eXPRESS Polymer Letters Vol.9, No.5 (2015) 401
Available online at www.expresspolymlett.com
DOI: 10.3144/expresspolymlett.2015.38

Editorial corner – a personal view
Polymer nanocomposites for energy applications

S. C. Tjong[*], *L. X. He*

City University of Hong Kong, Department of Physics and Materials Science, Kowloon, Hong Kong

The demand for developing sustainable and clean energy production, energy transportation, and storage, has grown rapidly in recent years due to the increase in fossil fuel consumption, environmental issue and global warming. Nanomaterials with different morphologies, properties and structures (e.g. barium titanate nanoparticles, carbon nanotubes, ZnO nanowires) offer superior chemical, mechanical or physical properties compared to their micrometer-scale counterparts. Accordingly, they are potential candidate materials for clean energy applications such as the energy storage, fuel cells, and solar cells (ISBN: 978-0-12-407796-6). The nanomaterials can be incorporated into polymers at low loading levels to form nanocomposites with greater mechanical flexibility, tailored properties and functionalities. These include bipolar plates of fuel cells (DOI: 10.1039/c0ee00689k), high-energy density capacitors, solid polymer electrolytes, and hybrid polymer/nanoparticle solar cells (DOI: 10.1016/j.jcis.2011.12.016). Nanofillers offer larger interfacial area that allows better interaction with the polymer matrix. Polymers provide structural support and protection for nanomaterials during their industrial service lives. A wide variety of polymers can be selected for making nanocomposites for various fields of energy applications depending on the designed chemical, physical and mechanical properties.

The major challenges of achieving high-performance polymer nanocomposites are the attainment of uniform dispersion of nanofillers in the polymer matrix and the manipulation of nanofiller/polymer interfaces. Typical approaches include surface modification of nanofillers via covalent and noncovalent functionalization. Significant research efforts have been devoted by chemists and materials scientist for developing polymer nanocomposites with novel functionalities using improved fabrication techniques recently. For instance, polymeric materials with high dielectric constant (k) and low loss find useful application for making supercapacitors. The β-phase of polyvinylidene fluoride is known to exhibit excellent ferroelectric and piezoelectric effects. This phase can be increased to ~46% by adding 0.5 wt% carbon nanotubes and processed through electrospinning. The process stretches polymer solution uniaxially under an electric potential. It can be further increased over 90% by mechanical drawing (DOI: 10.1021/jp4011026). To reduce dielectric loss, core-shell nanoparticle strategy emerges as a powerful method for preparing high-k nanocomposites especially filled with conducting nanomaterials (DOI: 10.1002/adma.201401310). To fully realize widespread commercial applications of polymer nanocomposites, it is necessary to develop cost-effective processes for the mass production of these materials in large quantities.

Prof. Dr. Sie Chin Tjong
Member of International Advisory Board

[*]Corresponding author, e-mail: APTJONG@cityu.edu.hk

eXPRESS Polymer Letters Vol.9, No.5 (2015) 402–411
Available online at www.expresspolymlett.com
DOI: 10.3144/expresspolymlett.2015.39

Antibacterial treatment of LDPE with halogen derivatives via cold plasma

A. Popelka[1], I. Novák[2], M. Lehocký[3], F. Bílek[3], A. Kleinová[2], M. Mozetič[4], M. Špírková[5], I. Chodák[2]*

[1]Center for Advanced Materials, Qatar University, P.O. Box 2713, Doha, Qatar
[2]Polymer Institute, Slovak Academy of Sciences, Dúbravská cesta 9, 845 41 Bratislava 45, Slovakia
[3]Centre of Polymer Systems, University Institute, Tomas Bata University in Zlín, Nad Ovčírnou 3685, 760 01 Zlín, Czech Republic
[4]Department of Surface Engineering, Jožef Stefan Institute, Jamova cesta 39, SI-1000 Ljubljana, Slovenia
[5]Institute of Macromolecular Chemistry, Academy of Sciences of the Czech Republic, Heyrovsky Sq. 2, 160 06 Prague, Czech Republic

Received 25 August 2014; accepted in revised form 14 November 2014

Abstract. The factor limiting the application of low-density polyethylene (LDPE) in healthcare is its high susceptibility to bacterial growth. For this reason, we here investigated antibacterial treatments of LDPE foils using appropriate antibacterial agents. Benzalkonium chloride and bronopol were selected because of their satisfactory antibacterial effect, which has been confirmed by their application in the medical and cosmetic industries. The aforementioned substances were immobilized by a multistep approach via the grafting of polyacrylic acid (PAA) brushes onto LDPE surfaces pre-treated with low-temperature plasma. Measurements of the surface energy, peel strength of the adhesive joints, X-ray photoelectron spectroscopy (XPS), Fourier-transform infrared spectroscopy with attenuated total reflectance (FTIR-ATR), and atomic force microscopy (AFM) were used to investigate the surface and adhesive properties of the antibacterial-treated LDPE. Moreover, the antibacterial effect was determined via measurements of the inhibition zone of the *Staphylococcus aureus* (*S. aureus*) bacterial strain. The antibacterial activity of benzalkonium chloride was observed to be more pronounced than that of bronopol. Inhibition-zone measurements of *Escherichia coli* (*E. coli*) were also conducted, but an antibacterial effect was not observed.

Keywords: *adhesion, benzalkonium chloride, bronopol, plasma treatment, antibacterial activity*

1. Introduction

Polyethylene (PE) has found uses in various biomedical applications [1], such as the production of catheters [2]. However, PE often leads to unfavorable infections that represent serious clinical complications [3]. These infections can result in implant failure, which can lead to numerous health problems [4]. To overcome this disadvantage, an anti-infection modification of PE is frequently applied. Anti-infective properties of polymers are achieved by the incorporation of an anti-infection agent into the polymer bulk or by copolymerization of an anti-infection agent with a monomer. Recently, an antibacterial surface treatment was demonstrated to be the preferred choice because it exhibited several advantages: it did not influence the bulk properties of the polymer, antibacterial agents were not released from the polymer volume, and the procedure was relatively simple and effective [5].

In this study, a multistep approach consisting of plasma surface treatment, radical graft polymerization [6, 7] of acrylic acid (AA) and the immobilization of antibacterial agents, was used (Figure 1) [8]. Surface treatment with low-temperature plasma plays a pronounced role in the surface treatment of polymers without influencing their volume properties

*Corresponding author, e-mail: anton.popelka@qu.edu.qa

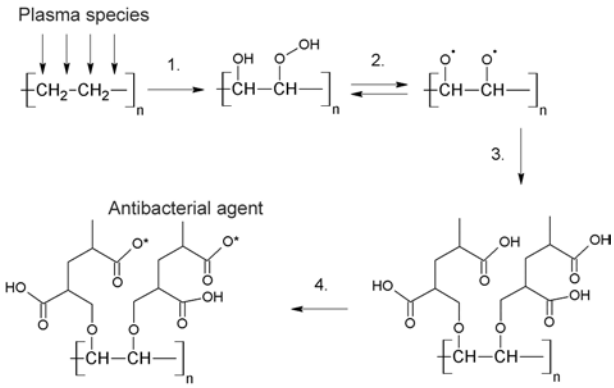

Figure 1. Multistep approach of the antibacterial treatment: 1. plasma treatment; 2. radicals generation; 3. AA radical graft polymerization; and 4. immobilization of the antibacterial agents

[9, 10]. Moreover, the use of low-temperature plasma is an environmental friendly, clean and dry process [11]. Low-temperature plasma facilities are often used in the electronic, aerospace, automotive, textile and biomedical industries [12, 13]. The products of the low-temperature plasma discharge, such as electrons, ions and excited atoms, are capable of interacting with the solid polymer surface. These interactions can lead to the functionalization (i.e., the creation of functional groups), etching (i.e., ablation), polymerization, or cross-linking processes [14]. Diffuse coplanar surface barrier discharge (DCSBD) plasma generators are used by facilities to generate the high surface power density of plasma discharges. The main advantage of this plasma system is its ability to operate at atmospheric pressure (i.e., it is suitable for continuous processes) [15]. The lifetime of electrodes is prolonged through the use of electrodes embedded in Al_2O_3 and connected to a cooling system [16]. Moreover, the high surface density of plasma generates visually macroscopically homogeneous low-temperature plasma discharges [17].

Low-temperature plasma can also initiate a radical graft polymerization of acrylic acid (AA) on the polymer surface [18]. The brushes of the resulting polyacrylic acid (PAA) represent an effective interfacial layer for antibacterial immobilization [19]. Benzalkonium chloride (Figure 2a) is known to be a safe, nontoxic biocide and is currently used in human pharmaceuticals [20]. Bronopol (Figure 2b) is another efficient antibacterial agent with a low clinical toxicity and as an effective protecting agent is used in various applications (e.g., water protection, cosmetics) [21]. These antibacterial agents are capable of inhibiting the proliferation of microorganisms on

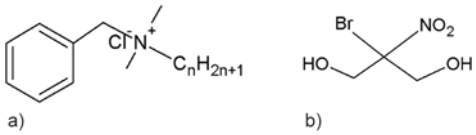

Figure 2. Scheme of: a) benzalkonium chloride and b) bronopol

the polymer surface [22]. The antibacterial activity of treated LDPE was investigated as a tool for eliminating the bacterial strains *Staphylococcus aureus* (*S. aureus*)–a gram-positive coccal bacterial strain that can lead to, for example, urinary tract infections and *Escherichia coli* (*E. coli*), which is a gram-negative rod-shaped bacteria that causes, for example, intestinal disease [23].

2. Experimental

2.1. Materials

Branched low-density polyethylene LDPE foils BRALEN FB 2-17 (T_m = 114°C, T_g = –110°C, M_w = 260 000 and PDI = 22.5) with a thickness of 20 μm were used in this study. The foils were supplied by Slovnaft-MOL (Slovakia) and contained no additives. These LDPE foils comply with the Food Contact Regulations and are approved for food contact; in addition, the grade is appropriate for use in pharmaceutical packaging products. Acrylic acid (AA, 99.0%, anhydrous, Acros Organics, Belgium) was used for the radical graft polymerization. Sodium metabisulfite (99.0%, Reagent plus, Merck, USA) was used as an inhibitor of acrylic acid homopolymerization. *N*-(3-Dimethylaminopropyl)-*N′*-ethylcarbodiimide hydrochloride (EDAC, 98.0%, Fluka, USA) was used as a carboxyl-group activator for enabling immobilization of antibacterial agents. Benzalkonium chloride (benzyl-dimethyl-tridecyl-azanium chloride, Sigma-Aldrich, Denmark) and bronopol (2-bromo-2-nitropropane-1,3-diol, Fluka, Germany) were used as antibacterial agents. Ultrapure water (produced by a Heal Force NW ULTRA pure water system) was used in the experiments. Diiodomethane (99.0%, Reagent plus), formamide (99.5%, molecular biology grade), and glycerol (99%, for molecular biology), which were supplied by Sigma-Aldrich (USA), were used as testing liquids for the surface wettability measurements.

2.2. Plasma treatment

The DCSBD plasma system developed by Černák *et al*. [15] was used to activate the LDPE foils. The

surface treatment was performed under dynamic conditions (i.e., the samples were in motion above the electrodes) at atmospheric pressure; the surface power density was 1 W/cm^2, the duration of the plasma treatment was 15 s, and air atmosphere was used as a working gas. Both sides of all samples were treated. A schematic of the DCSBD plasma equipment is shown in Figure 3. Two parallel banded systems consisting of several electrodes made of Ag paste (1 mm wide, 50 μm thick, and 0.5 mm spacing between the strips) were used to generate the low-temperature plasma discharges in an effective manner. These electrodes were embedded in 96% Al_2O_3, which protects the electrodes from direct contact with the plasma discharges and prolongs their durability. Moreover, the plasma panel was connected to a cooling system to prevent its overheating. A high-frequency sinusoidal voltage (≈15 kHz, $U_m \approx 10$ kV) was used to provide power to the electrodes led to the generation of macroscopically homogenous plasma and resulted in a uniform surface treatment.

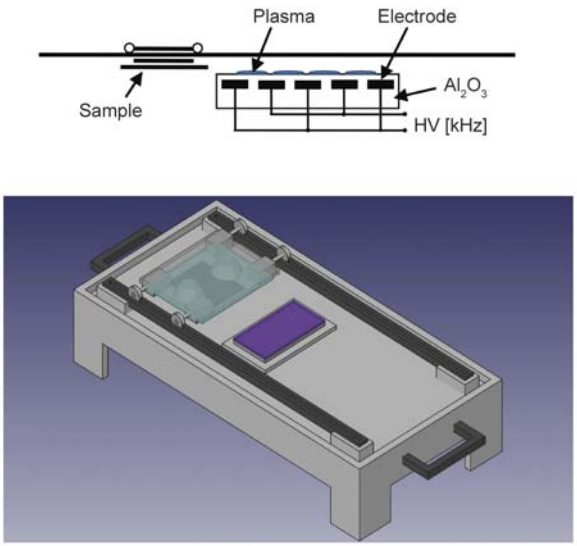

Figure 3. Schematic of the DCSBD plasma system

2.3. PAA grafting

Grafting of PAA onto the surface of the LDPE foil was performed immediately after plasma treatment by immersing the activated foil into a 10 vol% aqueous solution of AA for 24 h at 30°C. The solution also contained 0.1 wt% sodium metabisulfite as an efficient inhibitor of AA homopolymerization. The AA polymerization reaction led to the formation of PAA brushes, such was seen from AFM measurement and rendered it suitable for the effective immobilization of antibacterial agents. Finally, the prepared samples were thoroughly washed in distilled water for 5 min at 30°C to remove weakly bound or unreacted AA. The pre-treated samples were used for the immobilization of the antibacterial agents.

2.4. Benzalkonium chloride and bronopol immobilization

The PAA grafted substrates were subsequently immersed in a 0.1% (w/v) aqueous solution of EDAC at 4°C for 6 hours to activate the carboxyl groups, as shown in Figure 4. *O*-Acylisourea moieties are formed by this activation, and the PAA brushes are subsequently able to react with certain reducing agents. Two procedures were used: pre-treated LDPE samples were immersed in a benzalkonium chloride 2% (w/v) solution in distilled water for 24 hours at 30°C, and, alternatively, pre-treated LDPE samples were immersed in a bronopol 2% (w/v) solution in absolute ethanol for 24 hours at 30°C. Finally, samples with an immobilized antibacterial agent were washed in water and dried for 24 h at room temperature.

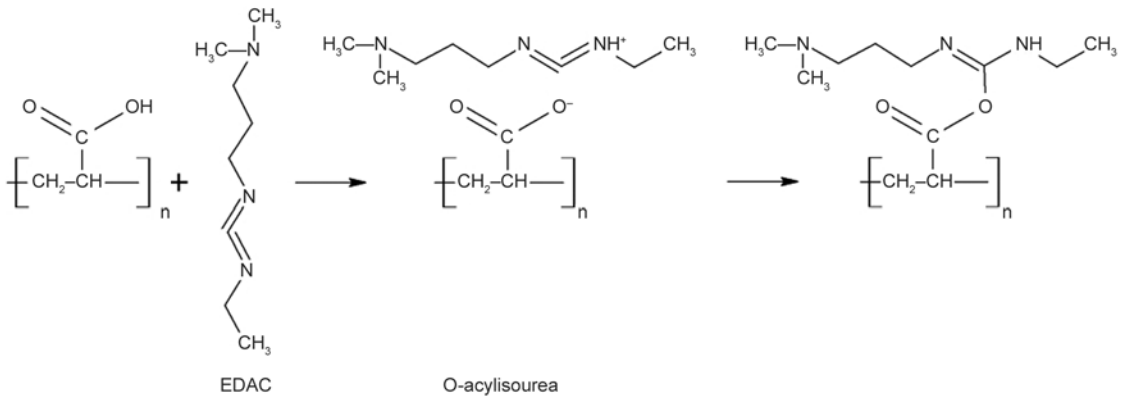

Figure 4. Carboxyl-group activation by EDAC

2.5. Surface wettability investigation

The surface wettability of the samples was investigated via sessile drop contact angle measurements. A surface energy evaluation system (SEE system, Advex-Instruments, Czech Republic) was used in this study. The CCD camera resolution was set to 1280×960 pixels to ensure that high-quality images of the drops were recorded. The contact angle refers to the angle between the solid/liquid interface and the liquid/vapor interface. Ultra-pure water, ethylene glycol, glycerol, formamide, and diiodomethane were used as test liquids. The contact angle was recorded after 3 s to allow thermodynamic equilibrium to be established between the solid, liquid, and gas phases. Average values of contact angles were used to calculate the surface free energy (γ^{tot}), and its polar (γ^{p}) and dispersive (γ^{d}) components were evaluated using the Owens-Wendt-Rabel-Kaelble regression model [24].

Moreover, changes in the graft yield of LDPE samples obtained by gravimetric measurements are also included. The graft yield (*GY*) was calculated by Equation (1):

$$GY = \frac{W_2 - W_1}{W_1} \cdot 100\,[\,\%\,] \qquad (1)$$

where W_1 and W_2 are the weights of the samples before and after the surface treatment [25].

2.6. Adhesive properties assessment

The adhesion properties between two materials are characterized by peel strength (force per unit width). The adhesive joint created from LDPE samples and poly(2-ethyhexyl acrylate) deposited on 15 mm polypropylene foil were used for the peel-strength measurements. Steel roller (3 kg) was used for the preparation of adhesive joint with constant distribution of adhesive forces. We performed these measurements by conducting 90° peel tests at a peel rate 10 mm/min using a universal INSTRON 4301 (UK) dynamometer equipped with 100 N load cell. The end parts of the LDPE samples were firmly fixed in clamps in a circular arrangement to achieve an even distribution of tension across the entire width. PP foil with an adhesive as a second part of the adhesive joint was fixed in the clamp connected to the load cell.

2.7. Surface morphology analysis

Atomic force microscopy (AFM) investigations of the surface topography were performed on a commercial atomic force microscope (Dimension Icon, Bruker) equipped with an SSS-NCL probe, Super Sharp SiliconTM-SPM-Sensor (NanoSensorsTM Switzerland; spring constant 35 N/m, resonant frequency: 170 kHz). The areas for individual AFM measurements were carefully chosen after previous screening of the surface regularity. Measurements were performed under ambient conditions and in tapping mode. The scans covered the sizes from 0.5×0.5 to 10×10 μm^2. Characteristic AFM images for each sample (area 10×10 μm^2) are represented in this paper.

2.8. Surface chemistry investigation

Fourier-transform infrared spectroscopy with attenuated total reflectance (FTIR-ATR) was used to determine the chemical composition of LDPE samples. The individual measurements were performed with a FTIR NICOLET 8700 spectrometer (Thermo Scientific, USA) using a single-bounce ATR accessory equipped with a Ge crystal at an angle of incidence of 45°. The spectral resolution and the number of scans were 2 cm^{-1} and 64, respectively, for each measurement. A pressure clamp was used to achieve sufficient spectral quality, which depends on a good contact between the crystal and investigated sample. The acquired spectra were analyzed using the OMNIC™ v8.1 spectroscopic software.

X-ray photoelectron spectroscopy (XPS) was used to quantify the chemical composition of LDPE samples. For this purpose, a TFA XPS Physical Electronics (USA) XPS instrument was used. The pressure in the chamber was approximately 6·10^{-8} Pa. The LDPE samples were irradiated with X-rays over a 400 μm spot area using monochromatic Al $K_{\alpha 1,2}$ radiation at 1486.6 eV. The photoelectrons were detected with a hemispherical analyzer placed at an angle of 45° with respect to the normal to the surface of the LDPE samples. Each survey-scan spectrum was collected at a pass energy of 187.85 eV and at an energy step of 0.4 eV. An electron gun was used for surface neutralization. The concentration of individual elements was determined using the MultiPak v7.3.1 software (Physical Electronics).

2.9. Antibacterial efficacy tests

The antibacterial effect of treated LDPE samples was determined against the *S. aureus* (CCM 4516) bacterial strain via measurement of an inhibition zone diameter on agar. Nutrient agar No. 2 M1269

– 500 g (HiMedia Laboratories PII, Ltd.) was used in this study. Circle-shaped LDPE samples (diameter ≈ 8 mm) were washed with ethanol, dried and placed on an agar plate inoculated with the bacterial suspension (volume = 100 μL, concentration = 10^7 units mL^{-1}). The samples were incubated for 24 h at 37°C. After 24 h, the diameters of the inhibition zone were measured in 5 directions to obtain average values; the test was repeated three times. The inhibition zone area was calculated as the area of annulus between the inhibition zone borders and the LDPE samples.

3. Results and discussion

3.1. Surface wettability

The ability of liquid to remain in contact with the solid surface is expressed by the surface's wettability. The wettability belongs among a very important factor supporting the antibacterial behavior. Hydrophilic brush layer can be responsible for attraction of water and form a repellent layer on the surface. There is steric hindrance for proteins or microorganisms to adsorb to the surface and the adsorption is reduced by several orders of magnitude [26]. For the above mentioned reason, the wettability measurement has very high importance for a characterization of the antibacterial surfaces. The wettability denotes the angle between the liquid drop and the solid surface. The contact-angle measurements were used to determine the wettability. The contact angle of several testing liquids was used to evaluate the surface free energy. The surface free energy indicates reversible work done for a unit surface area creation. The parameters related to wettability, such as the contact angle of testing liquids, the total surface free energy (γ^{tot}) and the dispersive (γ^{d}) and polar (γ^{p}) components of the free energy and *GY* are summarized in Table 1.

Given the hydrophobic and chemically inert nature of the surface of LDPE, the contact angles of the investigated testing liquids were relatively high. A significant decrease in contact angles was observed after plasma treatment of LDPE samples because of the incorporation of characteristic polar functional groups such as C=O, –OH, COOH, COO–, and C–O–C into the surface. The next step, which consisted of the radical graft polymerization of AA, resulted in a further decrease in the contact angles due to the polar character of PAA. The presence of bronopol and benzalkonium chloride also led to decreased contact angles in comparison to those of untreated LDPE. On the basis of contact angle measurements, we calculated the values of the surface energy and its components. Untreated LPDE is characterized by a very low surface energy, consistent with its hydrophobic character. The plasma treatment of LDPE resulted in an increase in the surface free energy due to the increased surface polarity. LDPE modified with polar PAA, bronopol and benzalkonium chloride exhibited very high surface free energy values. The graft yield of LDPE samples modified with antibacterial agent increased in compare with LDPE modified by PAA as result of introduction of benzalkonium chloride and bronopol on PAA brushes. The value of *GY* in case of benzalkonium chloride introduction was higher than in case of bronopol probably because of higher immobilization efficiency of benzalkonium chloride on PAA brushes.

3.2. Adhesive properties

The wettability closely relates to adhesion, which can be characterized by peel-test measurements. The results obtained from these measurements are presented in Figure 5. The adhesion of polymers correlates to their surface energy and to their roughness. Increased wettability of the LDPE surfaces results in increased adhesion and vice versa. Moreover, the increase in surface roughness is correlated with the adhesion increase due to the increase of surface con-

Table 1. Surface properties of LDPE modified via a multistep process (θ – contact angle, γ^{tot} – total surface free energy, γ^{d}, γ^{p} – dispersive and polar components of the surface free energy, respectively; *GY* – graft yield)

LDPE sample	θ_w [°]	θ_e [°]	θ_g [°]	θ_d [°]	θ_f [°]	γ^{tot} [mJ/m^2]	γ^{d} [mJ/m^2]	γ^{p} [mJ/m^2]	GY [%]
Untreated	99.2 (±0.6)	70.9 (±1.2)	85.3 (±0.9)	48.4 (±1.2)	80.7 (±0.9)	31.7	31.5	0.2	
Plasma-treated (A)	77.5 (±1.1)	51.0 (±2.8)	67.1 (±2.8)	36.0 (±1.2)	52.8 (±1.5)	42.6	41.4	1.1	0.0
A + PAA grafted (B)	66.9 (±0.7)	32.1 (±2.4)	57.2 (±2.7)	32.5 (±1.6)	37.0 (±2.0)	48.1	43.7	4.5	0.5
B + benzalkonium chloride coated	70.7 (±0.4)	52.9 (±2.2)	58.9 (±2.0)	40.3 (±0.8)	37.2 (±2.7)	43.1	36.4	6.7	3.4
B + bronopol coated	73.1 (±1.2)	31.8 (±3.0)	65.6 (±2.5)	37.5 (±1.0)	36.8 (±2.5)	45.6	40.4	5.2	0.9

w = deionized water, *e* = ethylene glycol, *g* = glycerol, *d* = diiodomethane, *f* = formamide

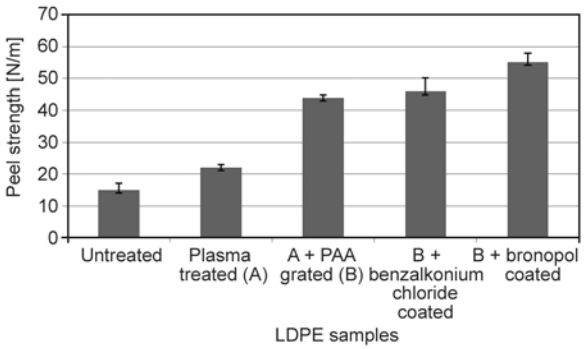

Figure 5. Changes in peel strength after each particular step of the LDPE antibacterial treatment

tact area. Adhesion is a complex phenomenon consisting of several chemical and physicochemical factors, as demonstrated in aforementioned results. A relatively low value of peel strength for the untreated LDPE was observed as result of the hydrophobic and chemically inert nature of the polymer. Moreover, the roughness of untreated LDPE was relatively low. The plasma treatment led to a more than twofold increase in the peel strength, caused by changes in the polarity and surface morphology. The grafting of PAA onto LDPE resulted in increased peel strength. The peel strength also increased in the cases of benzalkonium-chloride- and bronopol-coated LDPE samples.

3.3. Surface morphology

Changes in the surface roughness of untreated and antibacterial-treated LDPE were determined by AFM (Figure 6). Details related to the increase or decrease of the surface roughness were compared via the profile roughness parameter (R_a). The R_a value represents the average height of the irregularities in a perpendicular direction toward the sample surface, and, in the case of untreated LDPE, was being 38.1 nm in 10 μm of scan area (Figure 6a) as a consequence of the procedure used to prepare the foils. The plasma treatment led to a decrease in the roughness, as indicated by an decrease in the R_a value to 21.9 nm (Figure 6b) as a result of surface changes induced by the functionalization and ablation processes. In the case of the AA radical graft polymerization step, the R_a value increased compared to that of the plasma-treated LDPE surface because PAA brushes were created on the LDPE surface (Figure 6c). The agglomerates created from bronopol resulted in an increase of the surface roughness; therefore, the R_a values bronopol reached 37.2 nm (Figure 6d) while benzalkonium chloride formed more uniform layer and R_a was 29.2 nm (Figure 6e).

3.4. Surface chemistry analysis

Semi-quantitative information about chemical changes in the near-surface region was obtained from FTIR-ATR measurements. The spectrum of pristine LDPE is characterized by bands (Figure 7, curve a) associated with $–CH_2–$ stretching (2848 and 2915 $cm^{–1}$), asymmetric C–H and $–CH_3$ bending in plane (1460 and 1470 $cm^{–1}$, respectively), symmetric C-H bending in plane (1377 $cm^{–1}$), and C–H $(–CH_2–)_{n\geq 6}$ rocking (doublet with maxima at 720 and 731 $cm^{–1}$) [27]. The plasma surface treatment of LDPE resulted in significant spectral changes (Figure 7, curve b), which provided clear evidence of the incorporation of certain oxygen-containing groups, i.e., –OH (region 3700–3080 $cm^{–1}$) and/or other oxygen-containing products at the surface of the polymer (region 1845–1510, 1280, 1126, 1150 $cm^{–1}$, acid, ketone, aldehyde) [28]. The modification of LDPE by PAA grafting and by subsequent treatment with benzalkonium chloride and bronopol led to additional spectral changes. Characteristic peaks of PAA grafted onto LDPE were observed, specifically, the most intense peak at 1712 $cm^{–1}$ (carbonyl band, C=O stretching) and some unresolved peaks in the fingerprint region (1300–1100 $cm^{–1}$, C–O stretching and CH_2 bending), as shown in Figure 7, curve c. The presence of benzalkonium chloride was confirmed by the presence of the absorbance band at 702 $cm^{–1}$, which is attributed to C–Cl vibrations (Figure 7, curve d). The spectrum of LDPE treated with bronopol shows characteristic peaks at 3300 $cm^{–1}$ (–OH), 1557, 1340 $cm^{–1}$ ($–NO_2$) and 852 $cm^{–1}$ (C–Br) resulting from the incorporation of bronopol into the LDPE surface (Figure 7, curve e).

XPS was used to quantify the characteristic presence of typical chemical elements after each step of the antibacterial treatment. The surface composition of the LDPE samples, which is shown in Table 2, was measured at two different spots, allowing the average surface composition to be calculated.

The high resolution C1s spectra of all samples are shown in Figure 8. In the spectrum of untreated LDPE, only a C1s peak was present (Figure 8a), which is attributed to C–C/C–H bonds. The greatest amount of oxygen and also nitrogen functional

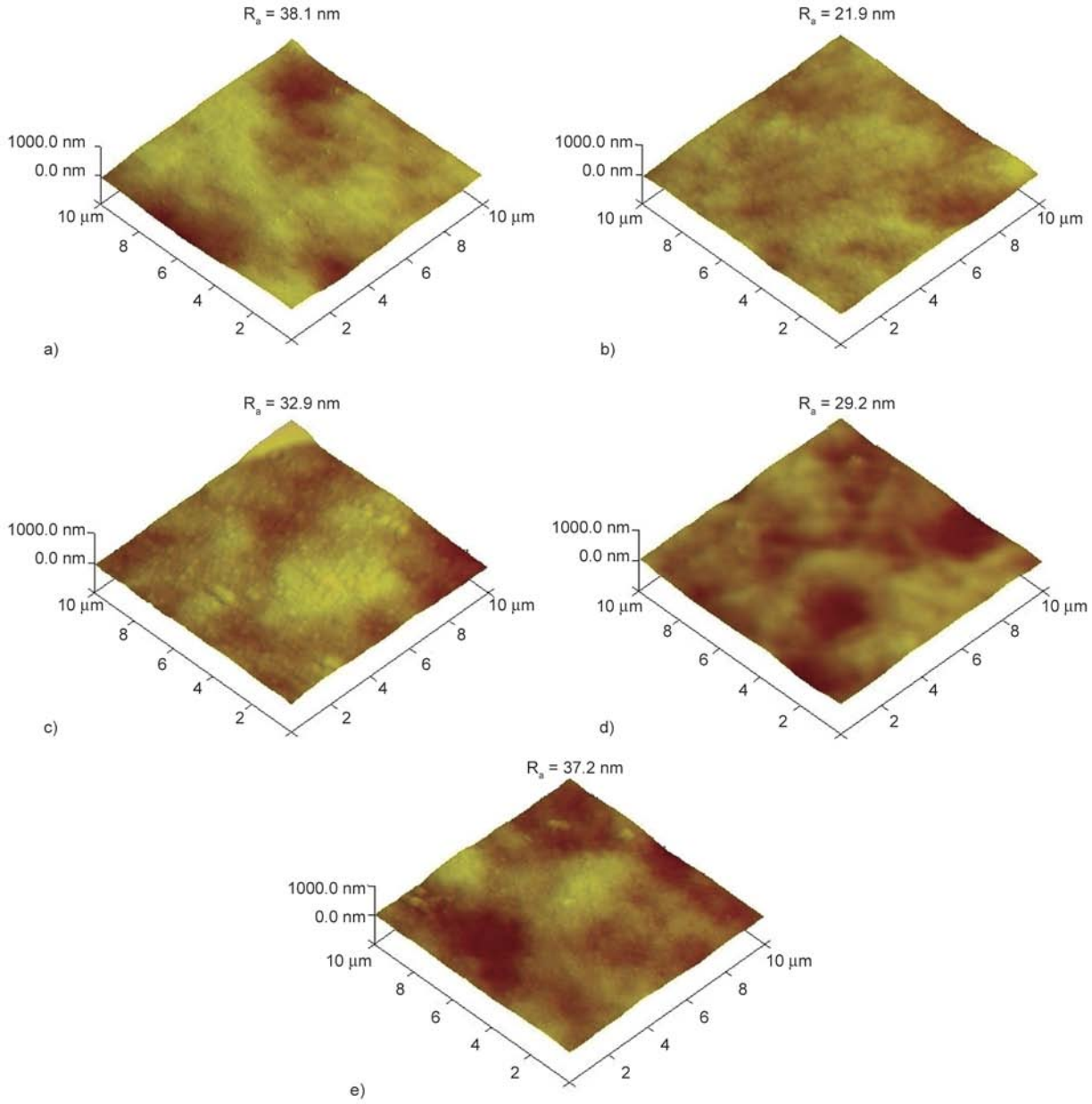

Figure 6. AFM images of LDPE sample surfaces and the samples' corresponding R_a values: a) untreated; b) plasma treated (A); c) A + PAA grafted (B); d) B + benzalkonium chloride coated; and e) B + bronopol coated

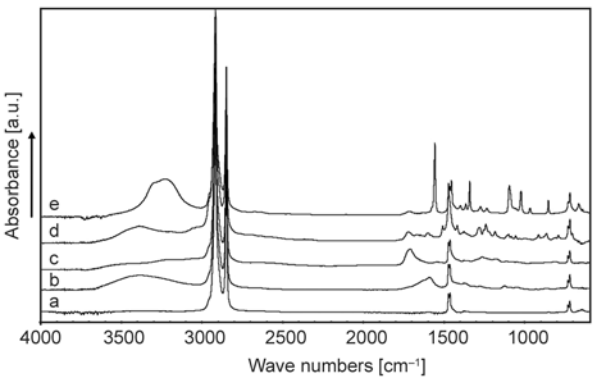

Figure 7. FTIR-ATR spectra of LDPE samples: a) untreated; b) plasma treated (A); c) A + PAA grafted (B); d) B + benzalkonium chloride coated; and e) B + bronopol coated

groups (19.8 and 4.0 at%, respectively) were observed in the plasma-treated LDPE sample. In this case, the carbon C1s peak represents C–C/C–H, O=C–O, C=O, and C–O groups (Figure 8b) and the nitrogen N1s peak is composed from different chemical bonds of nitrogen atoms such as C–N, C–NH_3^+, and –ONO_2. The spectrum of the LDPE sample grafted with PAA showed mainly the presence of an O1s peak as a consequence of the incorporation of carboxyl groups (Figure 8c); however, this peak may also indicate the presence of other oxygen groups created during plasma treatment. These samples also contained some iron traces and sulfur

Table 2. Surface composition of LDPE samples, as obtained from XPS measurements

LDPE samples	C1s	N1s	O1s	Cl2p	Si2p	S2p	Br3d
	[at%]						
Untreated	100.0	0	0				
Plasma treated (A)	76.3	4.0	19.8				
A + PAA grafted (B)	84.1	0	15.6			0.4	
B + benzalkonium chloride coated	87.8	3.0	4.7	4.5			
B + bronopol coated	91.5	0	7.1		1.3		0.1

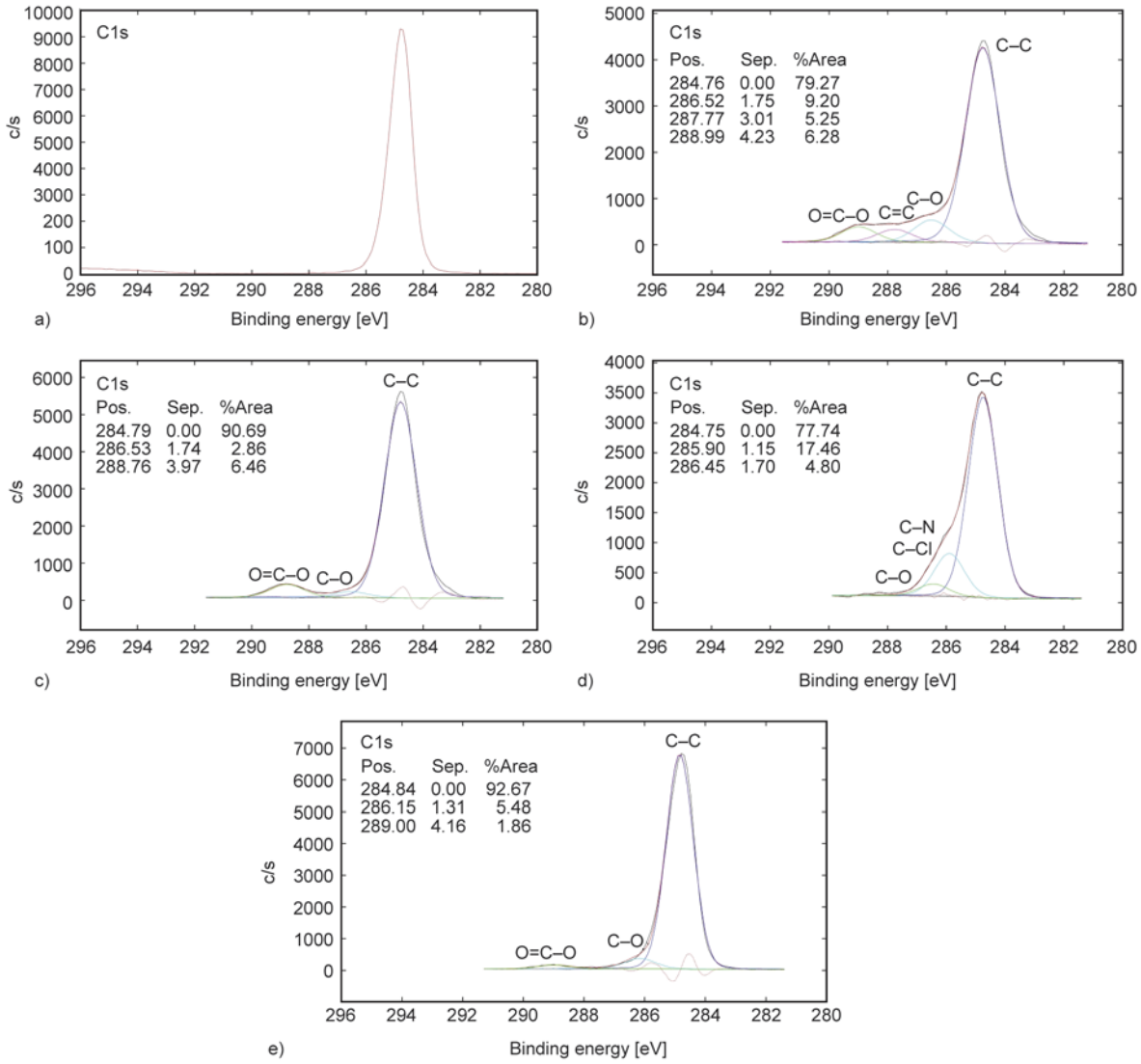

Figure 8. High resolution C1s spectra of LDPE samples: a) untreated; b) plasma treated (A); c) A + PAA grafted (B); d) B + benzalkonium chloride coated; and e) B + bronopol coated

impurities (approximately 0.4 at%) which probably originated from dust or chemicals. XPS spectra of the benzalkonium chloride-coated LDPE sample revealed the presence of N and Cl (Figure 8d), which originate from the antibacterial agent. The presence of a small amount of Br (0.1 at%) was detected in LDPE samples coated with bronopol, which is likely associated with the creation of the very thin bronopol layer.

3.5. Antibacterial effect

The antibacterial effect was determined by measurement of the inhibition zones. The results were averaged to obtain the one representative value when all three repeated measurements of the LDPE samples treated in the same manner exhibited some antibacterial activity. The measurements clearly indicated an antibacterial effect against *S. aureus*. In Figure 9, the inhibition zone values for each step

of the antibacterial treatment are presented. Samples coated with bronopol or benzalkonium chloride were active against *S. aureus*, which confirmed presence of the antibacterial agent. The best results were obtained for LDPE samples coated with benzalkonium chloride. Moreover, the use of PAA as an active platform for the immobilization of antibacterial agents had a more pronounced effect on the antibacterial activity against *S. aureus* in comparison to, e.g., LDPE samples grafted by allylamine, reported elsewhere [29]. Antibacterial activity against E. coli was not sufficiently demonstrated.

4. Conclusions

This work was focused on the anchoring of selected antibacterial agents to the surface of LDPE through the use of low-temperature plasma and PAA grafting on pre-treated samples. Such treated LDPE samples exhibited changes in their surface and chemical composition. The immobilization of the antibacterial agents led to changes in the surface roughness of LDPE which was confirmed by the R_a value increase from 21.9 nm for the plasma treated LDPE to 29.2 and 37.2 nm for PE surfaces grafted with benzalkonium chloride and bronopol, respectively. Moreover, this antibacterial treatment significant affected the wettability and adhesion of LDPE as a consequence of the increase in roughness and hydrophilicity, as previously mentioned, whereas the γ^{tot} of LDPE increased from 31.7 to 43.1 mJ/m^2 and 45.6 mJ/m^2 for LDPE surfaces covered with benzalkonium chloride and bronopol, respectively. The increase in hydrophilicity was caused by the introduction of polar functional groups present in the applied antibacterial agents, as was proven by FTIR-ATR and XPS measurements. The antibacterial effect of such

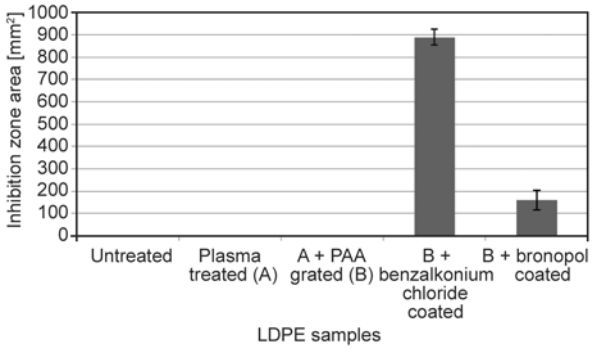

Figure 9. The inhibition zone area of LDPE samples after each step of the antibacterial treatment

treated LDPE films was confirmed by measurements of the inhibition zone of *S. aureus*; the most pronounced antibacterial activity was exhibited by LDPE samples treated with plasma, grafted with PAA, and subsequently coated with benzalkonium chloride. The antibacterial effect against *E. coli* was not sufficiently proven.

Acknowledgements

Financial support by the Ministry of Education, Youth, and Sports of the Czech Republic (Grant CZ.1.05/2.1.00/03.0111), the Slovak Academy of Sciences (Grant VEGA 2/0151/12 and 2/0199/14), Grant Agency of the Czech Republic (Czech Science Foundation, project No. 13-06700S and 13-08944S) are gratefully acknowledged. Author M. Mozetič would like to express his gratitude to the Slovenian Research Agency.

References

[1] Sanchis R., Fenollar O., García D., Sánchez L., Balart R.: Improved adhesion of LDPE films to polyolefin foams for automotive industry using low-pressure plasma. International Journal of Adhesion and Adhesives, **28**, 445–451 (2008). DOI: 10.1016/j.ijadhadh.2008.04.002

[2] Kuzuya M., Sawa T., Mouri M., Kondo S-I., Takai O.: Plasma technique for the fabrication of a durable functional surface on organic polymers. Surface and Coatings Technology, **169–170**, 587–591 (2003). DOI: 10.1016/S0257-8972(03)00116-6

[3] Zhang W., Chu P. K., Ji J., Zhang Y., Fu R. K. Y., Yan Q.: Antibacterial properties of plasma-modified and triclosan or bronopol coated polyethylene. Polymer, **47**, 931–936 (2006). DOI: 10.1016/j.polymer.2005.12.009

[4] Costa F., Carvalho I. F., Montelaro R. C., Gomes P., Martins M. C.: Covalent immobilization of antimicrobial peptides (AMPs) onto biomaterial surfaces. Acta Biomaterialia, **7**, 1431–1440 (2011). DOI: 10.1016/j.actbio.2010.11.005

[5] Newton A. P. N., Cadena S. M. S. C., Rocha M. E. M., Carnieri E. G. S., de Oliveira M. B. M.: Effect of triclosan (TRN) on energy-linked functions of rat liver mitochondria. Toxicology Letters, **160**, 49–59 (2005). DOI: 10.1016/j.toxlet.2005.06.004

[6] Suzuki M., Kishida A., Iwata H., Ikada Y.: Graft copolymerization of acrylamide onto a polyethylene surface pretreated with glow discharge. Macromolecules, **19**, 1804–1808 (1986). DOI: 10.1021/ma00161a005

[7] Johnsen K., Kirkhorn S., Olasen K., Redford K., Stori A.: Modification of polyolefin surfaces by plasma-induced grafting. Journal of Applied Polymer Science, **59**, 1651–1657 (1996). DOI: 10.1002/(SICI)1097-4628(19960307)59:10<1651::AID-APP17>3.0.CO;2-Z

[8] Asadinezhad A., Novák I., Lehocký M., Sedlařík V., Vesel A., Junkar I., Sáha P., Chodák I.: A physicochemical approach to render antibacterial surfaces on plasma-treated medical-grade PVC: Irgasan coating. Plasma Processes and Polymers, **7**, 504–514 (2010). DOI: 10.1002/ppap.200900132

[9] Vesel A., Mozetic M.: Surface modification and ageing of PMMA polymer by oxygen plasma treatment. Vacuum, **86**, 634–637 (2012). DOI: 10.1016/j.vacuum.2011.07.005

[10] Junkar I., Vesel A., Cvelbar U., Mozetič M., Strnad S.: Influence of oxygen and nitrogen plasma treatment on polyethylene terephthalate (PET) polymers. Vacuum, **84**, 83–85 (2010). DOI: 10.1016/j.vacuum.2009.04.011

[11] Vesel A., Mozetic M.: Surface functionalization of organic materials by weakly ionized highly dissociated oxygen plasma. Journal of Physics: Conference Series, **162**, 012015/1–012015/20 (2009). DOI: 10.1088/1742-6596/162/1/012015

[12] Wei Q. F.: Surface characterization of plasma-treated polypropylene fibers. Materials Characterization, **52**, 231–235 (2004). DOI: 10.1016/j.matchar.2004.05.003

[13] Lloyd G., Friedman G., Jafri S., Schultz G., Fridman A., Harding K.: Gas plasma: Medical uses and developments in wound care. Plasma Processes and Polymers, **7**, 194–211 (2010). DOI: 10.1002/ppap.200900097

[14] Slepička P., Slepičková Kasálková N., Stránská E., Bačáková L., Švorčík V.: Surface characterization of plasma treated polymers for applications as biocompatible carriers. Express Polymer Letters, **7**, 535–545 (2013). DOI: 10.3144/expresspolymlett.2013.50

[15] Černák M., Černáková Ľ., Hudec I., Kováčik D., Zahoranová A.: Diffuse coplanar surface barrier discharge and its applications for in-line processing of low-added-value materials. The European Physical Journal Applied Physics, **47**, 22806/1–22806/6 (2009). DOI: 10.1051/epjap/2009131

[16] Šimor M., Ráheľ J., Vojtek P., Černák M., Brablec A.: Atmospheric-pressure diffuse coplanar surface discharge for surface treatments. Applied Physics Letters, **81**, 2716–2718 (2002). DOI: 10.1063/1.1513185

[17] Černák M., Ráheľ J., Kováčik D., Šimor M., Brablec A., Slavíček P.: Generation of thin surface plasma layers for atmospheric-pressure surface treatments. Contributions to Plasma Physics, **44**, 492–495 (2004). DOI: 10.1002/ctpp.200410069

[18] Saxena S., Ray A. R., Mindemart J., Hilborn J., Gupta B.: Plasma-induced graft polymerization of acrylic acid onto poly(propylene) monofilament: Characterization. Plasma Processes and Polymers, **7**, 610–618 (2010). DOI: 10.1002/ppap.200900165

[19] Zhao B., Brittain W. J.: Polymer brushes: Surface-immobilized macromolecules. Progress in Polymer Science, **25**, 677–710 (2000). DOI: 10.1016/S0079-6700(00)00012-5

[20] Shi Z., Neoh K. G., Zhong S. P., Yung L. Y. L., Kang E. Y., Wang W.: *In vitro* antibacterial and cytotoxicity assay of multilayered polyelectrolyte-functionalized stainless steel. Journal of Biomedical Materials Research Part A, **76**, 826–834 (2006). DOI: 10.1002/jbm.a.30597

[21] Wang H., Provan G. J., Helliwell K.: Determination of bronopol and its degradation products by HPLC. Journal of Pharmaceutical and Biomedical Analysis, **29**, 387–392 (2002). DOI: 10.1016/S0731-7085(02)00078-X

[22] Tiller J. C.: Coatings for prevention or deactivation of biological contamination. in 'Developments in surface contamination and cleaning' (eds.: Kohli R., Mittal K. L.) Elsevier, Norwich, Vol 1, 1013–1065 (2007).

[23] Bílek F., Sulovská K., Lehocký M., Sáha P., Humpolíček P., Mozetič M., Junkar I.: Preparation of active antibacterial LDPE surface through multistep physicochemical approach II: Graft type effect on antibacterial properties. Colloids and Surfaces B: Biointerfaces, **102**, 842–848 (2013). DOI: 10.1016/j.colsurfb.2012.08.026

[24] Salimi A., Mirabedini S. M., Atai M., Mohseni M., Naimi-Jamal M. R.: Correlating the adhesion of an acrylic coating to the physico-mechanical behavior of a polypropylene substrate. International Journal of Adhesion and Adhesives, **31**, 220–225 (2011). DOI: 10.1016/j.ijadhadh.2011.01.003

[25] Işiklan N., Kurşun F., İnal M.: Graft copolymerization of itaconic acid onto sodium alginate using benzoyl peroxide. Carbohydrate Polymers, **79**, 665–672 (2010). DOI: 10.1016/j.carbpol.2009.09.021

[26] Knetsch M. L. W., Koole L. H.: New strategies in the development of antimicrobial coatings: The example of increasing usage of silver and silver nanoparticles. Polymers, **3**, 340–366 (2011). DOI: 10.3390/polym3010340

[27] Asensio R. Ch., Moya M. S. A., de la Roja J. M., Gómez M.: Analytical characterization of polymers used in conservation and restoration by ATR-FTIR spectroscopy. Analytical and Bioanalytical Chemistry, **395**, 2081–2096 (2009). DOI: 10.1007/s00216-009-3201-2

[28] Sellin N., de C. Campos J. S.: Surface composition analysis of PP films treated by corona discharge. Materials Research, **6**, 163–166 (2003). DOI: 10.1590/S1516-14392003000200009

[29] Bílek F., Křížová T., Lehocký M.: Preparation of active antibacterial LDPE surface through multistep physicochemical approach: I. Allylamine grafting, attachment of antibacterial agent and antibacterial activity assessment. Colloids and Surfaces B: Biointerfaces, **88**, 440–447 (2011). DOI: 10.1016/j.colsurfb.2011.07.027

eXPRESS Polymer Letters Vol.9, No.5 (2015) 412–423
Available online at www.expresspolymlett.com
DOI: 10.3144/expresspolymlett.2015.40

Graphene nanoplatelets-reinforced polyetherimide foams prepared by water vapor-induced phase separation

*H. Abbasi, M. Antunes, J. I. Velasco**

Centre Català del Plàstic. Universitat Politècnica de Catalunya, BarcelonaTech (UPC), Departament de Ciència dels Materials i Enginyeria Metal.lúrgica C/Colom 114, E-08222, Terrassa, Spain

Received 17 September 2014; accepted in revised form 21 November 2014

Abstract. The present work considers the preparation of medium-density polyetherimide foams reinforced with variable amounts of graphene nanoplatelets (1–10 wt%) by means of water vapor-induced phase separation (WVIPS) and their characterization . A homogeneous closed-cell structure with cell sizes around 10 μm was obtained, with foams exhibiting zero crystallinity according to X-ray diffraction (XRD). Thermogravimetric analysis under nitrogen showed a two-step thermal decomposition behaviour for both unfilled and graphene-reinforced foams, with foams containing graphene presenting thermal stability improvements, related to a physical barrier effect promoted by the nanoplatelets. Thermo-mechanical analysis indicated that the specific storage modulus of the nanocomposite foams significantly increased owing to the high stiffness of graphene and finer cellular morphology of the foams. Although foamed nanocomposites displayed no further sign of graphene nanoplatelets exfoliation, the electrical conductivity of these foams was significant even for low graphene contents, with a tunnel-like model fitting well to the evolution of the electrical conductivity with the amount of graphene.

Keywords: *nanocomposites, graphene nanoplatelets, polyetherimide foams, thermal stability, electrical conductivity*

1. Introduction

The growing necessity of weight reduction in the majority of industries continuously pushes the boundaries of material selection and production techniques to obtain lighter structures with improved specific properties and added functionalities [1–4]. For this reason, weight reduction of polymer-based composites by means of foaming, merged with integration of multifunctional fillers, has recently aroused a great interest [3, 4].

Carbon-based nanofillers, and particularly graphene, have recently attracted much attention owing to their inherently high mechanical and transport properties, which have provided wide sets of possibilities in sectors such as electronics or aerospace. Due to their conducting structure-dependent electronic properties, the role of these carbon nanoparticles has been suggested as a possible option to modify the electronic properties of polymers, partially solving some of the problems regarding the use of conductive polymers [1].

Among carbon-based nanofillers, graphene and graphene-derived materials have caught a great deal of attention due to their extraordinary combination of properties, such as high surface area, aspect ratio, tensile strength, thermal and electrical conductivities, electromagnetic interference (EMI) shielding efficiency, flexibility, transparency or low coefficient of thermal expansion [5–8].

From another point of view, the excellent thermal stability of graphene has promoted investigations on several polymer-based composites such as poly (vinyl alcohol) (PVA) [9, 10], poly(methyl methacrylate) (PMMA) [11], polystyrene (PS) [12], polyaniline [13], polypropylene (PP) [14] or polycarbonate (PC) [15] using different types of graphene, with

*Corresponding author, e-mail: jose.ignacio.velasco@upc.edu

remarkable enhancements in thermal stability being found. Another aspect of graphene that could have a favorable effect in terms of delaying polymer thermal decomposition is its platelet-like morphology, which, depending on the dispersion and exfoliation of graphene nanoplatelets (GnP) in the polymer matrix, could delay the escape of volatile products generated during polymer decomposition [15, 16].

It has been reported that polymers filled with layered nanoparticles such as polymer-clay nanocomposites [17] and polymers reinforced with graphene nanoplatelets [6] show great improvements in some thermo-mechanical properties at lower filler amounts when compared to conventional particulate composites.

One of the most interesting high-performance thermoplastic polymers for advanced applications is polyetherimide (PEI). The preparation of PEI foams using CO_2 as blowing agent has been studied by Jiang *et al*. [18]. Furthermore, a novel approach, recently proposed by Ling *et al*. [19], presents water vapor-induced phase separation (WVIPS) method as a proper way to obtain PEI-graphene nanocomposite foams. In this method, a proper solvent is chosen first to obtain a homogenous solution, which finally results in a cellular structure due to the nucleation of cells associated with the occurrence of phase separation promoted by the induction of water vapor from the humid atmosphere.

Although polymer composites with carbon nanofillers have been deeply investigated in the last decade, not many studies have been carried out regarding foams made from these materials. Some works have studied the influence of graphene nanoplatelets on the electrical conductivity of polymer foams, these foams displaying either a percolative electrical behaviour [19] or a tunnel-like one [20].

In terms of the thermal stability of polymer foams, significant improvements have been found in PC foams containing low amounts of GnP prepared using supercritical CO_2 (sCO_2) dissolution followed by one-step batch foaming [15], explained by a combination of a heat transfer reduction promoted by the insulating cellular structure and a physical barrier effect of the nanoplatelets, delaying the escape of volatile products generated during decomposition.

The incorporation of graphene into different polymers and foaming has recently been considered in terms of regulating the thermo-mechanical properties of the resulting foams. According to Yang *et al*. [21], the addition of graphene oxide (GO) to poly (propylene-carbonate) (PPC) foams prepared by the saturation of a PPC-GO nanocomposite using sCO_2 significantly improved the mechanical properties of the foam, with 1 wt% addition of GO leading to a 50 time increase in storage modulus and 9 time increase in compressive yield strength.

The present work aims to elucidate the influence of the addition of graphene nanoplatelets on PEI foams through the characterization of their morphology and structure, thermal stability, thermo-mechanical and electrical properties, with the final goal of developing multifunctional lightweight materials for advanced applications.

2. Experimental

2.1. Materials

Polyetherimide (PEI), with the commercial name of Ultem 1000, was provided by Sabic (Sittard, The Netherlands) in the form of transparent amber color solid bars. PEI Ultem 1000 has a density of 1.27 g/cm^3 and a glass transition temperature (T_g) of 217°C. The repeating unit of PEI Ultem 1000 is displayed in Figure 1.

Graphene nanoplatelets (commercial name xGnP-M-15 and density of 2.2 g/cm^3) were supplied by XG Sciences (Lansing, Michigan, USA). This material is formed by stacks of graphene layers having an average thickness of 6–8 nm and a diameter of 15 μm (see Figure 2), with a typical surface area of 120–150 m^2/g and an electrical resistivity of 10^7 and 10^2 S/m, respectively measured parallel and perpendicular to its surface, as reported by the manufacturer.

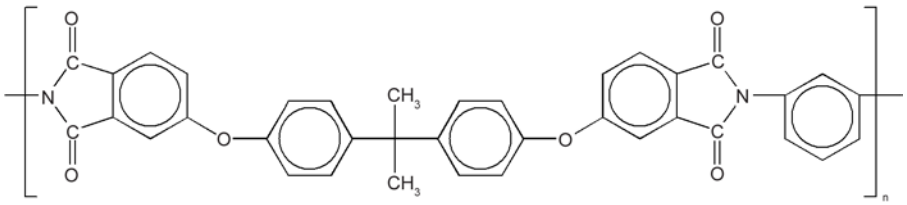

Figure 1. PEI Ultem 1000 repetitive unit

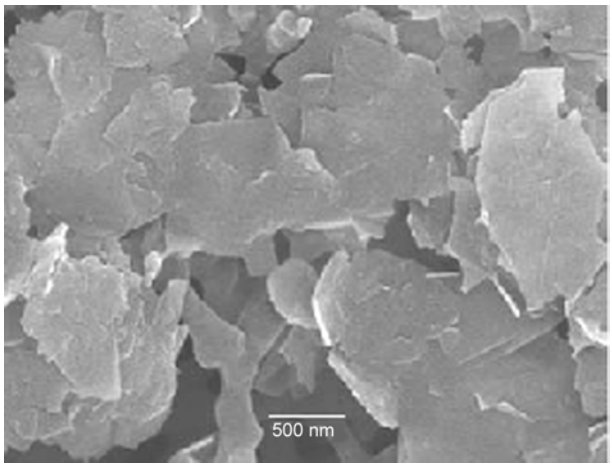

Figure 2. Characteristic platelet-like morphology of graphene nanoplatelets (GnP)

N-methyl pyrrolidone (NMP) was acquired from Panreac Co. (Barcelona, Spain) with a purity of 99% (boiling point: 202°C).

2.2. Foam preparation

Different amounts of graphene nanoplatelets (GnP) were first dispersed in 50 g of NMP (GnP-NMP solution), known to be one of the best solvents to suspend graphene at room temperature [22], and sonicated for 60 minutes using a Bransonic 3510E DTH ultrasonicator bath at a frequency of 42 kHz. Then, previously grinded PEI was dissolved in each suspension (16.6 g of PEI/50 g of GnP-NMP solution, i.e., a 25 wt% PEI solution) at 75°C and kept stirring at 450 rpm for 24 hours. Afterwards, each of the prepared solutions of PEI containing GnP (1, 2, 5 and 10 wt% GnP) was poured on a flat glass and exposed to air with a controlled humidity of 75% at room temperature for 4 days, which promoted foaming by WVIPS. Foams having two different thicknesses were prepared: thin foams (≈1 mm-thick) and thick foams (>3 mm-thick). Obtained foams were then kept stirring in hot water at 90°C for 7 days and later intensively dried under vacuum at 140°C during 7 additional days to fully remove the residual NMP (see scheme of PEI-GnP foam preparation by WVIPS shown in Figure 3). Demonstration of the full removal of NMP solvent from PEI-based foams is presented in section 3.1.

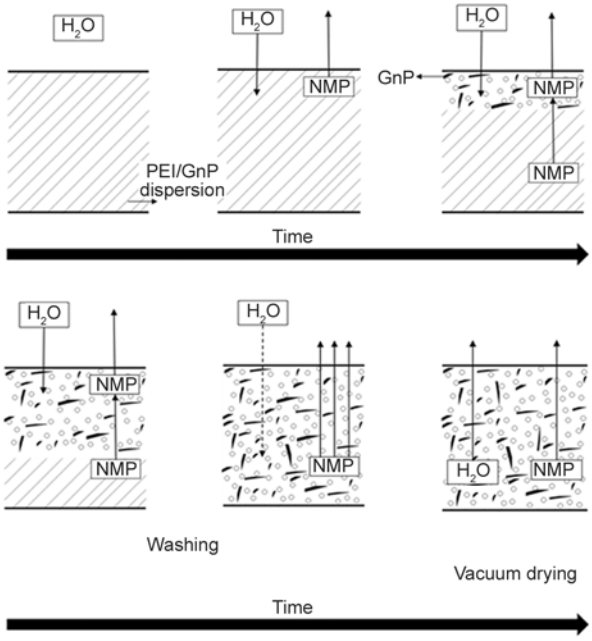

Figure 3. Scheme of PEI-GnP foam preparation by water vapor-induced phase separation (WVIPS)

2.3. Testing procedure

The density of the prepared foamed nanocomposites was measured according to a standard procedure (ISO-845). Due to the particular foam preparation process, the non-cellular nanocomposites were not available at any stage of the experiment and, therefore, solid density could only be theoretically calculated using the density values of the polymer and GnP and their respective weight fractions.

The morphology of the samples was analyzed using a JEOL JSM-5610 scanning electron microscope. Samples were prepared by brittle fracturing the foams using liquid nitrogen and sputter depositing a thin layer of gold onto the fractured surface in argon atmosphere using a BAL-TEC SCD005 Sputter Coater. Low-magnification micrographs were analyzed using the intercept counting method [23] in order to obtain the values of the average cell size (ϕ), cell nucleation density and cell density (N_0 and N_f, respectively), as well as to gather qualitative information of their cell shape. N_0 and N_f were calculated assuming an isotropic distribution of spherical cells according to Equations (1) and (2):

$$N_0 = \left(\frac{n}{A}\right)^{3/2}\left(\frac{\rho_s}{\rho_f}\right) \quad (1)$$

$$N_f = \frac{6}{\pi\phi^3}\left(1 - \frac{\rho_f}{\rho_s}\right) \quad (2)$$

where n is the number of cells in the micrograph, A [cm^2] is its area and ρ_s and ρ_f the solid and foam densities, respectively. In Equations (1) and (2) N_0 represents the number of cells per volume of unfoamed material and N_f the number of cells per volume of foamed material.

The crystalline characteristics of PEI and the exfoliation degree of graphene nanoplatelets were analyzed by X-ray diffraction (XRD) using a Panalytical diffractometer operating with CuKα radiation (λ = 0.154 nm) at 40 kV and 40 mA. Scans were taken from 2 to 60° using a scan step of 0.033°.

Differential scanning calorimetry (DSC) was carried out in order to assess the evolution of the glass transition temperature of PEI with drying time during foam preparation using a Perkin Elmer, Pyris 1 model with a glycol-based Perkin Elmer Intracooler IIP calorimeter at a heating rate of 10°C/min from 30 to 300°C using samples weighting around 8.0 mg.

A TGA/DSC 1 Mettler Toledo STAR System analyzer was used to evaluate the thermal decomposition of both pure and GnP-reinforced foamed materials by performing thermogravimetric analysis by heating samples of around 8.0 mg from 30 to 1000°C at a rate of 10°C/min. A constant running flow of nitrogen (30 ml/min) was used in the experiments. From the thermograms, the temperatures corresponding to sample mass losses of 5 and 40% and the amount of residue obtained at 1000°C were considered. Three different measurements were done for each material.

Dynamic-mechanical-thermal analysis (DMTA) was used to study the influence of the graphene nanoplatelets and foam density on the dynamic-mechanical-thermal response of the PEI-GnP foams. A DMA Q800 from TA instruments was used and calibrated in a single cantilever configuration. The experiments were performed from 30 to 270°C at a heating rate of 2°C/min and frequency of 1 Hz applying a dynamic strain of 0.02%. Test specimens were prepared in a rectangular shape with a typical length of 35.5±1.0 mm and width of 12.5±1.0 mm with various thicknesses: 1 mm in the case of thin foams and 3 mm in the case of thick foams. Three different measurements were done for each material (error < 5%).

The electrical conductivity of PEI and PEI-GnP foams was measured using a pA meter/dc voltage source HP model 4140B with a two-probe set. The connections were set up in the electrostatic light-shielded test box HP 16055A using electrolytic copper sheet electrodes. Square-shaped samples about 2 cm×2 cm in side and 0.5–1.0 mm thick were directly prepared from each foam and painted using colloidal silver conductive paint with a resistance per area ranging from 0.01 to 0.1 Ω/cm^2 in order to guarantee a good electrical contact between the electrodes and the sample's surface. A programmable direct current (*dc*) voltage feature with a range of 0–20 V and a voltage step of 0.05 V, a hold time of 10 seconds and a step delay time of 5 seconds, was used.

3. Results and discussion

3.1. Removal of NMP

The use of NMP as solvent for dispersing GnP prior to dissolving the PEI, albeit being the best option at room temperature when compared to other solvents (such as acetone, THF, benzene, toluene, dichlorobenzene or DMF) [22], has the downside of being difficult to remove. In order to demonstrate that no residual NMP was left in the materials after 7 consecutive days of intensive vacuum drying, on the one hand we analyzed by DSC the evolution of PEI's glass transition temperature with drying time (Figure 4a) and on the other hand the evolution of PEI's weight loss by TGA (Figure 4b).

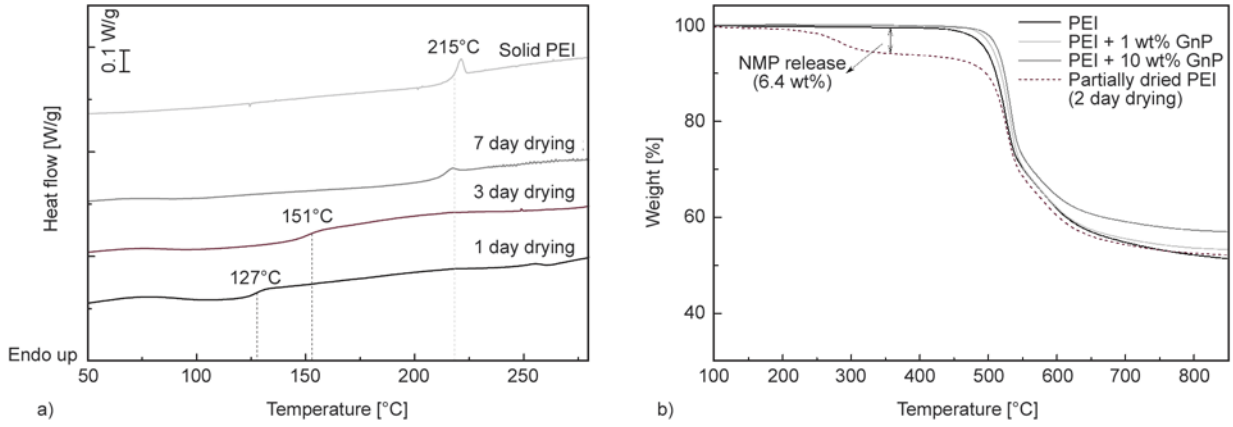

Figure 4. Evolution of the (a) glass transition temperature and (b) weight loss of PEI with incrementing the vacuum drying time during foam preparation showing full NMP removal after 7 days of drying

As can be seen, the glass transition temperature of PEI resulted considerably lower than that of the solid reference material (215°C) when NMP was present as residual solvent, NMP acting as PEI's plasticizer, i.e., PEI's T_g decreasing with increasing the amount of NMP. For instance, a more than 80°C difference in T_g was observed between the material dried under vacuum for 1 day and the solid reference PEI. Only after 7 days of intensive vacuum drying it was possible to fully remove the residual NMP present in the material, as can be seen by the fact that the T_g resulted identical to that of the solid PEI. The weight loss curves presented in Figure 4b show that an important amount of residual NMP stayed in the material even after 2 days of vacuum drying (6.4 wt%), explaining the high reduction in T_g observed by DSC. Once again, only after drying the materials for 7 days it was possible to fully eliminate the residual NMP (see in Figure 4b that no weight loss associated to NMP removal was observed in PEI and PEI-GnP foams after 7 days of drying).

3.2. Morphology and structure

The values of relative density, graphene nanoplatelets weight and volume percentages (respectively, w_{GnP} and v^s_{GnP} or v^f_{GnP}, the first one measured as volume percentage in the solid and the second one in the foam) and main cellular structure characterization results of PEI and PEI-GnP nanocomposite foams are compiled in Table 1 (thick foams) and Table 2 (thin foams). Generally speaking, all foams prepared in this study presented a homogenous cellular structure, with no major changes being observed comparing the cell size and structure between the top and bottom of the foams (see Figure 5).

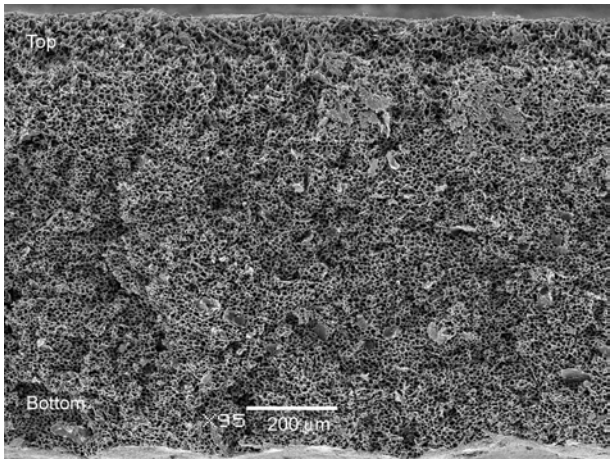

Figure 5. Typical micrograph of a PEI thin foam containing 2 wt% GnP

As can be seen from the results presented in the previous tables and the micrographs shown in Figure 6, slight changes in cellular structure were observed depending on the foam's composition and thickness of the sample. Foams displayed a quite isotropic spherical-like cellular morphology with expected porosity due to the nature of the water vapor-induced phase separation process.

The average cell size was in the interval 7.5–13.5 μm for PEI nanocomposite foams with a cell nucleation density of $6.90 \cdot 10^8$–$3.40 \cdot 10^9$ cells/cm^3. Generally speaking, the average cell size was in direct relation with the thickness of the foams, with the average cell size rising from roughly 8.5 μm for the thin foams to 13.6 μm for the thick foams. Logically, the higher surface area of thin samples allowed faster induc-

Table 1. Composition and cellular structure characteristics of the thick foams

Thickness [mm]	w_{GnP} [%]	v^s_{GnP} [%]	v^f_{GnP} [%]	Relative density	ϕ [μm]	N_0 [cells/cm^3]	N_f [cells/cm^3]
3.2	0.0	0.00	0.00	0.36	11.8	$1.40 \cdot 10^9$	$7.10 \cdot 10^8$
3.9	1.0	0.58	0.25	0.44	11.3	$1.30 \cdot 10^9$	$7.10 \cdot 10^8$
5.3	2.0	1.16	0.45	0.39	11.5	$1.40 \cdot 10^9$	$7.40 \cdot 10^8$
3.6	5.0	2.95	1.05	0.36	13.6	$1.10 \cdot 10^9$	$4.80 \cdot 10^8$
3.5	10.0	6.03	2.20	0.36	13.5	$6.90 \cdot 10^8$	$4.80 \cdot 10^8$

Table 2. Composition and cellular structure characteristics of the thin foams

Thickness [mm]	w_{GnP} [%]	v^s_{GnP} [%]	v^f_{GnP} [%]	Relative density	ϕ [μm]	N_0 [cells/cm^3]	N_f [cells/cm^3]
0.9	0.0	0.00	0.00	0.42	9.1	$2.90 \cdot 10^9$	$1.40 \cdot 10^9$
1.7	1.0	0.58	0.24	0.41	8.5	$2.20 \cdot 10^9$	$1.80 \cdot 10^9$
1.0	2.0	1.16	0.43	0.37	7.5	$3.40 \cdot 10^9$	$2.80 \cdot 10^9$
0.9	5.0	2.95	1.22	0.41	9.0	$2.20 \cdot 10^9$	$1.50 \cdot 10^9$
0.9	10.0	6.03	2.43	0.40	9.0	$2.20 \cdot 10^9$	$1.60 \cdot 10^9$

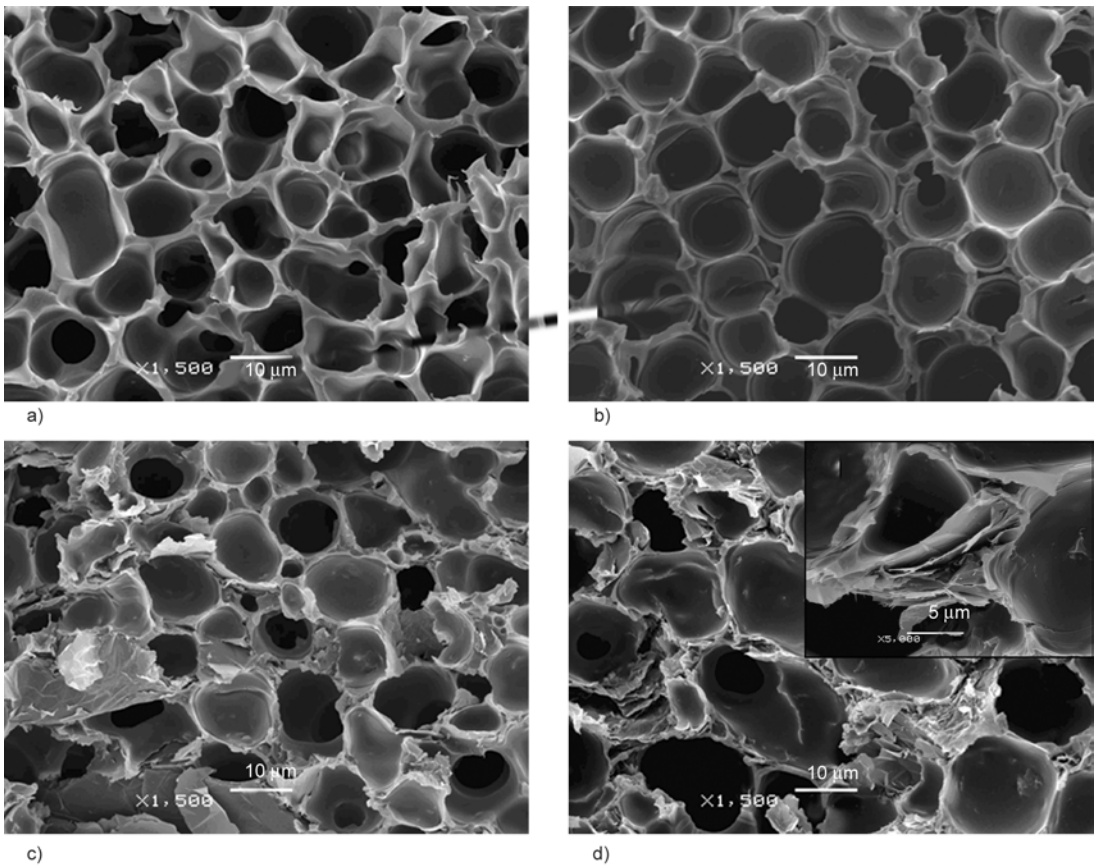

Figure 6. Typical micrographs of PEI (a, b) and PEI-GnP (c, d) foams showing the effect of thickness variation (thin foams: (a, c), thick foams: (b, d)) and addition of GnP on cellular morphology. See high magnification SEM micrograph insert showing the presence of GnP stacks in PEI + 10% GnP's foam cell strut.

tion of water into the solution, leading to the formation of smaller cells and thus to foams with finer cellular structures and higher cell densities.

The average cell size increased in thick foams with raising graphene concentration from approximately 11.5 to 13.5 µm, which could be a consequence of a higher barrier to the diffusion promoted by the GnP. Consequently, said results had a clear effect on the cell nucleation density of the foams, causing a decrease from $1.40 \cdot 10^9$ cells/cm^3 for the unfilled PEI foam to $6.90 \cdot 10^8$ cells/cm^3 for the 10 wt% graphene-reinforced foams, a 50% cell density reduction with increasing the amount of graphene nanoplatelets.

The analysis of the XRD spectra allowed the observation of eventual crystallinity in the polymer induced by the WVIPS foaming process and/or the presence of GnP, as well as possible changes on the (002) characteristic diffraction peak of GnP. As can be seen in Figure 7, on the one hand no significant changes were observed in terms of the characteristic amorphous halo of PEI in the unfilled PEI and PEI-GnP foams, meaning that neither foaming nor the addition of GnP induced PEI's crystallization.

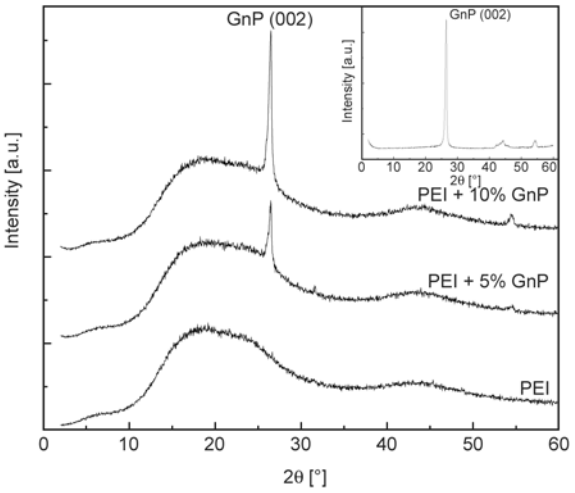

Figure 7. Characteristic XRD spectra of unfilled PEI and PEI-GnP foams. Insert: XRD spectrum of GnP.

On the other hand, the strong sharp diffraction signal at $2\theta = 26.5°$, corresponding to the reflection of graphene nanoplatelets' (002) crystal diffraction plane [24] (see insert in Figure 7), although is reduced with decreasing the concentration of nanoplatelets, does not fully disappear after foaming,

indicating that there is no full exfoliation of the graphene nanoplatelets [1, 14, 15].

3.3. Thermal stability

The thermogravimetric analysis (TGA) and respective first derivative (dTG) thermograms of the solid and foamed unfilled PEI and PEI-GnP nanocomposites were obtained under nitrogen atmosphere. As seen in Figure 8, a characteristic two-step thermal decomposition was observed for all samples with the following changes related to foaming and addition of graphene nanoplatelets: unfilled solid PEI showed this characteristic two-step decomposition, the first step being related to the decomposition of the non-aromatic part of PEI and the second one to the decomposition of the aromatic part (see PEI's repetitive unit presented in Figure 1), with a temperature corresponding to a 5 wt% loss of 524°C and a T_{max}, defined as the temperature of maximum mass loss rate, of 535°C. The unfilled PEI foam showed a similar two-step decomposition, although there was a faster onset of both first and second steps of the decomposition of 25°C for a 5 wt% loss and about 9°C for T_{max} when compared to unfilled solid PEI (see values presented in Table 3). The possible cause behind this earlier decomposition could be related to the presence of oxygen in the interior of foam cells, favoring local polymer thermal decomposition.

As can be seen in Figure 8, graphene-reinforced PEI foams, although globally showing a two-step decomposition similar to that of unfilled PEI, presented significant thermal decomposition delays during degradation, i.e., higher thermal stabilities, than the unfilled PEI foam, consequence of the effective physical barrier effect of graphene nanoplatelets dispersed throughout the cell walls (see TGA and respective dTG curves of pure GnP as an insert to Figure 8 showing the high thermal stability of GnP under nitrogen – total weight loss at 1000°C: 11.3 wt%).

Table 3. TGA and dTG results for thick unfilled PEI and PEI-GnP foams

w_{GnP} [%]	Temperature [°C]			Residue at 1000°C [wt%]
	5 wt% loss	40 wt% loss	T_{max}	
0.0 (solid)	523.8	675.1	535.3	48.3
0.0	496.2	614.0	526.0	48.4
1.0	506.3	616.9	531.3	51.7
2.0	513.0	621.0	535.5	52.0
5.0	501.8	614.3	526.8	52.7
10.0	513.5	668.8	531.6	55.8

An optimum concentration of 2 wt% GnP was found in terms of guaranteeing the maximum thermal stability in the earlier stages of thermal decomposition (see Figure 9), with PEI-GnP foams with higher GnP amounts (5 and 10 wt%) displaying faster decompositions. This behaviour was attributed to the existence of two competitive effects of GnP in terms of the thermal stability of the foam: on the one hand the already mentioned physical barrier effect of GnP, delaying the escape of volatiles from the pyrolysis in the same way as other fillers having similar platelet-like morphologies [25]; and on the other hand its inherently high thermal conductivity, explaining the faster thermal decomposition in the first decomposition stage of foams with higher GnP contents, counteracting GnP's barrier effect observed at lower amounts. In the second stage the high ther-

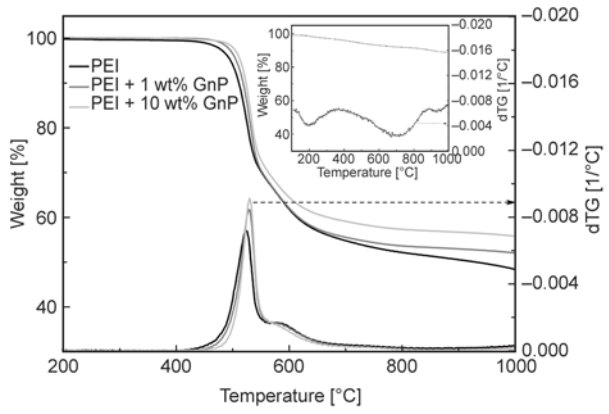

Figure 8. TGA and dTG thermograms of unfilled PEI and PEI-GnP foams. Insert: TGA and respective dTG thermogram of GnP.

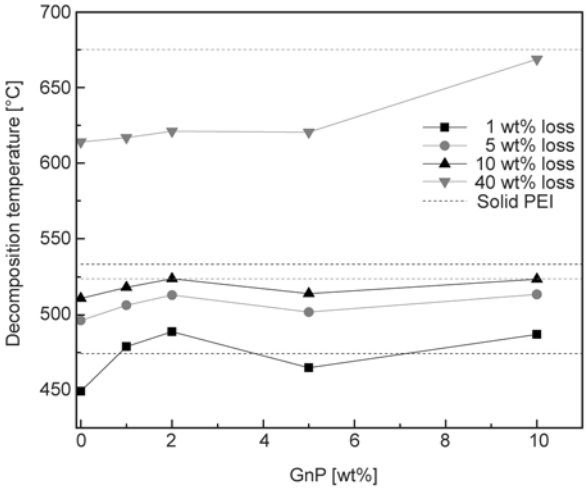

Figure 9. Evolution of the decomposition temperature of PEI-GnP nanocomposite foams with the amount of graphene nanoplatelets

mal conductivity of GnP seemed to have a lower influence on accelerating thermal decomposition, hence the significant increase in decomposition temperature corresponding to a 40 wt% loss for PEI foams with 10 wt% GnP (see Figure 9).

Particularly, PEI foams containing 1 wt% GnP showed 10 and 5°C decomposition delays respectively for 5 wt% loss and maximum decomposition rate temperature compared to the unfilled PEI foam. PEI foams with 2 and 10 wt% GnP showed similar trends, as can be seen in Table 3. On the contrary, 5 wt% GnP-reinforced PEI foam showed a delay in thermal decomposition that was lower than expected, which could be due to its lower relative density.

3.4. Dynamic-mechanical-thermal properties

The main results of the dynamic-mechanical-thermal analysis of the solid and foamed unfilled PEI and PEI-GnP nanocomposites, particularly the storage moduli (E'), the respective specific moduli (E'_{spec}), i.e., the storage modulus divided by the density of the material, and the glass transition temperatures (T_g), measured as the maximum of the transition peak in the tan δ curve, are presented in Figure 10.

As can be seen, PEI foams showed the typical behaviour of amorphous PEI, with the glass transition appearing on both loss modulus and tan δ curves, besides a molecular relaxation at 125°C, as the main signal (see Figure 10a).

Analyzing the glass transition temperature values of the foamed nanocomposites (Figure 10b), no significant increasing trend was observed with the addition of GnP, indicating that the interaction of the PEI with graphene's surface seemed to be poor. The foaming process itself seemed to promote a slight reduction of the glass transition temperature (223.5°C), with the highest T_g corresponding to the solid unfilled PEI (227°C), in good accordance with similar experimental results for porous materials. Comparatively, the T_g of PEI foams with 1 and 2 wt% GnP (respectively, 0.25 and 0.45 vol% GnP) was

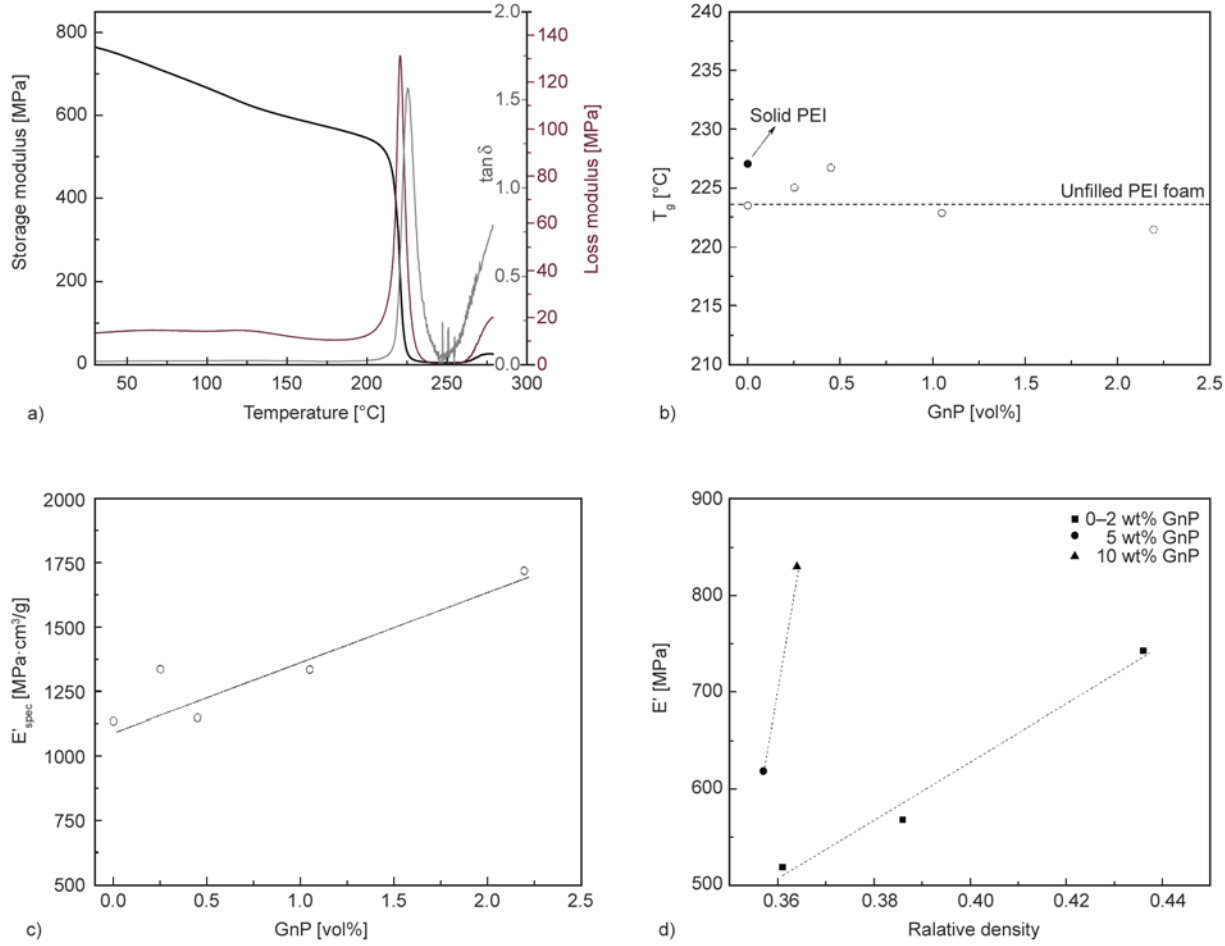

Figure 10. (a) Characteristic DMTA curves of PEI-GnP foams; (b) evolution of the glass transition temperature with GnP volume percentage measured in the foam (v^f_{GnP}); (c) evolution of the specific storage modulus with GnP volume percentage measured in the foam (v^f_{GnP}); and (d) evolution of the storage modulus with relative density.

slightly higher than that of unfilled PEI foam, which can be due to the higher relative density of these foams and might indicate an improved interaction between PEI's molecules and GnP. The slight decrease in T_g observed for PEI foams containing 5 and 10 wt% GnP (respectively, 1.05 and 2.20 vol% GnP) was related to a decrease in relative density.

The specific storage modulus (E'_{spec}) clearly increased with increasing the concentration of GnP, related to a higher stiffness of the graphene nanoplatelets (see Figure 10c). As expected, foams with higher relative densities presented higher values of the storage modulus, clearly exceeding that of the unfilled PEI foam (see Figure 10d).

3.5. Electrical conductivity

As expected, based on the intrinsically high transport properties of carbon-based materials, their addition into polymers and foaming has been used as a possible strategy to improve the low electrical conductivity of polymer foams, and therefore extend their uses to other sectors such as electronics. For instance, EMI shielding efficiency benefits with increasing electrical conductivity in foams, boosting their already intrinsic ability to absorb electromagnetic radiation [26]. Optimum nanoparticle distribution and dispersion is widely known to improve the transport properties of polymer-based nanocomposites. In previous works on PP [20] and polyurethane (PU) [4], we have shown that melt-compounding can improve graphene nanoplatelets dispersion and exfoliation. Nevertheless, this method requires high shear forces in order to avoid aggregation and guarantee a proper dispersion [27, 28]. In a study that considered the preparation and characterization of microcellular PEI-graphene composites, Ling *et al*. [19] verified that foams prepared by WVIPS presented promising electrical conductivity values. Their research showed that the electrical conductivity of foams increased from $4.8 \cdot 10^{-4}$ S/m for 5.87 vol% GnP to $2.2 \cdot 10^{-3}$ S/m for 1.38 vol% GnP, showing the effectiveness of foaming in improving the electrical conductivity of PEI-graphene nanocomposites.

The electrical conductivity enhancement achieved with the addition of graphene nanoplatelets was investigated, the results being shown in Figure 11. PEI is considered electrically insulating with an experimentally determined conductivity of $1.0 \cdot 10^{-15}$ S/m. Nanocomposite foams presented a dramatic increase up to $1.8 \cdot 10^{-7}$ S/m at 2.2 vol% GnP, indicating that a conductive network of graphene nanoplatelets was formed. As can be seen in Figure 11a, for GnP concentrations below 3 vol%, the electrical conductivity of foams followed a linear-like trend, indicating that the electrical properties of the nanocomposite foams were controlled by the concentration of GnP. Figure 11a depicts the electrical conductivity (σ) data as a function of GnP volume percentage relative to the foam and to the amount of solid material. The foamed nanocomposites presented a linear increase, indicating that GnP's distribution enhanced the electrical conductivity of the PEI foam.

Despite the fact that the electrical conductivity above a certain critical concentration is usually depicted based on a physical contact between conductive particles by means of a percolative behaviour given by $\sigma = (\phi - \phi_c)^v$, where σ is the conductivity of the material, ϕ is the volume fraction of particles, ϕ_c is the critical volume fraction of particles for electrical conduction and v is the percola-

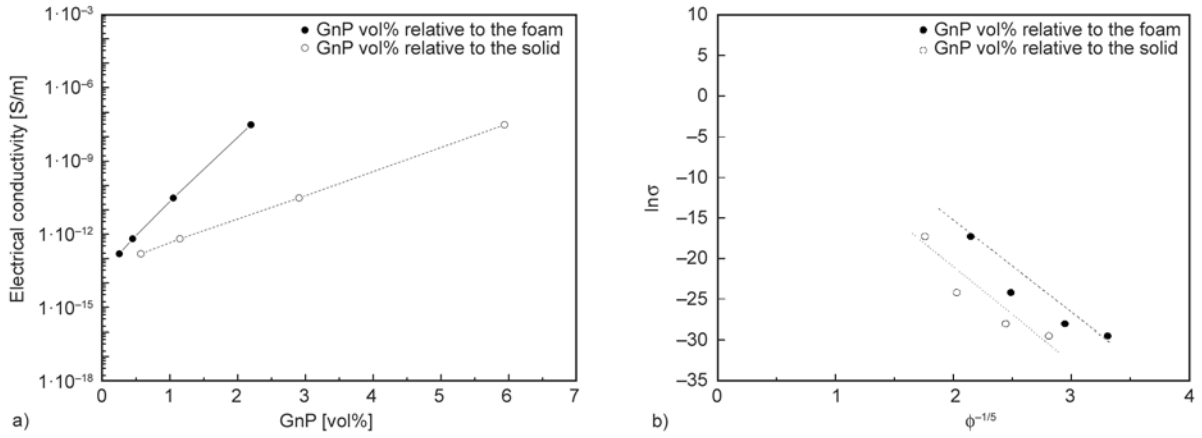

Figure 11. (a) Evolution of the electrical conductivity (σ) with GnP volume content and (b) representation of the fitting results of lnσ vs. $\phi^{-1/5}$

tion exponent [19, 29], a tunnel conduction mechanism was proposed in this study, as it has been shown to be a better model to predict the electrical conductivity of thermoplastic polymer foams containing conductive carbon-based particles [4, 20]. Tunneling was considered as the main conduction mechanism, first of all due to the concentration range of GnP and secondly to the fact that the percolation model does not consider that the samples are already electrically-conductive for GnP concentrations below the critical value. As recently shown, tunnel conduction is a better match for experiments with wide range of filler concentrations before the formation of a continuous conductive particle network in carbon-reinforced nanocomposites, as direct contact between conductive particles would lead to much higher final electrical conductivities [20, 30, 31].

If tunnel conduction is considered, the dc electrical conductivity can be described by $\sigma \propto \exp(-Ad)$, where A is the so-called tunnel parameter and d is the tunnel distance [32]. This tunnel distance (d) is directly proportional to ϕ^{-n}, where the value of n depends on the geometry and distribution of the conductive particles. In the particular case of a random spherical particle distribution, the mean average distance between particles has been proposed to be proportional to $\phi^{-1/3}$ [33], i.e., $n = 1/3$, while in the case of a three-dimensional random fibre network d is proportional to ϕ^{-1} ($n = 1$) [34]. We have shown in one of our previous works [20] that the electrical response of similar foams of PP containing variable concentrations of carbon nanofibres (CNFs) followed a tunnel-like behaviour, with foams showing higher electrical conductivities than the solid composites due to CNF aggregate rupture during foaming and excluded volume related to cell formation [35], pushing CNFs closer and effectively reducing d. These foams presented a behaviour that resembled that of a conductive network system formed by random-distributed conductive fibres ($n = 1$), while the solid composites showed an electrical behaviour where d was proportional to $\phi^{-1/3}$ (random-distributed spherical particles), showing that foaming promoted an effective CNF aggregate rupture.

In our present research the best fit to the electrical conductivity of the PEI-GnP foams assuming a tunnel-like approach led to a value of $n = 1/5$ (see representation of the fitting results in Figure 11b), which, according to values calculated by Krenchel [36] and Fisher *et al*. [37], is in good agreement with the existence of a GnP network with a three-dimensional random distribution, which, albeit the non-full exfoliation of GnP shown by XRD, seem to indicate that foaming promoted a proper distribution of GnP stacks.

4. Conclusions

This work presents the preparation by WVIPS and characterization of PEI foams reinforced with variable amounts of graphene nanoplatelets regarding the structure and morphology of the foams, their thermal stability, thermo-mechanical behaviour and electrical conductivity, with the main objective of developing multifunctional foams for advanced applications.

Although all foams presented a characteristic homogeneous cellular morphology, slight changes were observed depending on foam thickness and amount of GnP. The average cell size increased and cell density decreased with increasing foam thickness, related to the higher surface area of the thinner foams. Additionally, cell size increased with augmenting the amount of GnP. XRD analysis revealed that there was not any significant GnP exfoliation after foaming or any occurrence of PEI's crystallization.

A characteristic two-step thermal decomposition was observed for the unfilled and graphene-reinforced solid and foamed PEI, with graphene-reinforced foams showing significantly higher thermal stabilities than the unfilled PEI foam. The maximum thermal stability for PEI-GnP foams in the earlier stages of foaming was found at 2 wt% GnP, with further GnP addition leading to reduced thermal stabilities.

In terms of the viscoelastic response, foaming promoted a slight reduction in the T_g of PEI. The addition of GnP did not lead to significant differences in T_g, its value mainly depending on relative density. The specific storage modulus of foams significantly increased with incrementing the concentration of GnP, clearly exceeding that of unfilled PEI foam, proving the effective function of GnP as strengthening filler.

The addition of GnP to PEI and later foaming led to foams with mild electrical conductivity values, which increased with increasing the concentration of GnP. A tunnel-like conduction mechanism assuming a three-dimensional random distribution of con-

ductive particles was shown to fit well to the evolution of the electrical conductivity of the foams with GnP's concentration.

Acknowledgements

The authors would like to acknowledge the Spanish Ministry of Economy and Competitiveness for the financial support of project MAT2011-26410.

References

[1] Antunes M., Gedler G., Velasco J. I.: Multifunctional nanocomposite foams based on polypropylene with carbon nanofillers. Journal of Cellular Plastics, **49**, 259–279 (2013).
DOI: 10.1177/0021955X13477433

[2] Antunes M., Velasco J. I., Realinho V.: Polypropylene foams. Production, structure and properties. in 'Advances in materials science research' (ed.: Wythers M. C.) Nova Science Publishers, New York, Vol 10, 123–154 (2011).

[3] Klempner D., Sendijarevic V.: Handbook of polymeric foams and foam technology. Hanser, Munich (2004).

[4] Antunes M., Velasco J. I.: Multifunctional polymer foams with carbon nanoparticles. Progress in Polymer Science, **39**, 486–509 (2014).
DOI: 10.1016/j.progpolymsci.2013.11.002

[5] Geim A. K., Novoselov K. S.: The rise of graphene. Nature Materials, **6**, 183–191 (2007).
DOI: 10.1038/nmat1849

[6] Dreyer D. R., Park S., Bielawski C. W., Ruoff R. S.: The chemistry of graphene oxide. Chemical Society Reviews, **39**, 228–240 (2010).
DOI: 10.1039/B917103G

[7] Wang G., Yang J., Park J., Gou X., Wang B., Liu H., Yao J.: Facile synthesis and characterization of graphene nanosheets. The Journal of Physical Chemistry C, **112**, 8192–8195 (2008).
DOI: 10.1021/jp710931h

[8] Wang G., Shen X., Wang B., Yao J., Park J.: Synthesis and characterisation of hydrophilic and organophilic graphene nanosheets. Carbon, **47**, 1359–1364 (2009).
DOI: 10.1016/j.carbon.2009.01.027

[9] Salavagione H. J., Martínez G., Gómez M. A.: Synthesis of poly(vinyl alcohol)/reduced graphite oxide nanocomposites with improved thermal and electrical properties. Journal of Materials Chemistry, **19**, 5027–5032 (2009).
DOI: 10.1039/B904232F

[10] Xu Y., Hong W., Bai H., Li C., Shi G.: Strong and ductile poly(vinyl alcohol)/graphene oxide composite films with a layered structure. Carbon, **47**, 3538–3543 (2009).
DOI: 10.1016/j.carbon.2009.08.022

[11] Villar-Rodil S., Paredes J. I., Martínez-Alonso A., Tascón J. M.: Preparation of graphene dispersions and graphene-polymer composites in organic media. Journal of Materials Chemistry, **19**, 3591–3593 (2009).
DOI: 10.1039/B904935E

[12] Liu N., Luo F., Wu H., Liu Y., Zhang C., Chen J.: One-step ionic-liquid-assisted electrochemical synthesis of ionic-liquid-functionalized graphene sheets directly from graphite. Advanced Functional Materials, **18**, 1518–1525 (2008).
DOI: 10.1002/adfm.200700797

[13] Bhadra S., Khastgir D., Singha N. K., Lee J. H.: Progress in preparation, processing and applications of polyaniline. Progress in Polymer Science, **34**, 783–810 (2009).
DOI: 10.1016/j.progpolymsci.2009.04.003

[14] Song P., Cao Z., Cai Y., Zhao L., Fang Z., Fu S.: Fabrication of exfoliated graphene-based polypropylene nanocomposites with enhanced mechanical and thermal properties. Polymer, **52**, 4001–4010 (2011).
DOI: 10.1016/j.polymer.2011.06.045

[15] Gedler G., Antunes M., Realinho V., Velasco J. I.: Thermal stability of polycarbonate-graphene nanocomposite foams. Polymer Degradation and Stability, **97**, 1297–1304 (2012).
DOI: 10.1016/j.polymdegradstab.2012.05.027

[16] Kim H., Macosko C. W.: Processing-property relationships of polycarbonate/graphene composites. Polymer, **50**, 3797–3809 (2009).
DOI: 10.1016/j.polymer.2009.05.038

[17] Yasmin A., Luo J. J., Abot J. L., Daniel I. M.: Mechanical and thermal behavior of clay/epoxy nanocomposites. Composites Science and Technology, **66**, 2415–2422 (2006).
DOI: 10.1016/j.compscitech.2006.03.011

[18] Jiang W., Sundarram S. S., Wong D., Koo J. H., Li W.: Polyetherimide nanocomposite foams as an ablative for thermal protection applications. Composites Part B: Engineering, **58**, 559–565 (2014).
DOI: 10.1016/j.compositesb.2013.10.040

[19] Ling J., Zhai W., Feng W., Shen B., Zhang J., Zheng W. G.: Facile preparation of lightweight microcellular polyetherimide/graphene composite foams for electromagnetic interference shielding. ACS Applied Materials and Interfaces, **5**, 2677–2684 (2013).
DOI: 10.1021/am303289m

[20] Antunes M., Mudarra M., Velasco J. I.: Broad-band electrical conductivity of carbon nanofibre-reinforced polypropylene foams. Carbon, **49**, 708–717 (2011).
DOI: 10.1016/j.carbon.2010.10.032

[21] Yang G., Su J., Gao J., Hu X., Geng C., Fu Q.: Fabrication of well-controlled porous foams of graphene oxide modified poly(propylene-carbonate) using supercritical carbon dioxide and its potential tissue engineering applications. The Journal of Supercritical Fluids, **73**, 1–9 (2013).
DOI: 10.1016/j.supflu.2012.11.004

[22] Zaman I., Kuan H-C., Meng Q., Michelmore A., Kawashima N., Pitt T., Zhang L., Gouda S., Luong L., Ma J.: A facile approach to chemically modified graphene and its polymer nanocomposites. Advanced Functional Materials, **22**, 2735–2743 (2012).
DOI: 10.1002/adfm.201103041

[23] Sims G. L. A., Khunniteekool C.: Cell size measurement of polymeric foams. Cellular Polymers, **13**, 137–146 (1994).

[24] Pham T. A., Kim J. S., Kim J. S., Jeong Y. T.: One-step reduction of graphene oxide with L-glutathione. Colloids and Surfaces A: Physicochemical and Engineering Aspects, **384**, 543–548 (2011).
DOI: 10.1016/j.colsurfa.2011.05.019

[25] Realinho V., Haurie L., Antunes M., Velasco J. I.: Thermal stability and fire behaviour of flame retardant high density rigid foams based on hydromagnesite-filled polypropylene composites. Composites Part B: Engineering, **58**, 553–558 (2014).
DOI: 10.1016/j.compositesb.2013.11.015

[26] Gelves G. A., Al-Saleh M. H., Sundararaj U.: Highly electrically conductive and high performance EMI shielding nanowire/polymer nanocomposites by miscible mixing and precipitation. Journal of Materials Chemistry, **21**, 829–836 (2011).
DOI: 10.1039/C0JM02546A

[27] Tang W., Santare M. H., Advani S. G.: Melt processing and mechanical property characterization of multi-walled carbon nanotube/high density polyethylene (MWNT/HDPE) composite films. Carbon, **41**, 2779–2785 (2003).
DOI: 10.1016/S0008-6223(03)00387-7

[28] Thostenson E. T., Chou T-W.: Aligned multi-walled carbon nanotube-reinforced composites: Processing and mechanical characterization. Journal of Physics D: Applied Physics, **35**, L77–L80 (2002).
DOI: 10.1088/0022-3727/35/16/103

[29] Stankovich S., Dikin D. A., Dommett G. H. B., Kohlhaas K. M., Zimney E. J., Stach E. A., Piner R. D., Nguyen S. T., Ruoff R. S.: Graphene-based composite materials. Nature, **442**, 282–286 (2006).
DOI: 10.1038/nature04969

[30] Barrau S., Demont P., Peigney A., Laurent C., Lacabanne C.: DC and AC conductivity of carbon nanotubes–polyepoxy composites. Macromolecules, **36**, 5187–5194 (2003).
DOI: 10.1021/ma021263b

[31] Linares A., Canalda J. C., Cagiao M. E., García-Gutiérrez M. C., Nogales A., Martín-Gullón I., Vera J., Ezquerra T. A.: Broad-band electrical conductivity of high density polyethylene nanocomposites with carbon nanoadditives: Multiwall carbon nanotubes and carbon nanofibers. Macromolecules, **41**, 7090–7097 (2008).
DOI: 10.1021/ma801410j

[32] Ryvkina N., Tchmutin I., Vilčáková J., Pelíšková M., Sáha P.: The deformation behavior of conductivity in composites where charge carrier transport is by tunneling: Theoretical modeling and experimental results. Synthetic Metals, **148**, 141–146 (2005).
DOI: 10.1016/j.synthmet.2004.09.028

[33] Hull D., Clyne T.: An introduction to composite materials. Cambridge University Press, New York (1996).

[34] Allaoui A., Hoa S. V., Pugh M. D.: The electronic transport properties and microstructure of carbon nanofiber/epoxy composites. Composites Science and Technology, **68**, 410–416 (2008).
DOI: 10.1016/j.compscitech.2007.06.028

[35] Yang Y., Gupta M. C., Dudley K. L., Lawrence R. W.: Conductive carbon nanofiber–polymer foam structures. Advanced Materials, **17**, 1999–2003 (2005).
DOI: 10.1002/adma.200500615

[36] Krenchel H.: Fibre reinforcement. Akademisk Forlag, Copenhagen (1964).

[37] Fisher F. T., Bradshaw R. D., Brinson L. C.: Fiber waviness in nanotube-reinforced polymer composites – I: Modulus predictions using effective nanotube properties. Composites Science and Technology, **63**, 1689–1703 (2003).
DOI: 10.1016/S0266-3538(03)00069-1

eXPRESS Polymer Letters Vol.9, No.5 (2015) 424–434
Available online at www.expresspolymlett.com
DOI: 10.3144/expresspolymlett.2015.41

Solution viscosity – molar mass relationships for poly(butylene succinate) and discussion on molar mass analysis

Q. Charlier[1,2], E. Girard[1,2], F. Freyermouth[1,2], M. Vandesteene[1,2], N. Jacquel[3], C. Ladavière[1,4], A. Rousseau[1,2], F. Fenouillot[1,2]*

[1]Université de Lyon, F-69003 Lyon, France
[2]INSA-Lyon, Ingénierie des Matériaux Polymères, IMP, CNRS UMR5223, F-69621 Villeurbanne, France
[3]Roquette Frères, Division Recherche, F-62080 Lestrem, France
[4]Université de Lyon, CNRS UMR5223, IMP@Lyon 1, 15 Boulevard Latarjet, F-69622 Villeurbanne, France

Received 23 September 2014; accepted in revised form 27 November 2014

Abstract. Poly(butylene succinate) (PBS) is currently developing due to its biodegradability and the similarity of its mechanical properties to those of polyolefins. Relationships between the number average molar mass, $\overline{M}_n$, and solution viscosity such as [η] and η_{red} were derived for this aliphatic polyester. $\overline{M}_n$ values were determined by end-group analysis and size exclusion chromatography (SEC). Mark-Houwink-Sakurada (MHS) parameters were proposed in two solvents and for the different molar masses and viscosity measurement methods. As an example, the MHS equations were respectively, $[\eta] = 6.4 \cdot 10^{-4} \cdot M_n^{0.67}$ in chloroform and $[\eta] = 7.1 \cdot 10^{-4} \cdot \overline{M}_n^{0.69}$ in 50/50 wt% 1,2-dichlorobenzene/phenol at 25°C for molar masses measured by SEC in hexafluoro isopropanol (HFIP) with poly(methyl methacrylate) (PMMA) standards. Empirical relationships were also suggested to derive $\overline{M}_n$ directly from reduced viscosity, η_{red}, which is much easier to determine than intrinsic viscosity. With these data, the number average molar mass of PBS can be conveniently estimated from a single viscosity measurement. In addition, it was shown that PBS contains 1–2 wt% of cyclic oligomers produced during esterification and that molar masses determined by taking this fraction into account or not were significantly different, especially for long chains.

Keywords: *biopolymers, poly(butylene succinate), molar mass, cyclic oligomers*

1. Introduction

Poly(butylene succinate) (PBS) is one of the 'old' polyesters which regains interest because of the current preoccupation with the environment [1–3]. It is biodegradable and can be bio-based. Its thermal and mechanical properties are close to those of polyolefins and its processability is excellent while its durability is much lower due to possible hydrolysis. Indeed it recently drew attention from academia and industry [4–9] and now, the producers are trying to find applications in agriculture, fishery, forestry, civil engineering and other fields in which recycling of materials is challenging.

Poly(butylene succinate) is not a new polymer however it was not developed commercially in the 1950s or 1960s as was done with commodity polymers. As a consequence research has not been very active until now and basic data on PBS may be missing. Here we will focus on the topic of molar mass determination of PBS.

There are several ways to determine the number and weight average molar masses ($\overline{M}_n$, $\overline{M}_w$) of a

*Corresponding author, e-mail: Francoise.Fenouillot@insa-lyon.fr

polymer such as end-group analysis by titration or by ^{1}H-NMR spectroscopy ($\overline{M}_n$), size exclusion chromatography (SEC) ($\overline{M}_n$, $\overline{M}_w$ and $\overline{M}_z$), ($\overline{M}_n$), membrane osmometry ($\overline{M}_n$), light-scattering (M_w), and viscometric method ($\overline{M}_v$) [10, 11].

Viscometry is a quick and simple method if dispersity data are not needed. It involves measuring the viscosity of dilute solutions of the polymer, from which the molar mass may be calculated since the relationship between the intrinsic viscosity, [η], and the viscosity-average molar mass, $\overline{M}_v$, can be described by the well-known Mark-Houwink-Sakurada (MHS) equation (Equation (1)):

$$\eta = k \cdot \overline{M}_v^a \quad (1)$$

where k and a are constants for a given well-defined polymer-solvent-temperature system. In general, $\overline{M}_v$ is not experimentally accessible, and in most reports, different average molecular masses ($\overline{M}_n$, $\overline{M}_w$ and $\overline{M}_z$), instead of the viscosity–average molar mass $\overline{M}_v$, are substituted in the MHS equation, ignoring dispersity effects [12–14]. For poly(butylene succinate) k and a parameters are poorly defined in the literature [15–17].

On the other hand only size exclusion chromatography provides information on the molar mass distribution but it is not an easy technique for aromatic polyesters due to their poor solubility in commonly used SEC eluents. Aliphatic polyesters are more soluble but other difficulties arise. As an example, PBS is soluble in chloroform at room temperature but the refractive indexes of the polymer and the solvent are very close to each other ($dn/dc \sim 5 \cdot 10^{-2}$ mL·g^{-1}) so inaccuracies are observed. The above comment illustrates one of the reasons why the determination of molar mass by SEC with a refractive index or light scattering detector for polyesters is controversial in chloroform. Several authors have recently highlighted that polystyrene-calibrated SEC measurements in chloroform overestimate the real $\overline{M}_n$ by at least 50% in the range above 10^4 g·mol^{-1} for poly(ε-caprolactone), polylactide and related copolyesters [18–24]. For these reasons, researchers have used complementary techniques such as MALDI-TOF mass spectrometry [19, 25]. Also, commercial polyesters often contain a fraction of cyclic oligomers, which may significantly affect the calculation of $\overline{M}_n$. These inaccuracies are especially critical if the actual molar mass is needed with the aim of modelling polymerization or chemically modifying end-groups.

In this context, the objectives of this work were to provide information on the uncertainties attached to molar mass determination of PBS and develop a methodology to conveniently determine it. To this end, a series of linear PBS was synthesized, different methods for molar mass determination were explored, and the impact of the oligomer content on the data was estimated.

2. Experimental

2.1. PBS synthesis

A series of PBS samples with increasing molar mass were synthesized from succinic acid (SA) (99% min, GADIV Petrochemical Ind., Haifa, Israel) and 1,4-butanediol (BDO) (99%, Sigma-Aldrich, Saint-Quentin-Fallavier, France) via a two-step melt polycondensation reaction described in detail elsewhere [26]. Titanium (IV) n-butoxide (97%, Sigma-Aldrich, Saint-Quentin-Fallavier, France) was used as the catalyst with 400 ppm of Ti present in the final polymer.

Seven PBS samples were collected. The pellets were dried and stored in sealed aluminium bags. The first, PBS1, was collected after the esterification step. The others, denoted PBS2 to PBS7, were collected when the stirring torque variation reached 0.1, 0.5, 1, 3, 16, and 22.5 Nm, respectively. They are numbered PBS1 to PBS7 in the order of increasing molar mass.

2.2. Intrinsic viscosity and reduced viscosity determination

An automated viscometer (AVS310, Schott Geräte, Hofheim, Germany), was used to determine the intrinsic viscosities of the PBS samples at 25±0.05°C in 50/50 wt% 1,2-dichlorobenzene/phenol (solvent for the standard DIN53728) and in chloroform. The capillary diameter was 0.84 mm for the analysis in 50/50 wt% 1,2-dichlorobenzene/phenol and 0.36 mm in chloroform in order to have sufficient accuracy for the flow time data. The PBS samples were solubilized at room temperature in both solvents. The solution viscosities were measured for four PBS concentrations varying from 2.5 to 10 g·L^{-1} in quadruplicate. The reduced viscosity, η_{red}, is the viscosity measured with a concentration equal to 5 g·L^{-1}.

2.3. Molar mass determination by size exclusion chromatography (SEC)

Polymer molar mass was assessed by size exclusion chromatography coupled to a UV detector (UV-272) and a refractive index (RI) detector (RI-1100) (Agilent, Germany, Waldbronn). 1 g·L^{-1} samples were eluted at a flow rate of 0.75 mL·min^{-1} with 1,1,1,3,3,3-hexafluoro-2-propanol (HFIP). The average molar masses $\overline{M}_n$ and $\overline{M}_w$ were determined with calibration method using poly(methyl methacrylate) (PMMA) standards. Calculation of the average molar masses was done using two methods, integrating low molar mass species between 100 and 1000 g·mol^{-1} or not.

2.4. Molar mass determination by hydroxyl and carboxyl end-group contents

Hydroxyl and carboxylic end-group concentrations, N_{HC} and N_{CC}, were determined by ^{1}H NMR spectroscopy. A liquid state NMR spectrometer equipped with a BBFO+ probe at 25°C was used (Avance III 400 MHz, Brucker, Wissembourg, France). Polymer samples were dissolved in deuterated chloroform containing tetramethylsilane (TMS) before analysis and trifluoroacetic anhydride (TFAA) was added to shift the $\underline{CH_2}OH$ and $\underline{CH_2}COOH$ signals of the hydoxyl and carboxylic end-groups (downfield shift of ~0.6 ppm) [18]. The number of scans was 256.

2.5. Oligomer extraction and characterization

To assess the quantity of the oligomers, 5 g of PBS samples were dispersed in 40 g of tetrahydrofurane (THF) over a period of three days under stirring. The dissolved oligomers were collected and the amount was quantified after evaporation at 25°C until a constant weight.

PBS oligomers were first analyzed by SEC (Shimadzu, DGU-20A3 + LC-20AD, Japan) with THF as the eluent. 5 g·L^{-1} samples were injected in three 5 µm columns containing Waters Styragel HR2THF, HR1THF and HR0.5THF at 1 mL·min^{-1}. $\overline{M}_n$ and $\overline{M}_w$ were determined with a calibration method using polystyrene standards.

To compare the molar masses and to identify the nature (cyclic or linear) of the oligomers, the samples extracted with THF were analyzed by MALDI-TOF mass spectroscopy. All MALDI-TOF mass spectra were obtained with a Voyager-DE PRO (Applied Biosystems, Framingham, MA) equipped with a nitrogen laser emitting at 337 nm with a 3 ns pulse duration. The instrument was operated in reflector mode. The ions were accelerated under a potential of 20 kV. The positive ions were detected in all cases. The mass spectra were the sum of 300 shots and external mass calibration of the mass analyzer was used (a mixture of peptides, Sequazyme, Applied Biosystems, Framingham, MA). Samples were prepared by mixing 10 µL of 2-(4′-hydroxyphenylazo) benzoic acid (HABA) at 0.1 M in chloroform/THF 50/50 v/v with 10 µL of sample (at 5 g·L^{-1} in THF). The resulting mixtures (0.5 µL) were spotted on the MALDI sample plate and air-dried.

3. Results and discussion

3.1. Intrinsic viscosity determination

The intrinsic viscosity was determined for the seven PBS samples by two different methods:

1. At different concentrations, then extrapolation to infinite dilution.
2. *Via* the single-point method based on the solution's specific viscosity, η_{sp}, and reduced viscosity, η_{red}, at only one specific concentration (C = 5 g·L^{-1}).

3.1.1. Method using different concentrations

The flow time of the pure solvent, t_0, and of four different PBS concentrations, t, was measured. Based on these time values, the specific viscosity η_{sp} and the relative viscosity η_{rel} were calculated using Equations (2) and (3):

$$\eta_{rel} = \frac{t}{t_0} \tag{2}$$

$$\eta_{sp} = \frac{t - t_0}{t_0} = \eta_{rel} - 1 \tag{3}$$

The intrinsic viscosity can be determined when η_{sp} and η_{rel} are known (Equation (4) and (5)):

$$[\eta] - k_1[\eta]^2 C = \frac{\eta_{sp}}{C} \tag{4}$$

$$[\eta] - k_2[\eta]^2 C = \frac{\ln \eta_{rel}}{C} \tag{5}$$

where k_1 and k_2 are the Huggins and Kramer coefficients, respectively and C is the concentration of the polymer solution in g·L^{-1}.

For each PBS, η_{sp}/C and $(\ln \eta_{rel})/C$ were plotted against the concentration C (Huggins and Kramer

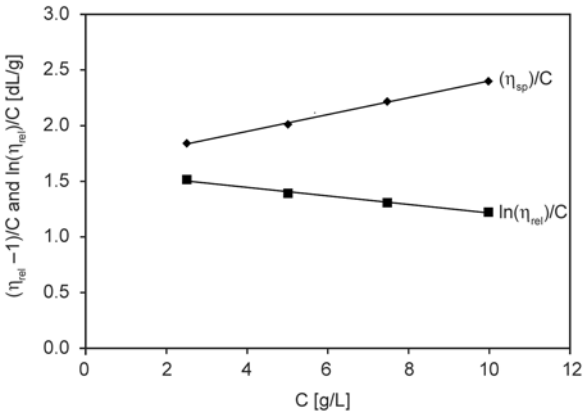

Figure 1. A typical Huggins-Kramer dual extrapolation plot for PBS7 (M_n = 55,550 g·mol^{-1} by SEC in HFIP *versus* PMMA standards) in 50/50 wt% 1,2-dichlorobenzene/phenol at 25°C. (♦) $(\eta_{sp})/C$, (■) $(\ln\eta_{rel})/C$.

plots) and the intrinsic viscosity was obtained by extrapolating the plots to infinite dilution [27]. An example of such a graph for PBS 7 is given in Figure 1.

The intrinsic viscosity data of PBS samples at 25°C in 50/50 wt% 1,2-dichlorobenzene/phenol and in chloroform are listed in Table 1.

3.1.2. Method using a single-point

The intrinsic viscosity, $[\eta]$, can be estimated with the measurement of specific viscosity, η_{sp}, and relative viscosity, η_{rel}, for a single concentration with Equations (6), (7) and (8) [28–30]:

$$\text{Solomon and Ciuta: } [\eta] = \frac{\sqrt{2(\eta_{sp} - \ln\eta_{rel})}}{C} \quad (6)$$

$$\text{Kuwahara: } [\eta] = \frac{\eta_{sp} + 3\ln\eta_{rel}}{4C} \quad (7)$$

$$\text{Rao and Yaseen: } [\eta] = \frac{\eta_{sp} + \ln\eta_{rel})}{2C} \quad (8)$$

The previous method of Huggins and Kramer at different concentrations and the single-point method play two separate roles in characterizing the molar mass of polymers. The method of Huggins and Kramer is employed for procuring accurate information on the intrinsic viscosity, while the single-point method is fast for a reasonable estimation but is widely criticized in the literature. Both methods are consistent for some polymer-solvent couples but only if the solution has a low concentration (≤0.2%) and low specific viscosity between 0.15 and 0.30 [27–32]. In most published studies where viscosity measurements were performed with PBS, these measurements were carried out in chloroform at 25 or 30°C [25, 33–35]. Some use the method developed by Huggins and Kramer [25, 33] while others prefer the single-point method. In this case, the most used equation is the one of Solomon and Ciuta [33, 34]. The concentration used for the single-point method was 2.5 g·L^{-1}. Viscosity data extracted with the two methods are shown in Table 1.

Table 1. Comparison of $[\eta]$ of PBS determined from the Huggins and Kramer plots and from the single-point method determined in 50/50 wt% 1,2-dichlorobenzene/phenol and chloroform at 25°C

		[η] (dL/g) (±0.01 dL·g^{-1})			
Solvent	PBS sample	Huggins-Kramer dual extrapolation	Single point method[a)]		
			Solomon and Ciuta	Kuwaraha	Rao and Yaseen
50 :50 1,2-dichlorobenzene/phenol	PBS1	0.11	0.11	0.11	0.11
	PBS2	0.33	0.33	0.33	0.34
	PBS3	0.67	0.67	0.66	0.68
	PBS4	0.81	0.83	0.82	0.84
	PBS5	1.30	1.29	1.28	1.33
	PBS6	1.50	1.48	1.46	1.53
	PBS7	1.62	1.62	1.60	1.68
Chloroform	PBS1	0.08	0.08	0.08	0.08
	PBS2	0.25	0.25	0.24	0.25
	PBS3	0.50	0.50	0.49	0.50
	PBS4	0.57	0.57	0.57	0.58
	PBS5	0.89	0.89	0.89	0.91
	PBS6	0.99	0.99	0.99	1.01
	PBS7	1.07	1.08	1.07	1.10

[a)]data determined for a concentration of 2.5 g·L^{-1}.

The data suggest that estimating [η] of PBS using single-point calculation fits quite well with more than 97% accuracy recorded at relatively low concentrations and when the specific viscosity η_{sp} is not higher than 0.2.

3.2. Molar mass determination by end-groups analysis

To calculate the equivalent Mark-Houwink-Sakurada parameters, the next step was to determine the molar mass of the PBS samples. Two methods were accessible: end-groups analysis and size exclusion chromatography. Both were done with and without an estimation of the cyclic oligomers fraction.
End-groups analysis is presented first.

3.2.1. End-groups analysis (without cyclic oligomers)

The molar masses of PBS samples can be calculated if the chain end-groups content is known (Equation (9)):

$$\overline{M}_n = \frac{1}{\frac{N_{CC} + N_{HC}}{2}} \quad (9)$$

where N_{HC} is the hydroxyl end group content, and N_{CC} is the carboxylic acid end group content, both measured by ^{1}H-NMR and expressed in mol·g^{-1}.

The carboxylic end-group concentration cannot be determined with a simple analysis in chloroform containing TMS because their signals superimpose to the 2.6 ppm peak which corresponds to the succinic acid methylene groups inserted in the chains. The addition of trifluoroacetic anhydride (TFAA) which reacts quantitatively with both hydroxyl and carboxylic acid end-groups is necessary. As a consequence of that reaction, the peak corresponding to hydroxyl end-groups shifts downfield from 3.6 to 4.4 ppm (H5), and two peaks corresponding to carboxylic end-groups appear at 2.7 ppm (H2) and 2.9 ppm (H3) (Figure 2).
The N_{HC} and N_{CC} end-group concentrations were calculated using Equations (10) and (11):

$$N_{HC} = \frac{\frac{I_{H5}}{2}}{\sum I_{PBS}} \cdot \frac{2}{M_{PBS}} \quad (10)$$

$$N_{CC} = \frac{\frac{I_{COOH\ at\ 2.9\ ppm}}{2}}{\sum I_{PBS}} \cdot \frac{2}{M_{PBS}} \quad (11)$$

where M_{PBS} is the molar mass of the repeat unit (172 g·mol^{-1}). I_{H5} is the integral of trifluoroacetylated PBS hydroxyl end-groups at 4.4 ppm

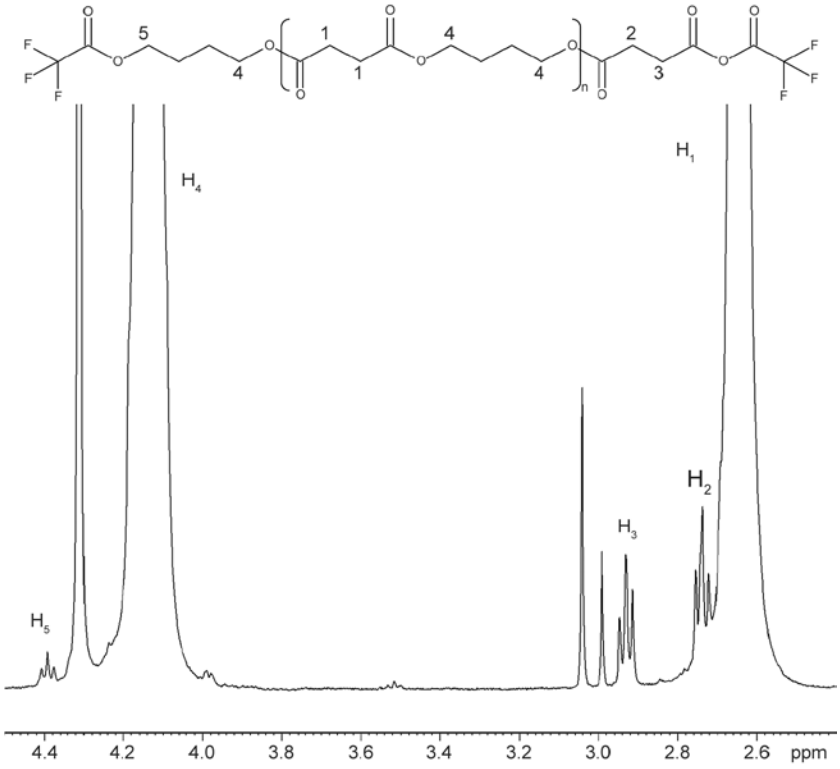

Figure 2. ^{1}H NMR spectrum of a sample of a trifluoroacetylated PBS (solvent: $CDCl_3$) at 25°C

(–$\underline{CH_2}OCOCF_3$) and ΣI_{PBS} is the sum of the integrals from all monomer units in the chains of PBS (Equation (12)):

$$\sum I_{PBS} = \frac{I_{H3}}{2} + \frac{I_{H5}}{2} + \frac{I_{H1}}{4} + \frac{I_{H4}}{4} \quad (12)$$

where I_{H1} is the integral at 2.6 ppm, referring to the methylene groups of succinic acid units in PBS and the peak at 4.2 ppm, referring to butanediol units in PBS.

N_{HC}, N_{CC} data and the resulting molar masses of the PBS series are detailed in Table 2.

3.2.2. End-groups analysis taking into account cyclic oligomers

As reported in the literature, the synthesis of PBS may produce a non negligible amount of oligomers, especially cyclic species [18, 19]. Most of the time, in scientific studies, PBS is purified to get rid of these species but commercial PBS clearly contains oligomers since dissolution/precipitation steps are not performed. In some cases it may be of importance to be able to account for their presence.

Equation (9) is not adapted for calculating the molar mass of a polymer that contains cycles. Indeed cyclic oligomers do not contain chain-ends, thus the molar mass derived with Equation (9) is overestimated since cycles monomer units are considered as being integrated into the linear chains population. It is possible to modify Equation (9) to account for cyclic oligomers only if their fraction and molar mass are known.

To this purpose, the mass fraction of cyclic oligomers, w_{cyclic}, of PBS samples was evaluated by extraction in THF and was found to be equal to 1–2 wt% (Table 2). The SEC analysis of the extractible fraction clearly shows four main elution peaks corresponding to species with estimated molar masses of 355, 487, 630 and 801 g·mol^{-1} (Figure 3a). These four populations corresponding to cyclic oligomers could be discriminated more accurately by MALDI-TOF mass spectrometry: C2 (367.1 *m/z*), C3 (539.2 *m/z*), C4 (711.3 *m/z*), and C5 (883.3 *m/z*) corresponding respectively to Na^+ cationized cyclic oligomers composed of 2, 3, 4 and 5 repeat units, i.e. DPn = 4, 6, 8 and 10 (Figure 3b). The average molar mass, $\overline{M}_{cyclic}$, was calculated with the help of SEC and MALDI-TOF mass spectrometry data (Table 2). The cyclic oligomer content, N_c, may be expressed in mol·g^{-1} with Equation (13):

$$N_c = \frac{w_{cyclic}}{\overline{M}_{cyclic}} \quad (13)$$

Then a corrected value of $\overline{M}_n$ which includes cycles may be calculated with Equation (14):

$$M_{n\,cor} = \frac{1}{\frac{w_{cyclic}}{M_{cyclic}} + \frac{N_{CC} + N_{HC}}{2}} \quad (14)$$

where $\overline{M}_n$ values calculated with Equation (14) are listed in Table 2.

3.3. Molar mass determination by size exclusion chromatography

In addition to ^{1}H-NMR, $\overline{M}_n$ was also measured by SEC with HFIP as the eluent and calibration with PMMA standards. It is necessary to note that polyester samples were not purified after synthesis. In order to get an idea of the influence of the small chains fraction, the molar mass was then calculated

Table 2. End-group concentrations and cycles fraction of PBS. $\overline{M}_n$ data of PBS determined using two methods, SEC and NMR (by taking cyclic oligomers into account or not)

PBS	N_{CC}/N_{HC}[a] [μ_{eq}·g^{-1}]	w_{cycles}[b] [wt%]	$\overline{M}_n$ of cycles[c] [g·mol^{-1}]	[η] [dL·g^{-1}]		$\overline{M}_n$ [g·mol^{-1}]		Đ[f]	$\overline{M}_n$ with cyclic[f] [g·mol^{-1}]		Number of cycles per PBS chain[h]
				$CHCl_3$	D/P[d]	SEC[e]	^{1}H-NMR	SEC[e]	SEC[e]	^{1}H-NMR	
PBS1	812/1 060	1.9	484	0.08	0.11	1 150	1 070	2.6	1 150	1 030	0.046
PBS2	62/362	2.1	473	0.25	0.33	10 300	4 710	1.7	5 120	3 890	0.52
PBS3	27/216	0.9	442	0.50	0.67	25 000	8 260	1.8	8 300	7 080	0.51
PBS4	18/107	1.1	432	0.57	0.81	29 950	16 000	1.8	9 400	11 500	0.77
PBS5	21/48	1.4	450	0.89	1.30	48 550	28 900	1.9	11 600	15 000	1.53
PBS6	46/12	1.6	466	0.99	1.50	55 250	34 100	2.0	12 300	15 600	1.93
PBS7	43/6	2.0	459	1.07	1.62	55 550	40 400	2.0	11 300	14 400	2.46

[a]Carboxylic and hydroxyl end-groups concentrations, [b]Cycles mass fraction, [c]SEC *versus* PS standard and with THF as the eluent, [d]In 50/50 wt% dichlorobenzene/phenol, [e]SEC *versus* PMMA standards and with HFIP as the eluent, [f]Dispersity, [g]Average molar mass including the contribution of cyclic oligomers, [h]Data calculated from w_{cycles}, $M_{n\,cycles}$ and M_n SEC (see text)

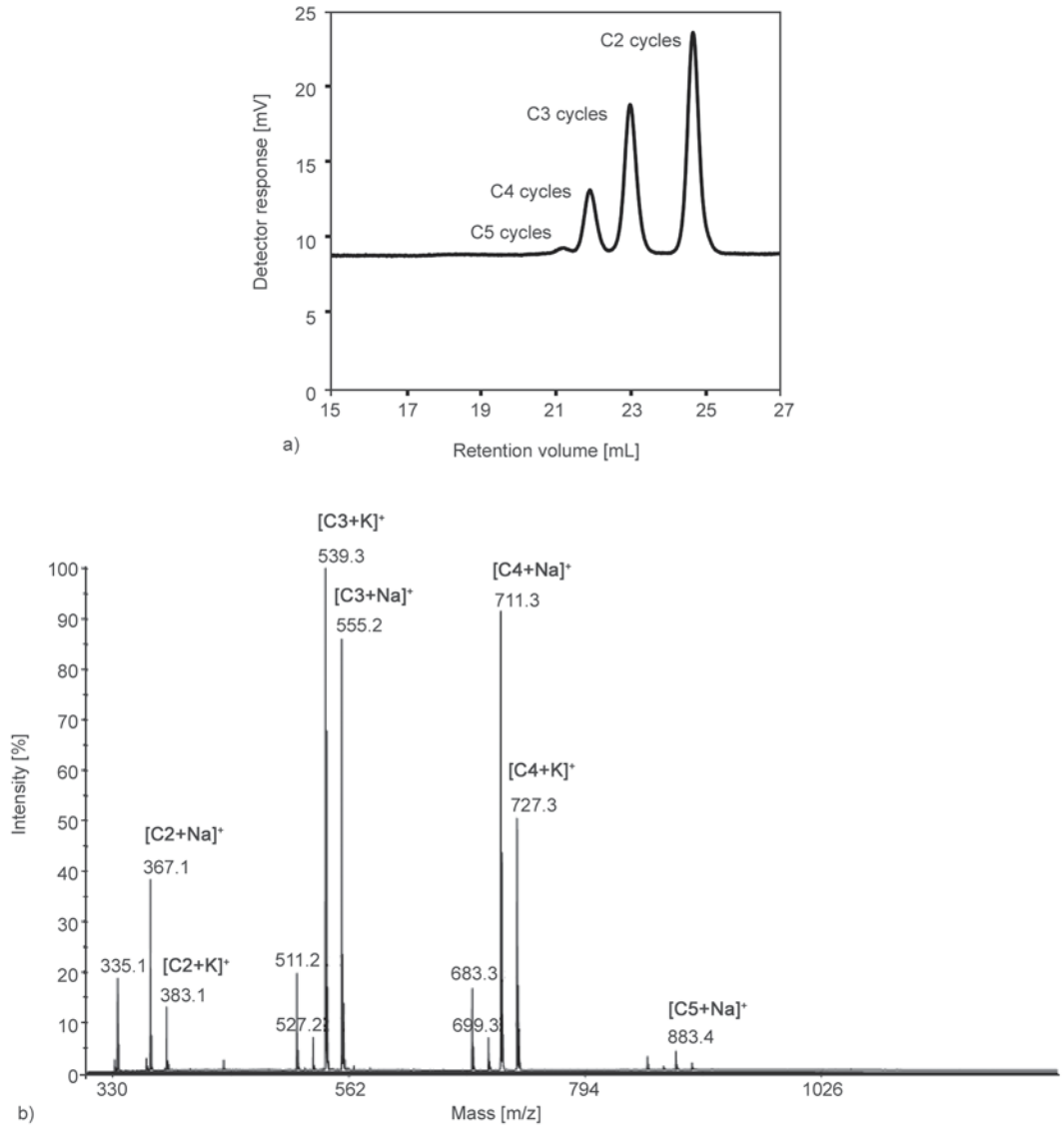

Figure 3. Analysis of the THF soluble fraction of PBS samples, (a) SEC in THF and (b) positive MALDI-TOF mass spectrum obtained in reflector mode (HABA matrix). Peaks at *m*/*z* 511.2 and 683.3 correspond to CH_2=$CHCO(C_8H_{12}O_4)_{DP}O(CH_2)_4OH$ with DP =6 and 8, respectively.

by integrating the chromatograms excluding or not the molar mass range corresponding to oligomers (100–1000 g·mol^{-1}) (Table 2).

3.4. Comparison of molar mass data obtained by ^{1}H-NMR and SEC

The number-average molar mass of PBS2 to PBS7 obtained via chain-ends quantification by ^{1}H-NMR was significantly lower than that measured by using SEC (both without correction for cyclic oligomers). This confirms the trend reported for polylactones and polylactides by several authors. Hiltunen *et al*. [20] measured molar masses 2–3 times smaller by titration than by SEC. Kowalsky *et al*. [21] and Save *et al*. [23] reported the same feature and found that the error depends on the chemical structure of the polymer and its mass range. They proposed a correction factor ranging from 0.54 to 0.58 depending on the polymer. For PBS, Lahcini *et al*. [19] found that measurements by SEC in chloroform calibrated with polystyrene standards caused an overestimation of the molar mass by 80–100% compared to universal calibration. Actually, the values determined by SEC can vary significantly depending on the detector and/or on the calibration for PBS samples. In the present study, the values determined by SEC overestimated the real $\overline{M_n}$ by at least 50%, partly due to SEC calibration using PMMA hydro-

dynamic volumes which are different from those of the PBS and partly because of baseline errors due to oligomers.

Note that the molar mass determined by ^{1}H-NMR or by SEC by taking cyclic oligomers into account was much different from that with no correction. Although the oligomers represent a small mass fraction of the polymer ($w_{cyclic} \approx 0.9$ to 2.1 wt%), the number of these cycles is high in comparison with the number of linear chains. As an example the number of moles of cycles in 1 g of PBS 5 is $n_{cycles} = w_{cycles}/M_{n\,cycles} \sim 0.003$ mole and the number of moles of long chains is $n_{chains} = (100 - w_{chains})/M_{n\,chains} \sim 0.002$ mole (w_{cycles} is the mass percentage of cycles). Thus it is roughly estimated to be 1.5 cyclic molecule per PBS linear chain for PBS with $\overline{M}_n \sim 48\,550$ g·mol^{-1} (the data for other PBS is listed in Table 2). As a consequence, the corrected $\overline{M}_n$ is much lower than the data derived without considering cyclic oligomers. Indeed, this is particularly true for samples with a high molar mass.

Finally, despite the experimental inaccuracies linked with the elution of low molar mass compounds, SEC technique and ^{1}H-NMR provided consistent $\overline{M}_n$ results when cyclic oligomers were integrated into the calculation.

3.5. Correlation between intrinsic viscosity and molar mass.

Figure 4 and Figure 5 show the plot of $\ln[\eta]$ versus $\ln\overline{M}_n$ for PBS samples in 50/50 wt% 1,2-dichlorobenzene/phenol and in chloroform respectively, where $\overline{M}_n$ values were determined by the different methods presented previously (SEC and ^{1}H-NMR), and $[\eta]$ is the average of the Huggins and Kramer dual extrapolation values. The linear relationship between $\ln[\eta]$ and $\ln\overline{M}_n$ was obtained by the least squares linear regression method. The values of equivalent a and k were obtained from the slope and intercept of the axis, respectively.

The values of equivalent k and a are presented in Table 3 as a function of the solvent used to determine the intrinsic viscosities and the method used to measure the molar mass.

Equivalent a and k values can be compared to those obtained by Imaizumi *et al*. [15] in chloroform at 40°C, $[\eta] = 2.75\cdot10^{-4}\cdot\overline{M}_n^{0.75}$. Molar masses were determined by SEC with polystyrene standards calibration. On the other hand Liu *et al*. [16] proposed $[\eta] = 1.706\cdot10^{-4}\cdot\overline{M}_n^{0.79}$. They determined the MHS

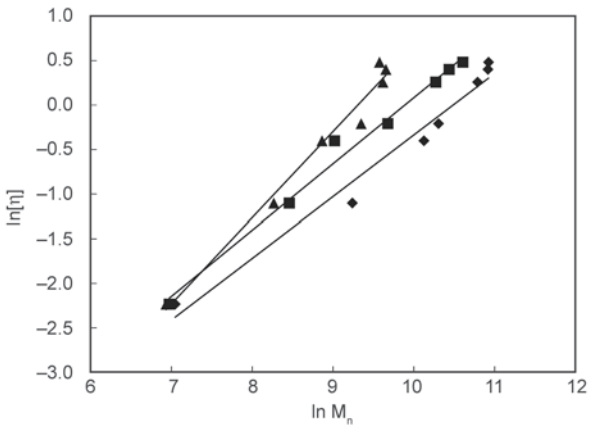

Figure 4. Relation between $\ln[\eta]$ and $\ln\overline{M}_n$ for PBS samples in 50/50 wt% 1,2-dichlorobenzene/phenol at 25°C with $[\eta]$ in dL·g^{-1} and $\overline{M}_n$ in g·mol^{-1}. $\overline{M}_n$ determined (♦) by SEC in HFIP, (■) end-group analysis and (▲) end-group analysis considering cyclic oligomers.

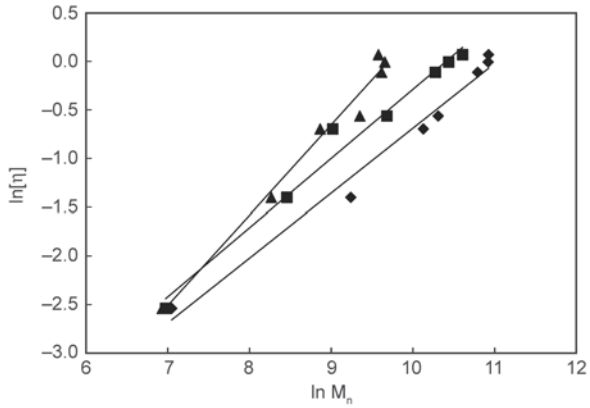

Figure 5. Relation between $\ln[\eta]$ and $\ln\overline{M}_n$ for PBS samples in chloroform at 25°C with $[\eta]$ in dL·g^{-1} and $\overline{M}_n$ in g·mol^{-1}. $\overline{M}_n$ determined (♦) by SEC in HFIP, (■) end-group analysis and (▲) end-group analysis considering cyclic oligomers.

parameters in 50/50 wt% phenol/tetrachloroethane with $\overline{M}_n$ values obtained by SEC measurements in chloroform with polystyrene calibration ($\overline{M}_n <$ 100 000 g·mol^{-1}). Recently Garin *et al.* [17] proposed $[\eta] = 39.94\cdot10^{-5}\cdot\overline{M}_n^{0.71}$ in chloroform at 30°C with molar mass determined by SEC with a triple detection system. $[\eta]$ is expressed in dL·g^{-1}.

3.6. Correlation between reduced viscosity and molar mass

The Mark-Houwink-Sakurada parameters are largely used in order to calculate molar masses from intrinsic viscosity measurements but the methodology requires the analysis of several concentrations of one polymer. In routine characterization only the reduced viscosity, η_{red}, of polyesters is measured

Table 3. Equivalent *k* and *a* parameters in chloroform and 50/50 wt% 1,2-dichlorobenzene/phenol to calculate the molar mass for different method of determination. [η] in dL·g^{-1}.

Solvent used for determining viscosity	Method for molar mass determination	Range of $\overline{M}_n$ [g/mol]	Equivalent Mark-Houwink-Sakurada relation[a)]
50/50 wt% 1,2-dichlorobenzene/phenol	SEC in HFIP[b)]	1 150–55 550	$[\eta] = 7.1 \cdot 10^{-4} \cdot \overline{M}_n^{0.69}$
	End-group analysis without considering cyclic oligomers	1 070–40 400	$[\eta] = 6.4 \cdot 10^{-4} \cdot \overline{M}_n^{0.74}$
	End-group analysis considering cyclic oligomers	1 030–15 600	$[\eta] = 1.2 \cdot 10^{-4} \cdot \overline{M}_n^{0.97}$
Chloroform	SEC in HFIP[b)]	1 150–55 550	$[\eta] = 6.4 \cdot 10^{-4} \cdot \overline{M}_n^{0.67}$
	End-group analysis without considering cyclic oligomers	1 070–40 400	$[\eta] = 6.1 \cdot 10^{-4} \cdot \overline{M}_n^{0.71}$
	End-group analysis considering cyclic oligomers	1 030–15 600	$[\eta] = 1.2 \cdot 10^{-4} \cdot \overline{M}_n^{0.93}$

[a)]*k* parameter determined with [η] in dL·g^{-1}; [b)]*versus* PMMA standards, without taking cycles into account

because obtaining this data is much less time consuming. Only one polyester solution is prepared and analyzed. In the polyester industry, it is common practice to calculate $\overline{M}_n$ with the help of simple linear empirical relationships between molar mass and reduced viscosity. As an example, very helpful equations have been proposed by Gantillon *et al.* [36] for poly(ethylene terephthalate).

In the same way, it is possible to apply this approach to PBS and plot $\overline{M}_n$ values versus η_{red}. The example depicted in Figure 6 is the most reliable one, for which we have the more data; the different relationships for obtaining $\overline{M}_n$ data are summarized in Table 4

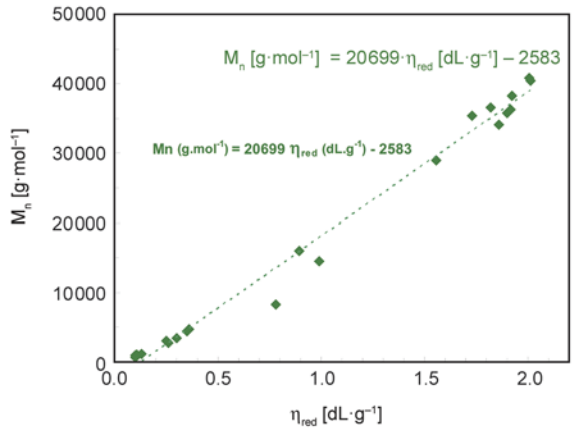

Figure 6. Number average molar mass versus reduced viscosity η_{red} measured for a 5 g·L^{-1} PBS solution in 50/50 wt% dichlorobenzene/phenol at 25°C. Molar mass determined by ^{1}H-NMR without correction for the cyclic oligomers.

4. Conclusions

The determination of the molar mass of polyesters is a difficult task. Here a series of PBS samples was synthesized with molar masses ranging from 1000 to 40 000 g·mol^{-1}. They contained a fraction of cyclic oligomers produced during the esterification step of the synthesis process. This fraction was deliberately not removed by purification in order to evaluate its effect. The characterization of the solution viscosity of these polymers was performed in chloroform, a typical solvent for PBS and in a mixture of dichlorobenzene/phenol, a classical solvent for semi-aromatic polyesters. The molar mass of the polymers was determined using different techniques. The first one was an easily available method but did not provide an absolute value of $\overline{M}_n$. More reliable data were obtained using ^{1}H-NMR spectroscopy. In addition a correction was proposed to account for the presence of PBS cyclic oligomers with a number average degree of polymerization, DPn = 4, 6, 8 and 10. The proposed sets of Mark-Houwink-Sakurada parameters and empirical relationships were

Table 4. Empirical relationship for determining $\overline{M}_n$ from reduced viscosity measurements. η_{red} in dL·g^{-1}. Concentration of the solution for the viscosity measurement = 5 g·L^{-1}.

Solvent used for determining η_{red}	Range of M_n [g·mol^{-1}]	$\overline{M}_n = f(\eta_{red})$	$\overline{M}_n$ value corresponds to that measured by:
50/50 wt% 1,2-dichlorobenzene/phenol	1 150–55 500	$\overline{M}_n = 29\,000 \cdot \eta_{red} + 700$	SEC in HFIP[a)]
	1 070–40 400	$\overline{M}_n = 20\,600 \cdot \eta_{red} - 2580$	End-group analysis without considering cyclic oligomers
	1 030–15 600	$\overline{M}_n = 7\,500 \cdot \eta_{red} + 1700$	End-group analysis considering cyclic oligomers
Chloroform	1 150–55 550	$\overline{M}_n = 47\,000 \cdot \eta_{red} - 1300$	SEC in HFIP[a)]
	1 070–40 400	$\overline{M}_n = 33\,000 \cdot \eta_{red} - 4500$	End-group analysis without considering cyclic oligomers
	1 030–15 600	$\overline{M}_n = 12\,000 \cdot \eta_{red} + 1100$	End-group analysis considering cyclic oligomers

[a)]*versus* PMMA standards, without taking cycles into account

very helpful to calculate $\overline{M}_n$ either from the determination of the intrinsic viscosity or with a simple measurement of the reduced viscosity, η_{red}.

Acknowledgements

This project was supported by the French Région Rhône-Alpes and FEFER in the framework of the Thalia project. It has also been supported by Roquettes Frères and by Texinov. We thank the NMR Polymer Center of the Institut de Chimie de Lyon (FR5223) for assistance and access to the NMR facilities.

References

[1] Lourenço A. V.: Recherches sur les composés polyatomiques. Annales de Chimie et de Physique, **67**, 257–339 (1863).

[2] Flory P. J.: Early accounters with condensation polymers. in 'Principles of polymer chemistry' (ed.: Flory P. J.) Cornell University Press, Ithaca, 12–19 (1953).

[3] Carothers W. H., Arvin G. A.: Studies on polymerization and ring formation. II. Poly-esters. Journal of the American Chemical Society, **51**, 2560–2570 (1929). DOI: 10.1021/ja01383a042

[4] Xu J., Guo B. H.: Microbial succinic acid, its polymer poly(butylene succinate), and applications. in 'Plastics from bacteria' (Ed.: Chen G. G. Q.) Springer, Berlin, 347–388 (2010).

[5] Ichikawa Y., Mizukoshi T.: Bionolle (polybutylene-succinate). in 'Synthetic biodegradable polymers' (ed.: Rieger B., Künkel A., Coates G. W., Reichardt R., Dinjus E., Zevaco T. A.) Springer, Berlin, 285–313 (2012). DOI: 10.1007/12_2011_145

[6] Papageorgiou G. Z., Achilias D. S., Bikiaris D. N.: Crystallization kinetics of biodegradable poly(butylene succinate) under isothermal and non-isothermal conditions. Macromolecular Chemistry and Physics, **208**, 1250–1264 (2007). DOI: 10.1002/macp.200700084

[7] Chung H. S., Lee J. W., Kim D. H., Jun J. N., Lee S. W.: Polyester resin and a process for preparing the same. U.S. Patent 6063895A, USA(2000).

[8] Imaizumi M., Kimura H., Fujihira R., Ichikawa Y., Suzuki J., Moteki Y., Fujimaki T., Takiyama E.: Aliphatic polyester resin and method for producing same. U.S. Patent 5714569 A, USA (1998).

[9] Aoshima T., Miki Y., Kumazawa K., Katou S., Uyeda T., Hoshino T., Shintani N., Yamagishi K., Isotani A.: Polyester derived from biomass resources and method for production thereof. U.S. Patent 20090171037 A1, USA (2009).

[10] Han Y-K., Um J. W., Im S. S., Kim B. C.: Synthesis and characterization of high molecular weight branched PBA. Journal of polymer science Part A: Polymer Chemistry, **39**, 2143–2150 (2001). DOI: 10.1002/pola.1190.abs

[11] Singley E. J., Daniel A., Person D., Beckman E. J.: Determination of Mark-Houwink parameters for poly(N-vinylformamide). Journal of Polymer Science Part A: Polymer Chemistry, **35**, 2533–2534 (1997). DOI: 10.1002/(SICI)1099-0518(19970915)35:12<2533::AID-POLA24>3.0.CO;2-7

[12] Yin N., Zeng Z-X., Xue W-L.: Intrinsic viscosity–number average molecular weight relationship for poly(1,4-butylene adipate) diol. Journal of Applied Polymer Science, **117**, 1883–1887 (2010). DOI: 10.1002/app.32058

[13] Zeng Z., Sun L., Xue W., Yin N., Zhu W.: Relationship of intrinsic viscosity to molecular weight for poly (1, 4-butylene adipate). Polymer Testing, **29**, 66–71 (2010). DOI: 10.1016/j.polymertesting.2009.09.006

[14] Kasaai M. R., Arul J., Charlet G.: Intrinsic viscosity–molecular weight relationship for chitosan. Journal of Polymer Science Part B: Polymer Physics, **38**, 2591–2598 (2000). DOI: 10.1002/1099-0488(20001001)38:19<2591::AID-POLB110>3.0.CO;2-6

[15] Imaizumi X., Okiro Y., Yoshikawa K., Koyama K.: Relationship between viscosity and molecular weight (M_W) of PBS and PBSA determined by SEC-LALLS and SEC-viscometry (in Japanese). Seikei-Kakou, **15**, 419–423 (2003).

[16] Liu X-H., Huang G-B., Wang S-P.: Synthesis of high molecule weight poly(butylene succinate) and relationship of molecule weight with intrinsic viscosity. China Plastics Industry, **36**, 14–16 (2008).

[17] Garin M., Tighzert L., Vroman I., Marinkovic S., Estrine B.: The influence of molar mass on rheological and dilute solution properties of poly(butylene succinate). Journal of Applied Polymer Science, **131**, 40887/1–40887/7 (2014). DOI: 10.1002/APP.40887

[18] Yashiro T., Kricheldorf H. R., Huijser S.: Syntheses of polyesters from succinic anhydride and various diols catalyzed by metal triflates. Macromolecular Chemistry and Physics, **210**, 1607–1616 (2009). DOI: 10.1002/macp.200900189

[19] Lahcini M., Qayouh H., Yashiro T., Simon P., Kricheldorf H. R.: Syntheses of poly(butylene succinate) by means of non-toxic catalysts. Journal of Macromolecular Science Part A: Pure and Applied Chemistry, **47**, 503–509 (2010). DOI: 10.1080/10601321003741875

[20] Hiltunen K., Härkönen M., Seppälä J. V., Väänänen T.: Synthesis and characterization of lactic acid based telechelic prepolymers. Macromolecules, **29**, 8677–8682 (1996). DOI: 10.1021/ma960402k

[21] Kowalski A., Duda A., Penczek S.: Polymerization of L,L-lactide initiated by aluminum isopropoxide trimer or tetramer. Macromolecules, **31**, 2114–2122 (1998). DOI: 10.1021/ma971737k

[22] Kricheldorf H. R., Eggerstedt S.: Macrocycles 2. Living macrocyclic polymerization of ε-caprolactone with 2,2-dibutyl-2-stanna-1,3-dioxepane as initiator. Macromolecular Chemistry and Physics, **199**, 283–290 (1998). DOI: 10.1002/(SICI)1521-3935(19980201)199:2<283::AID-MACP283>3.3.CO;2-0

[23] Save M., Schappacher M., Soum A.: Controlled ring-opening polymerization of lactones and lactides initiated by lanthanum isopropoxide, 1. General aspects and kinetics. Macromolecular Chemistry and Physics, **203**, 889–899 (2002). DOI: 10.1002/1521-3935(20020401)203:5/6<889::AID-MACP889>3.0.CO;2-O

[24] Pasch H., Rode K.: Use of matrix-assisted laser desorption/ionization mass spectrometry for molar mass-sensitive detection in liquid chromatography of polymers. Journal of Chromatography A, **699**, 21–29 (1995). DOI: 10.1016/0021-9673(95)00061-Q

[25] Montaudo M. S.: MALDI for the estimation of viscosity parameters. A modified method which applies also to polycondensates. Polymer, **45**, 6291–6298 (2004). DOI: 10.1016/j.polymer.2004.07.011

[26] Jacquel N., Freyermouth F., Fenouillot F., Rousseau A., Pascault J. P., Fuertes P., Saint-Loup R.: Synthesis and properties of poly(butylene succinate): Efficiency of different transesterification catalysts. Journal of Polymer Science Part A: Polymer Chemistry, **49**, 5301–5312 (2011). DOI: 10.1002/pola.25009

[27] Yuan Y., Johnson F., Cabasso I.: Polybenzimidazole (PBI) molecular weight and Mark-Houwink equation. Journal of Applied Polymer Science, **112**, 3436–3441 (2009). DOI: 10.1002/app.29817

[28] Solomon O. F., Ciută I. Z. : Détermination de la viscosité intrinsèque de solutions de polymères par une simple détermination de la viscosité. Journal of Applied Polymer Science, **24**, 683–686 (1962). DOI: 10.1002/app.1962.070062414

[29] Kuwahara N. J.: On the polymer–solvent interaction in polymer solutions. Journal of Polymer Science Part A: General Papers, **1**, 2395–2406 (1963). DOI: 10.1002/pol.1963.100010717

[30] Rao M. V. R. M., Yaseen M.: Determination of intrinsic viscosity by single specific viscosity measurement. Journal of Applied Polymer Science, **31**, 2501–2508 (1986). DOI: 10.1002/app.1986.070310811

[31] Chee K. K.: A critical evaluation of the single-point determination of intrinsic viscosity. Journal of Applied Polymer Science, **34**, 891–899 (1987). DOI: 10.1002/app.1987.070340301

[32] Chuah H. H., Lin-Vien D., Soni U.: Poly(trimethylene terephthalate) molecular weight and Mark–Houwink equation. Polymer, **42**, 7137–7139 (2001). DOI: 10.1016/S0032-3861(01)00043-X

[33] Zhao J. B., Li K. Y., Yang W. T.: Chain extension of polybutylene adipate and polybutylene succinate with adipoyl- and terephthaloyl-biscaprolactamate. Journal of Applied Polymer Science, **106**, 590–598 (2007). DOI: 10.1002/app.26635

[34] Chrissafis K., Paraskevopoulos K. M., Bikiaris D. N.: Thermal degradation mechanism of poly(ethylene succinate) and poly(butylene succinate): Comparative study. Thermochimica Acta, **435**, 142–150 (2005). DOI: 10.1016/j.tca.2005.05.011

[35] Bikiaris D. N., Achilias D. S.: Synthesis of poly(alkylene succinate) biodegradable polyesters, Part II: Mathematical modelling of the polycondensation reaction. Polymer, **49**, 3677–3685 (2008). DOI: 10.1016/j.polymer.2008.06.026

[36] Gantillon B., Spitz R., McKenna T. F.: The solid state postcondensation of PET, 2. Toward the development of a new dispersed phase solid state process. Macromolecular Materials and Engineering, **289**, 106–112 (2004). DOI: 10.1002/mame.200300290

eXPRESS Polymer Letters Vol.9, No.5 (2015) 435–455
Available online at www.expresspolymlett.com
DOI: 10.3144/expresspolymlett.2015.42

Properties and medical applications of polylactic acid: A review

K. Hamad[1], *M. Kaseem*[1], *H.W. Yang*[1], *F. Deri*[2], *Y. G. Ko*[1*]

[1]Plasticity Control & Mechanical Modeling Laboratory, School of Materials Science & Engineering, Yeungnam University, Gyeongsan 712–749, South Korea
[2]Laboratory of Materials Rheology, Department of Chemistry, University of Damascus, Damascus, Syria

Received 30 September 2014; accepted in revised form 30 November 2014

Abstract. Polylactic acid (PLA), one of the well-known biodegradable polyesters, has been studied extensively for tissue engineering and drug delivery systems, and it was also used widely in human medicine. A new method to synthesize PLA (ring-opening polymerization), which allowed the economical production of a high molecular weight PLA polymer, broadened its applications, and this processing would be a potential substitute for petroleum-based products. This review described the principles of the polymerization reactions of PLA and, then, outlined the various materials properties affecting the performance of PLA polymer, such as rheological, mechanical, thermal, and barrier properties as well as the processing technologies which were used to fabricate products based on PLA. In addition, the biodegradation processes of products which were shaped from PLA were discussed and reviewed. The potential applications of PLA in the medical fields, such as tissue engineering, wound management, drugs delivery, and orthopedic devices, were also highlighted.

Keywords: *biodegradable polymers, polylactic acid, properties, medical applications*

1. Introduction

In recent years, considerable research effort has been devoted to the use of polymeric biodegradable materials in plastics applications, such as packaging, to reduce the environmental impact related to the accumulation of plastics waste from the day-to-day applications of plastic materials based on traditional polymers, such as polyethylene terephthalate (PET), polyethylene (PE), etc. [1, 2]. One of the promising polymers used in these applications was the polylactic acid (PLA), which was an aliphatic polyester derived from lactic acid (2-hydroxypropionic acid) [3].

First, PLA with a low-molecular weight was synthesized by Carothers in 1932 [4, 5]. Further work by DuPont resulted in a higher-molecular weight product patented in 1954 [6]. Accordingly, two methods were used to produce the basic block of PLA, lactic acid (LA): the chemical synthesis was based on petrochemical feedstock and carbohydrate fermentation (Figure 1). Although the former was more familiar to chemists, the fermentation of natural materials containing carbohydrates, such as rice, corn, etc., was the main method used to produce LA (>90%). Datta and Henry [7] examined the synthesis and purification technologies of LA that were found in two enantiomers, L- and D-lactic acid. The results reported in that work showed that a 50/50 optically inactive mixture of L and D could be produced via a chemical route. In contrast, fermentation-derived lactic acid existed almost exclusively as L-lactic acid. The ability to produce the L-isomer in high purity possessed important ramifications in chemistry and the ultimate process/property relationships achievable in the polymers produced from lactic acid.

*Corresponding author, e-mail: younggun@ynu.ac.kr

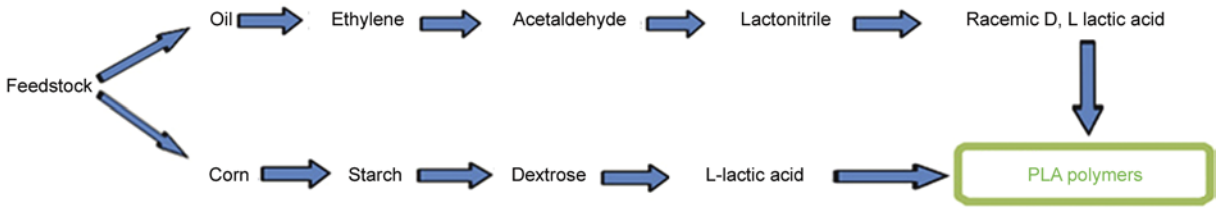

Figure 1. Lactic acid preparation methods

Biodegradable polymers attracted considerable attention in medical applications because they exhibited advantages over the non-biodegradable polymers, including an elimination of the need to remove implants and biocompatibility. Recently, PLA and its systems played an effective role in medical applications, where the use of PLA in these applications was not based solely on its biodegradability because it was made from renewable resources, but PLA was being used because it worked very well and provided the excellent properties at a low cost as compared to other traditional biodegradable polymers used in medical applications. A range of devices were prepared from different PLA types, including degradable sutures, drug releasing micro-particles, nano-particles, and porous scaffolds for cellular applications [8]. In addition, the excellent properties of PLA, including mechanical properties, thermal properties, barrier properties, and processability, using traditional processing technologies, such as extrusion, injection molding, compression molding, and blow molding, broadened its applications. The aim of this review paper is to discuss the properties for PLA and summarizes the medical applications of PLA.

2. Synthesis of polylactic acid

LA monomers synthesized using the last two methods as shown in Figure 1 were converted to PLA polymers using a range of polymerization processes, including polycondensation, ring opening polymerization and azeotopic dehydration condensation reaction (Figure 2).

Although polycondensation (PC) including solution polycondensation and melt polycondensation was the least expensive route, it was difficult to obtain a solvent-free high molecular weight PLA using these routes. In solution methods, commercial LA aqueous solution was distilled under reduced pressures and high temperatures, and the product of the distillation process was then mixed with the catalyst and solvent, and charged to a reactor under heating. The byproduct (water) was continually removed azeotropically, and the resulting polymer (PLA) was dissolved in the solvent and precipitated twice in excess methanol. Tin (II) chloride was the most commonly used catalyst and could be recovered at the end of the reaction. Because the polymer in this reaction was a low to intermediate molecular weight material, the coupling agents, such as isocyantes, epoxides or per-

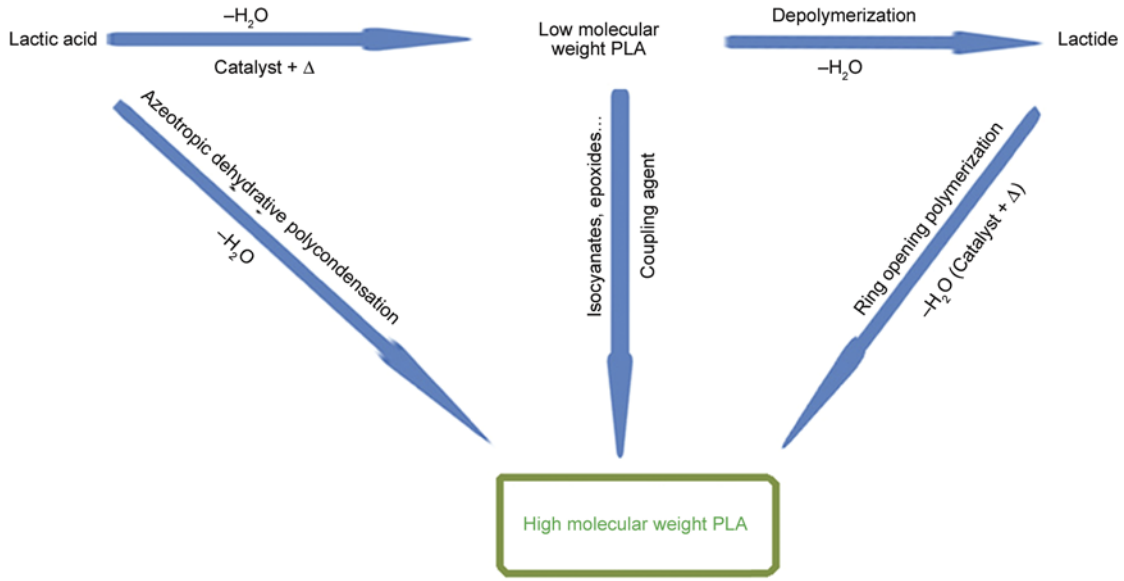

Figure 2. PLA preparation technologies

oxides, could be incorporated to produce a range of molecular weights. In contrast, the azeotropic dehydration condensation reaction of LA was a method used to yield high molecular weight PLA without the use of chain extenders or adjuvants.

In general, low molecular weights PLA polymers (no more than 30 kDa [9]) were produced using this process, and several studies reported an increase in the molecular weight of PLA polymers using the PC method. Zei *et al*. [10] used an aqueous solution of LA to prepare PLA in the presence of two catalysts (tin (II) chloride and succinic anhydride), and they reported a molecular weight in kDa region. Achmad *et al*. [11] fabricated higher molecular weights of PLA polymers where LA was polymerized by direct PC under controlled temperatures and pressures without catalyst, solvent or initiators. The effects of the reaction temperature and pressure on the resulting molecular weights were examined. The results showed that high molecular weights of 90 kDa could be obtained at 200°C after ~90 h under vacuum condition (Figure 3). In addition, the Mitsui Toatsu chemical company used organic solvents with a high boiling point to prepare poly-DL-lactic acid (PDLLA) by direct solution PC, in which the lactic acid, catalysts, and solvents were mixed in a reactor so as to produce high molecular weights of approximately 300 kDa [12].

On the other hand, ring-opening polymerization (ROP), which occurred by ring opening of the lactide (cyclic dimmer of lactic acid) in the presence of a catalyst, was the most commonly used method to obtain high molecular weight PLA [13]. This method consisted of three steps: polycondensation of LA monomers to low-molecular weight PLA, depolymerization of the PLA into the lactide, and catalytic ring-opening polymerization of the lactide intermediate resulting in PLA with a controlled molecular weight [14] (see Figure 2). On the other hand, the additional purification steps required for this process which was relatively complicated increased the cost of the polymer prepared using this method as compared to that of the polymer prepared using the PC method.

The molecular weights of the PLA polymer fabricated by the ORP method could be controlled by the residence time, temperature, consternation, and catalyst type. The ratio and sequence of D- and L-lactic acid units in the final polymer could also be controlled [15]. Recently, Cargill developed a new method to prepare the high-molecular weight PLA polymers from the lactide using a solvent free process and a novel distillation process, and a range of biodegradable PLA copolymers consisting of meso-lactide or D-lactide have become commercially available since 2003 [5].

3. Properties of polylactic acid

3.1. Rheological properties

The rheological properties of PLA and its systems (PLA blends and composites) were investigated extensively using a variety of rheological characterization methods, such as capillary and rational rheometers [16–20]. Similar to all thermoplastic polymers, PLA exhibited Newtonian behavior at the low shear rates (<10 s^{-1}) whereas it exhibited non-Newtonian behavior (shear thinning) at the high shear rates (>10 s^{-1}) as shown in Figure 4. Many studies reported the rheological behavior of PLA and showed that PLA obeyed the power law (Equation (1)) over a certain range of shear rates and tem-

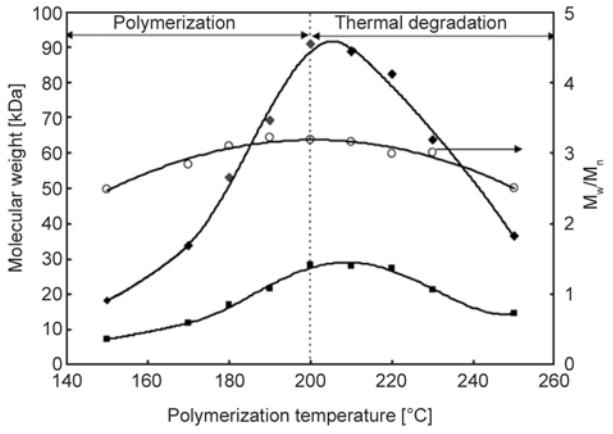

Figure 3. Effect of the PC reaction temperature on molecular weights of PLA polymers [11]

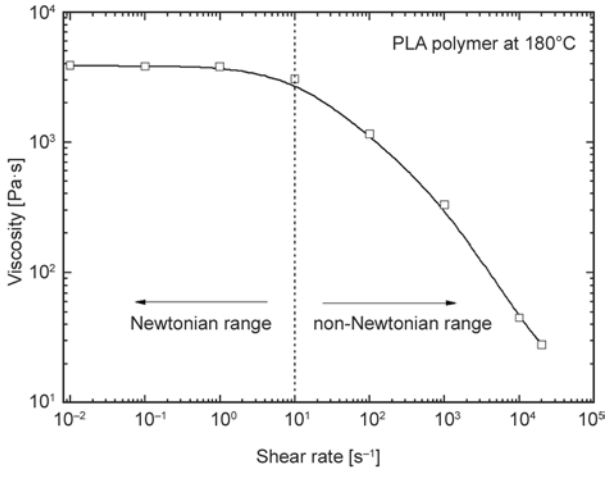

Figure 4. Viscosity curve of PLA at 180°C showing shear viscosity as a function of shear rate [26]

peratures in the same way where other polymers obeyed [21–26]:

$$\tau = K\gamma^{n} \quad (1)$$

where τ is the shear stress, γ is the shear rate, K is the consistency index, and n is the non-Newtonian index. The value of n described the deviation from Newtonian fluid flow behavior, so it was also called the flow behavior index. A higher n value indicated that the shear rate had a less effect on the flow behavior. In other words, the changes in viscosity with the shear rate were not obvious. In addition, it was found that a PLA melt obeyed Equation (2) (Arrhenius equation form) at different shear rates and shear stresses:

$$\eta = Ae^{\frac{E}{RT}} \quad (2)$$

where E is the flow activation energy, A is the consistency related to the structure and formulation and R is the gas constant. The flow activation energy reflected the temperature-sensitivity of the viscosity. Hence, a larger E indicated a higher temperature sensitivity of the materials behavior.

The effects of the composition (L- and D-isomers) on the rheological properties of the PLA polymers were reported in the end of 1990s [16]. Two types of PLA were investigated, such as amorphous PLA containing 82% L-lactide and 18% D-lactide and semi-crystalline PLA containing 95% L-lactide and 5% D-lactide. The results showed that the shear viscosity of the polymer increased with increasing L-isomer in the L/D-isomer mixture because of the increasing crystallinity of PLA, where the crystallinity increased with increasing L-isomer content [24]. In addition, Dorgan *et al*. [25] investigated the effect of the structure of PLA on the rheological properties using two different types of PLA, such as linear and branched. Their findings showed that the viscosity of branched PLA was higher than that of linear PLA in the Newtonian range, whereas viscosity of the branched PLA was lower in the non-Newtonian range. This was attributed to the shear thinning behavior of the polymer, resulting in a lower viscosity at high shear rates [26, 27].

3.2. Mechanical properties

The mechanical properties described the behavior of the material under the effect of different loading modes, such as tensile, impact, shear, and pressure. PLA had good mechanical properties (particularly tensile Young's modulus, tensile strength, flexural strength) compared to traditional polymers, such as polypropylene (PP), polystyrene (PS) and polyethylene (PE). However, the elongation at a break and the impact strength of PLA were lower than those of PP, PE, poly(ethylene terephthalate) PET, and polyamide (PA). Although the tensile strength and Young's modulus (good stiffness) of PLA were comparable to PET, the poor toughness limited its use in applications requiring plastic deformation at higher stress levels, which has motivated the considerable interest toward the toughening of PLA over last five years [28–30].

Oyama [31] reported the use of poly(ethylene-glycidyl methacrylate) (EGMA) as a toughening agent for PLA, and examined the effects of the agent content, annealing, and molecular weights of PLA (high and low molecular weights) on the impact strength. Their results are summarized in Figure 5. The impact strength of PLA could be improved by adding the agent (20%) and by annealing at 90°C for 2.5 h. Figure 5 shows that the distribution of the EGMA phase in the PLA matrix was finer in the material fabricated from the high molecular weight PLA (PLA-H) compared to that fabricated from the low molecular weight PLA (PLA-L). The higher melt viscosity of PLA-H than that of PLA-L was likely to create a higher shear force during melt-mixing. This facilitated the pull-out of the copolymers generated from the interface to the PLA matrix, leading to the generation of more co-polymers in the interfacial regions and the finer distribution of the EGMA phase. In a work reported by Sun *et al*. [32], ABS-grafted glycidyl methacrylate (ABS-g-GMA) was used as a toughening agent. They showed that the impact strength and elongation at a break of PLA could be improved by incorporating ABS-g-GM. In addition, styrene/acrylonitrile/glycidyl methacrylate copolymer (SAN-GMA) as the in situ compatibilizer and ethyltriphenyl phosphonium bromide (ETPB) as a catalyst were used to improve the toughness and compatibility of the PLA/ABS blend [33]. Hashima *et al*. [34] used a hydrogenated styrene-butadiene-styrene block copolymer (SEBS) using a reactive compatibilizer and poly(ethylene-co-glycidyl methacrylate) (EGMA) in the toughness process of the PLA/ABS blend. Recently, different compatibilizers, such as maleic anhydride-grafted ethylene propylene rub-

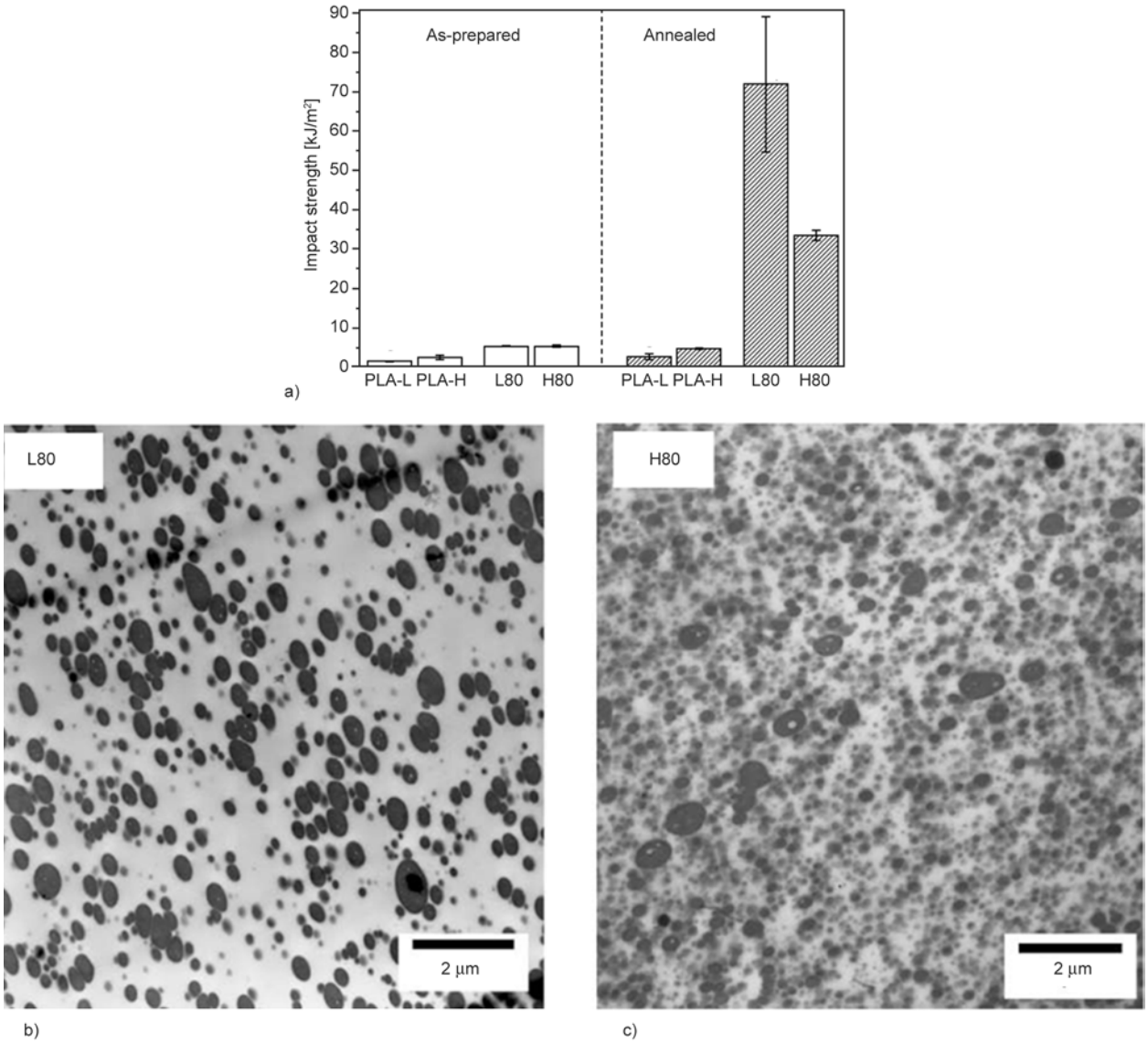

Figure 5. (a) Impact strength of PLA/EGMA blends before and after annealing treatment at 90°C for 2.5 h (b and c) morphologies of PLA/EGMA blends after annealing treatment at 90°C for 2.5 h [31]. L80 and H80 are PLA/EGMA blends (20% EGMA) prepared from low molecular weight PLA (PLA-L) and high molecular weight PLA (PLA-H), respectively

ber (EPR-g-MA), maleic anhydride-grafted styrene acrylonitrile copolymer (SAN-g-MAH), PE-epoxy, polycarbonate (PC), and glycidyl methacrylate-grafted styrene-acrylonitrile copolymer (SAN-g-GMA), were used in the blend consisting of PLA and ABS. The results showed that SAN-g-MAH was the most effective compatibilizer [35]. Wang *et al*. [36] also used PC to toughen PLA. Poly (butylene succinate-co-lactate) (PBSL) and epoxy (EP) were used as compatibilizers. The blends were prepared using a twin-screw extruder. Scanning electron microscopy (SEM) revealed a good interfacial adhesion between the blend components, which resulted in PLA materials with improved toughness and heat resistance. In addition, a ternary blend consisting of PLA, PC, and poly(butylene adipate-co-terephthalate) (PBAT) was fabricated to obtain a novel material with unique properties including high toughness and good biodegradability [37]. Recently, a bio-based vulcanized unsaturated aliphatic polyester elastomer (UPE) was used to fabricate a super-tough thermoplastic blends containing PLA [30, 38]. The results showed that the interfacial compatibilizations between PLA and UPE would lead to improved tensile and impact toughness with values up to ~99 MJ/m^3 and ~586 J/m, respectively, as compared to those of ~3.2 MJ/m^3 and ~16.8 J/m for neat PLA, respectively.

3.3. Thermal properties

PLA is a semi-crystalline or amorphous polymer with a glass transition temperature (T_g) and melting temperature (T_m) of approximately 55°C and 180°C, respectively. The thermal properties of PLA could be affected by different structural parameters, such as molecular weights and composition (stereoisomers content). The T_g was related to the molecular weight of the polymer, and the relation between T_g and molecular weight was described by Equation (3) (Flory-Fox equation):

$$T_g = T^{\infty} - \frac{K}{M} \quad (3)$$

where T^{∞} is the glass transition temperature at the infinite molecular weight, M is the molecular weight, and K is a constant related to the free volume of the end groups for the polymer chains. This relationship was reported on PLA polymers by Dorgan *et al*. [39], where the effect of molecular weights and composition (L/D ratio) on the thermal properties of PLA polymers was investigated. Figure 6 shows T_g values of several PLA polymers with different molecular weights and compositions. The curves presented in Figure 6 were fit to the data expected by Fox-Flory equation (Equation (3)) of the dependence of T_g on number-average molecular weights (M_n). The T_g increased rapidly with increasing molecular weight but, then, it reached a constant value. The effect of the L-stereoisomer content on the T_g of the polymer showed that, with increasing the amount of L-stereoisomer, the glass transition temperature at the infinite molecular weight increased as shown in Figure 6.

In addition, several studies reported the crystallization behaviors of PLA [40–43] showed that PLA could be either amorphous or semi-crystalline depending on its stereochemistry and thermal history. The crystallinity of PLA was determined commonly by differential scanning calorimetry (DSC), and by measuring the heat of fusion, ΔH_m, and the heat of crystallization, ΔH_C. The crystallinity (C [%]) can be calculated using Equation (4):

$$C\,[\%] = \frac{\Delta H_m - \Delta H_C}{93{,}1} \cdot 100 \quad (4)$$

where the constant, 93.1 J/g, is the ΔH_m for 100% crystalline PLLA or PDLA homo-polymers. The effect of stereochemistry on the crystallization behavior of PLA was investigated by Pyda *et al*. [44]. The results from DSC in Figure 7 showed that PLA polymers with ~8 and ~16% D-stereoisomer was amorphous even after 15 h of isothermally treatment at 145°C. In contrast, the heat treatment at 145°C of PLA polymers with 1.5% D-stereoisomer resulted in a large endothermic melting peak around 177°C, suggesting that PLA containing 1.5% D-stereoisomer was semi-crystalline. In addition to the stereo-chemistry of PLA polymers, the crystallization behavior could be affected by processing parameters during the production of PLA sheets, stretch blow molding of bottles, and fiber spinning. Figure 8 shows the crystallization behavior of PLA sheets with respect to draw ratio and drawing temperature [45]. As shown in Figure 8, the area below the crystallization peak increased with increasing draw ratio, indi-

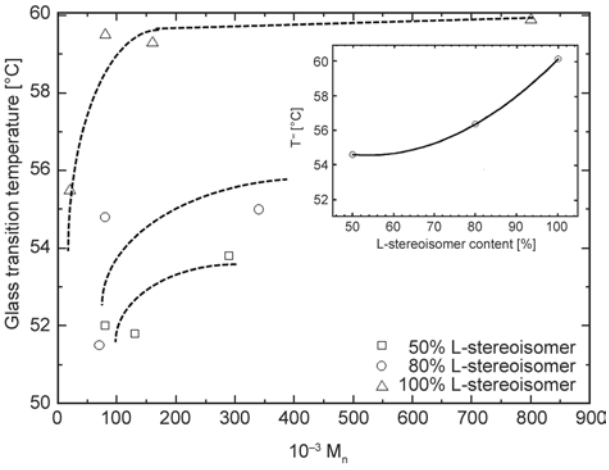

Figure 6. Glass transition temperatures (T_g) of PLA polymers with different L-stereoisomer contents as a function of number-average molecular weights (M_n) [39]

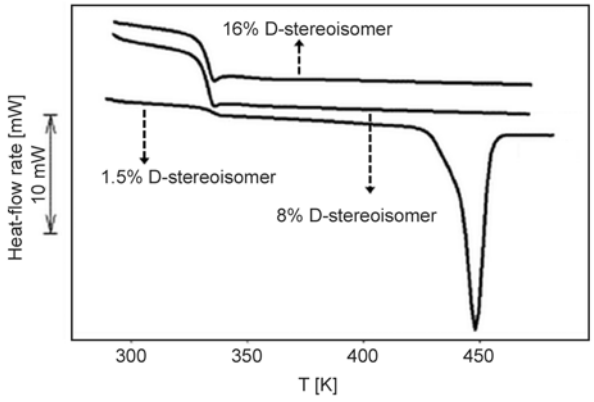

Figure 7. Differential scanning calorimetry (DSC) curves of PLA polymers with different contents of D-stereoisomer: ~1.5, ~8, and ~16 % [44]

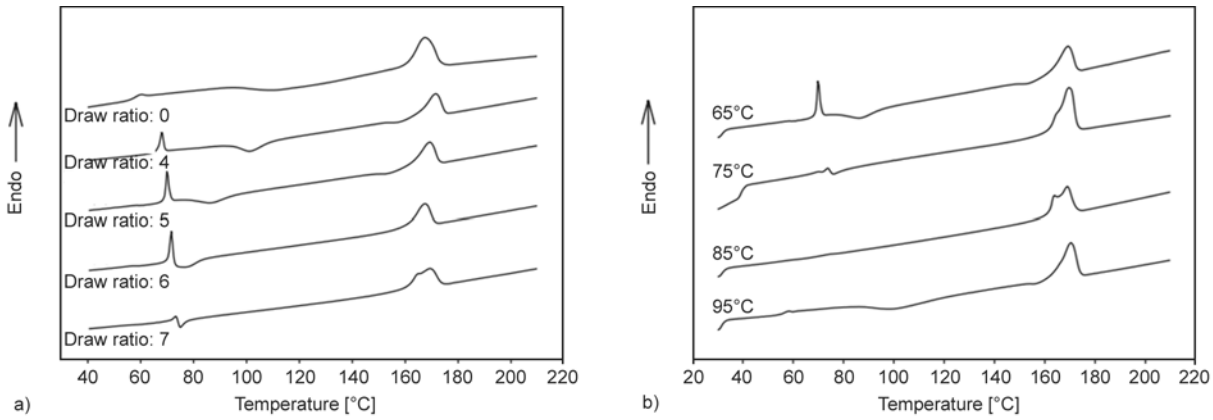

Figure 8. (a) Differential scanning calorimetry (DSC) curves of PLA samples stretched at 0.17 s^{-1} and at 65°C for various draw ratios of 0, 4, 5, 6, and 7 (b) DSC curves f PLA samples stretched at 0.17 s^{-1} with draw ratio of 5 for various drawing temperatures of 65, 75, 85, and 95°C [45]

cating the increasing of the crystallinity in PLA sheets. In addition, highly oriented PLA sheets were obtained at drawing temperature of 80°C. It was reported that at this temperature a combination of fast crystallization and slow relaxation could be achieved resulting in highly-oriented PLA sheets.

Polymer processes, such as extrusion, injection, and spinning, could result in the thermal degradation of PLA, hence the thermal stability of PLA was investigated widely. Pillin *et al*. [46] examined the effect of a thermo-mechanical treatment on the properties of PLA. The rheological and mechanical properties of PLA subjected to thermo-mechanical cycles were determined. The results showed that the viscosity of PLA decreased by a factor of 0.82 after the first cycle of treatment. In addition, only the tensile modulus remained constant with the thermo-mechanical cycles, whereas tensile strength and elongation at a break decreased after the thermo-mechanical treatment. The effect of a multi-extrusion process on the tensile properties, impact strength, melt flow index, and permeability of water vapor and oxygen of PLA was reported [47]. The results showed that the tensile strength and impact strength of PLA decreased slightly after the multi-extrusion process, whereas the melt flow index and permeability of water vapor and oxygen were increased by the multi-extrusion cycles. Al-Itry *et al*. [48] examined the thermal stability of PLA processed by the extrusion process at different processing temperatures by analyzing the rheological properties of the extruded PLA. Figure 9 shows the effect of the processing temperature on the viscosity of the extruded polymer at different temperatures along with the related molecular weights. The viscosity of the extrudate decreased with increasing extrusion temperature because of the decreasing molecular weights associated with the shear deformation imposed by the extrusion screw. To enhance the thermal stability of PLA during the extrusion process, chain extenders

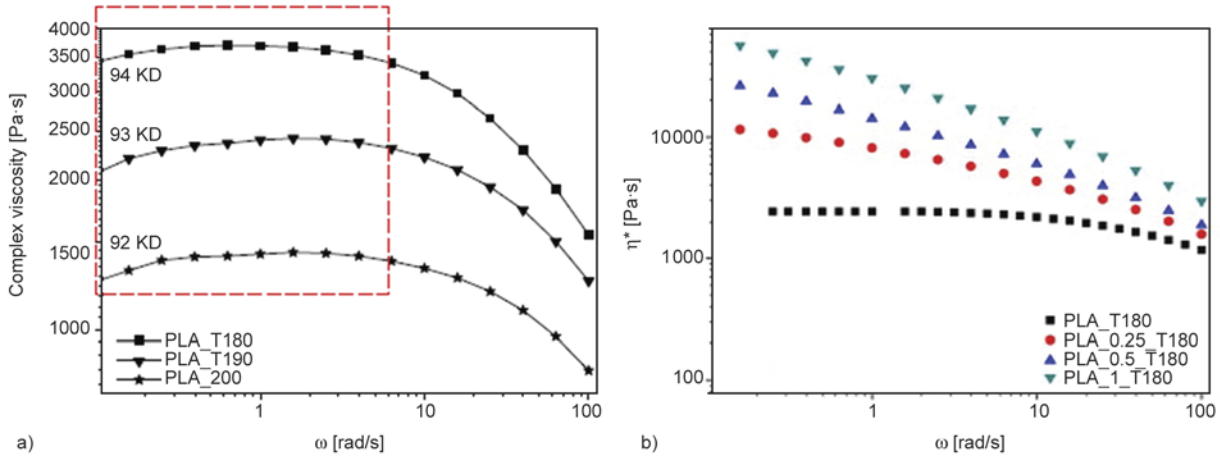

Figure 9. (a) Effect of the extrusion temperature on the complex viscosity of PLA (b) effect of chain extenders on the complex viscosity at 180°C [48]

were incorporated with the polymer, which resulted in an increased complex viscosity of the extruded polymer. Recently, the effects of PS, as a second component, on the thermal degradation of PLA polymer was studied [49]. The results showed that the presence of PS in the blend improved the thermal stability of PLA, which was attributed to the high thermal stability of PS.

3.4. Barrier properties

Because PLA was used in packaging applications [5], there has been a continuing need for a clear understanding of the barrier properties of PLA. PLA processed barrier properties that were higher than those of PE, PP and similar to PS but lower than those of PET (Figure 10). Auras and coworkers [50, 51] studied the barrier properties of PLA and compared them with those of PET and PS. They showed that the permeability coefficients of CO_2, O_2, N_2, and $H_2O_{(g)}$ for PLA were lower than that of PS, but higher than that of PET. In general, the crystallinity of PLA strongly affected the barrier properties of the polymer, where the decrease in crystallinity was a negative aspect in terms of the mechanical and barrier properties.

Accordingly, this issue motivated further interest in an improvement of the barrier properties of PLA. Many studies have reported improvement of the barrier properties of PLA. Thellen *et al*. [52] investigated montmorillonite-layered silicate/PLA composites in terms of the barrier properties. The enhancement of 50% in the oxygen barrier properties was noted. Chaiwong *et al*. [53] examined the effects of a plasma treatment on the barrier properties of PLA. The results showed that the plasma treatment had no effect on the barrier properties of PLA. In addition, Jamshidian *et al*. [54] reported the effects of a synthetic phenolic antioxidant (SPA) structure on the mechanical, thermal, and barrier properties of PLA. They found that the SPAs had no effect on the oxygen barrier properties of PLA, even though the other properties (thermal and mechanical properties) were affected. Bao *et al*. [55] examined the effects of annealing treatment on the barrier properties of films fabricated from PLA polymers. They reported that the barrierity of the films increased after annealing

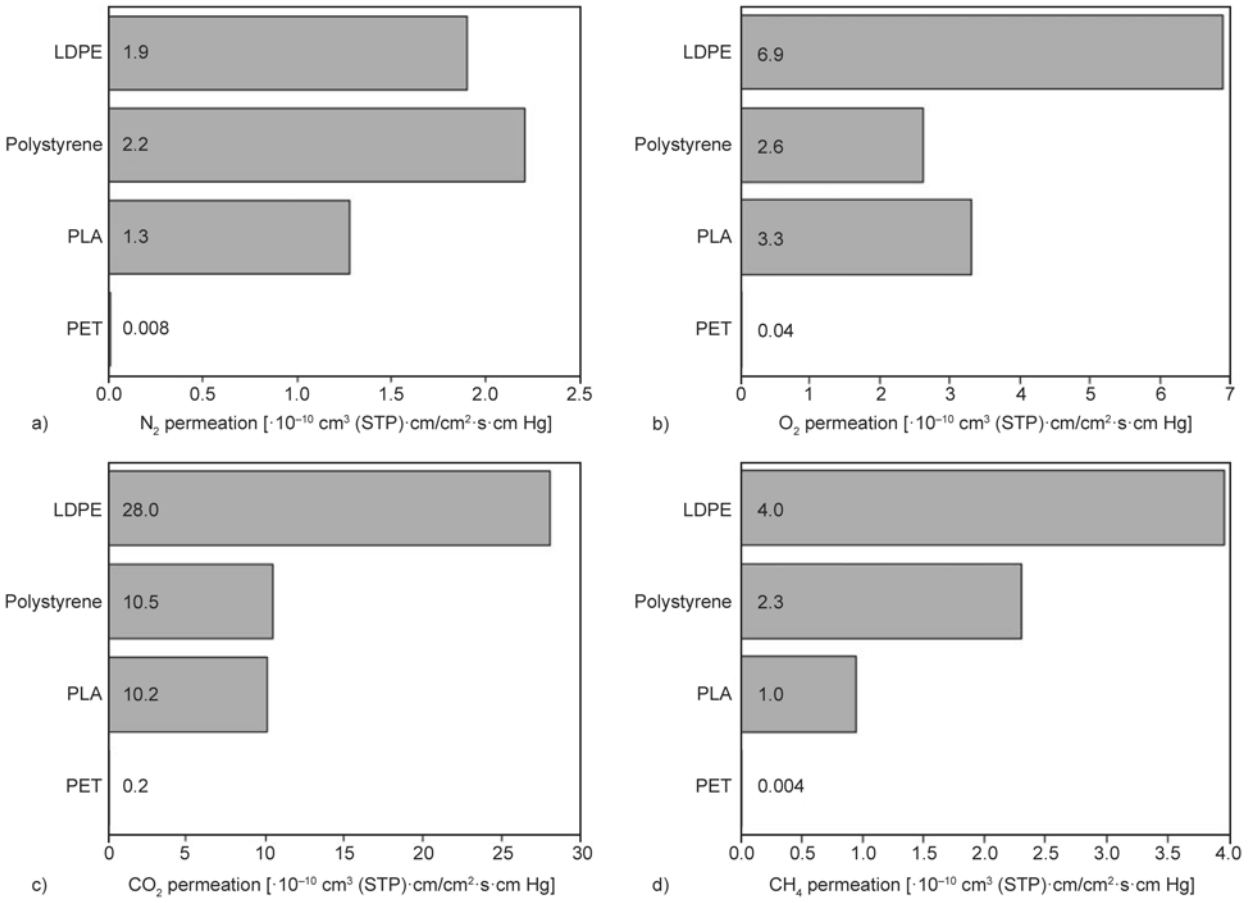

Figure 10. Barrier properties of PLA in comparison to other common polymers at 30°C (a) N_2, (b) O_2, (c) CO_2, and (d) CH_4 [25]

due to the increasing crystallinity induced by annealing.

3.5. Processing technologies

Polymer processing technologies were processes in which a polymeric material was converted to a finished product involving shaping, compounding, and chemical reactions. In the compounding process, additives, such as plasticizers, stabilizers, pigments, and fillers, were incorporated with the polymer matrix using different kinds of compounders. Accordingly, plasticizers were added to enhance the flexibility of PLA.

Al-Mulla *et al*. [56] reported the use of epoxidized palm oil as a plasticizer for PLA. PLA and plasticizer were blended using the solution method under which chloroform was used as a solvent. The ductility of PLA was improved by the addition 20% plasticizer, where the elongation of PLA increased by a factor of 8 as compared to pure PLA when the plasticizer was added. In other work [57], two commercial grades of polymeric adipates were used as plasticizers. A very good plasticization effect of these materials was reported. It was found that the elongation at break increased from 6% in the pure polymer up to approximately 500% for 20 wt% of both plasticizers. Such an increase in ductility was correlated directly with the decreases in T_g due to the compatibility between the plasticizers and PLA in the composite (Figure 11).

Polymer processing technologies, including extrusion, injection molding, and blow molding, were known for more than 100 years. In general, it was essential to dry the PLA pellets before the melt processing to reduce the moisture level, which could enhance the degradation of the ester linkage in PLA during the melting process of the polymer. Typically, the polymer was dried to less than 0.01 wt%. Amorphous pellets of PLA were dried below their T_g and because T_g depended on the stereo-chemistry of the monomers, the drying temperature depended on the composition of the polymer (PLA). Natureworks LLC, which was one of the main suppliers of PLA polymers, has recommended that PLA resins should be dried to moisture contents of 0.025 wt% or below [58]. In a single screw extrusion process, the polymer was dragged continuously along a screw through regions of high temperature and pressure. Using this process, constant profile articles, such as films, tubes, and pipes, were produced through the rotation of a screw that mixed and pushed the melts to the final articles. The general screws comprised of three main zones: the feeding zone, plasticizing (pressure) zone and metering (pumping) zone, where the temperature increased gradually from the feeding zone to the metering zone. Normally, extruders were described using several parameters, such as length/diameter ratio of the screw (*L*/*D* ratio) and compression ratio, which was the ratio of the channel depth in the feed zone to that in the metering zone. Many materials might require a specific screw, which was related to the structure and thermal stability of the fabricated materials, such as the PVC screw and PA screw. In the case of PLA, a screw with a low shear (*L*/*D* ratio between 24 and 40) was required to prevent the degradation induced by thermo-mechanical shearing during the extrusion process [58, 59].

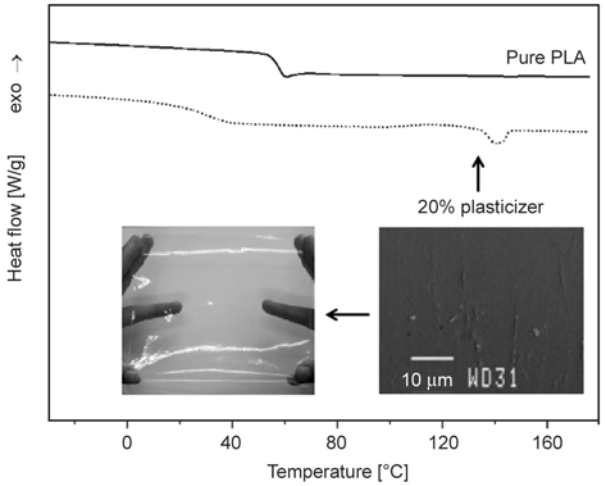

Figure 11. Transparent film of PLA/polyadipates blend and related thermal and structural properties [57]

In the injection molding, the processed material was molten using a similar screw to that used in the extrusion process, and it was then pushed (injected) using the same screw to the mold which provided the final shape of the product. The injection conditions were related to many factors, such as the chemical structure, molecular weight, morphology, and final product properties. In general, the injection temperature and pressure, which were related to the volume of an injected part through pressure-volume-temperature diagram (PVT diagram), were the most effective processing parameters in injection modeling. Sato *et al*. [60] reported the PVT diagram of PLA and other biodegradable polymers, and they used these diagrams to predict the shrinkage behavior of the final products fabricated from biodegradable polymers by injection molding. In addition, PLA bot-

tles used in food applications were molded by a blow molding process. In the first step of this process, the parison (pre-form part) was shaped using the injection molding process. The parison was then moved to blow the molding machine where it was stretched and blown after heating to temperatures between 85–110°C which was generally higher than the T_g and lower than T_m of the polymer in the axial direction, resulting in a biaxial orientation of the polymer, which in turn led to high mechanical and barrier performance of the shaped bottles.

3.6. Biodegradation properties

Biodegradation had a range of definitions but most definitions were based on the same concept: the action of microorganisms on the material and its conversion into carbon dioxide or methane and water. In addition, according to the Japanese Biodegradable Polymer Society (JBPS), the biodegradation was a process in which the polymer was decomposed to water and carbon dioxide through the action of microorganisms commonly existing in the natural environment, and the JBPS called this type of polymer (biodegradable polymers) Green Plastic. Two types of biodegradation were known, and the biodegradation products were aerobic or anaerobic. No residue mean complete biodegradation and complete mineralization was established when the original substrate was converted completely to the gaseous products. The rate of degradation was affected by a range of factors, such as the medium of biodegradation including temperature and humidity, and the chemical parameters of PLA including molecular weights and composition.

Many methods were used to measure the biodegradation rate. Some of them depended on measuring the gaseous products (CO_2 or CH_4) as a function of time. In addition, the structural, thermal, and morphological properties of the sample were monitored during the biodegradation test. Unlike weight loss, which reflected the structural changes in the polymer, CO_2 and CH_4 measurements provided an indicator of the ultimate biodegradability (i.e. mineralization) of the polymer. In these two cases, real or simulated (controlled) composting conditions were used (outdoor or indoor, respectively).

PLA degradation was studied in animal and human bodies for medical applications like implants, surgical sutures, and drug delivery materials. In these environments, PLA is initially degraded by hydrolysis and the soluble oligomers formed are metabolized by cells. On the other hand, PLA degradation upon disposal in the environment is more challenging because PLA is largely resistant to attack by microorganisms in soil or sewage under ambient conditions. The polymer must first be hydrolyzed at elevated temperatures (about 58°C) to reduce the molecular weight before biodegradation can commence. The hydrolysis reaction followed first order kinetics, as demonstrated previously and fitted to the Equation (5) [61, 62]:

$$M_W = ae^{bt} \tag{5}$$

where a and b are constants and equal to 230 kDa and 0.18 s^{-1}, respectively, and t is the time in days. Recently, the biodegradation behavior of PLA films buried in real soil environments for several months was investigated by measuring thermal and morphological properties of the residual degraded samples [63]. The analyses showed that the PLA sample surface had many corrosive holes after four months degradation, clearly showing that the PLA was degraded (Figure 12). Kale and coworkers [64, 65] reported the biodegradation performance PLA bottles in real composting conditions (~58°C and ~60% relative humidity (*RH*)) by measuring the variations in the molecular weight of the degraded polymer with the time. The results showed that the molecular weight increased slightly on the first day, which was attributed to cross-linking or recombination reactions. Major fragmentation which produced decomposition of the polymer chain to shorter oligomer chains and monomers was observed from the fourth day onwards. Figure 13 shows the variation in the molecular weight and polydispersity index (PDI) of the PLA bottles as a function of the degradation time. Molecular weight values below 5 kDa could be obtained after 57 days of the degradation, which was in consistent with the values calculated from Equation (5).

However, the biodegradability rate of PLA polymers in soil under real conditions was lower than the rate of waste accumulation. Therefore, several works reported the mixing of PLA with natural materials such as starch and cellulose in order to improve its biodegradability. For instance, in a work reported by Ohkita and Lee [66], PLA/corn starch (CS) composites were investigated in applications where fast biodegradable was required. The results of biodegrada-

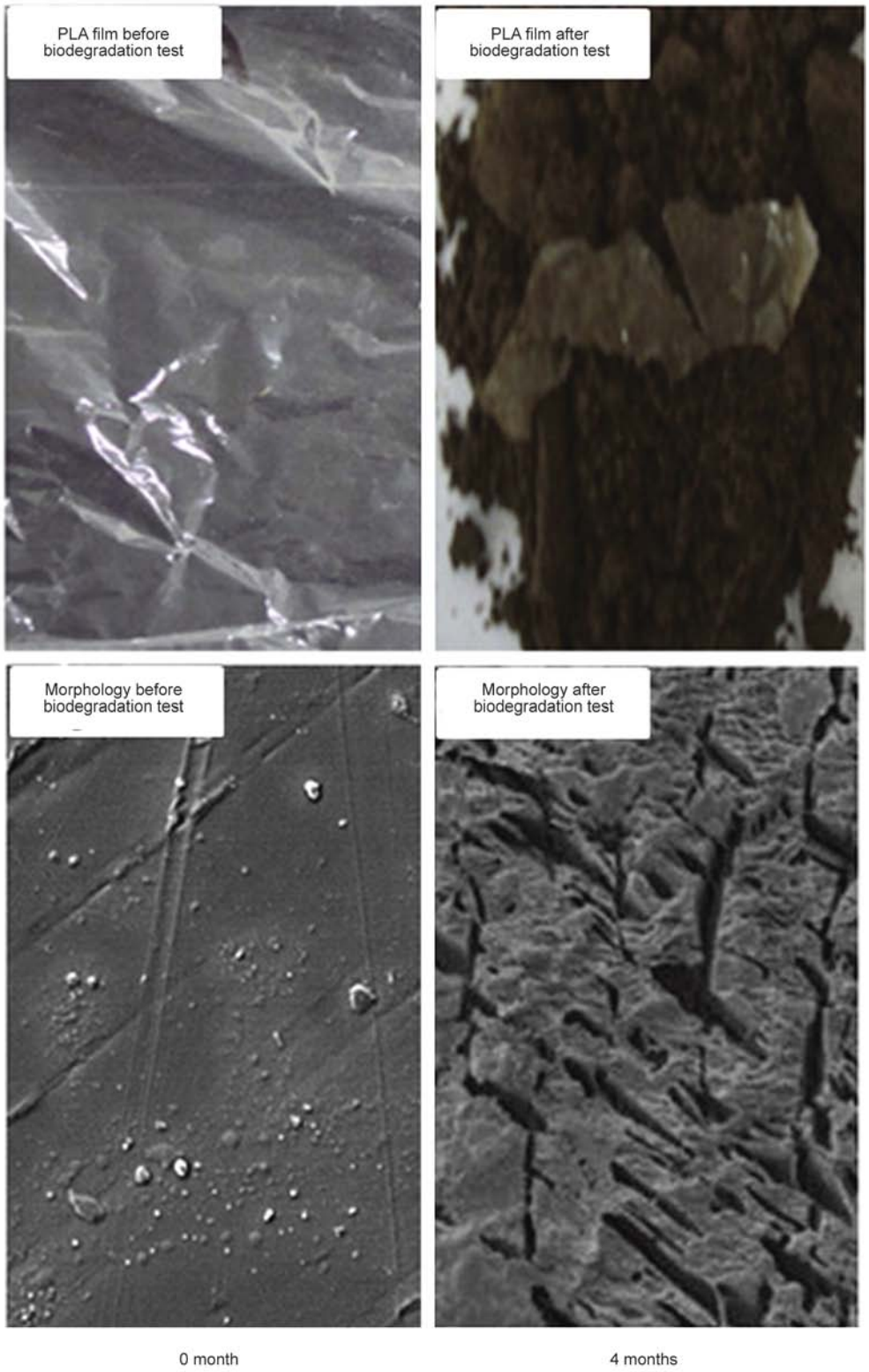

Figure 12. PLA film samples and SEM images before the biodegradation test and after 4 months of the biodegradation test [63]

tion tests of the composites performed in soil under real composting conditions (~30°C and ~80% *RH*) are presented in Figure 14. It is clearly seen from Figure 14 that the biodegradation rate increased with increasing corn starch content in the prepared composites due to the high biodegradability of starch materials.

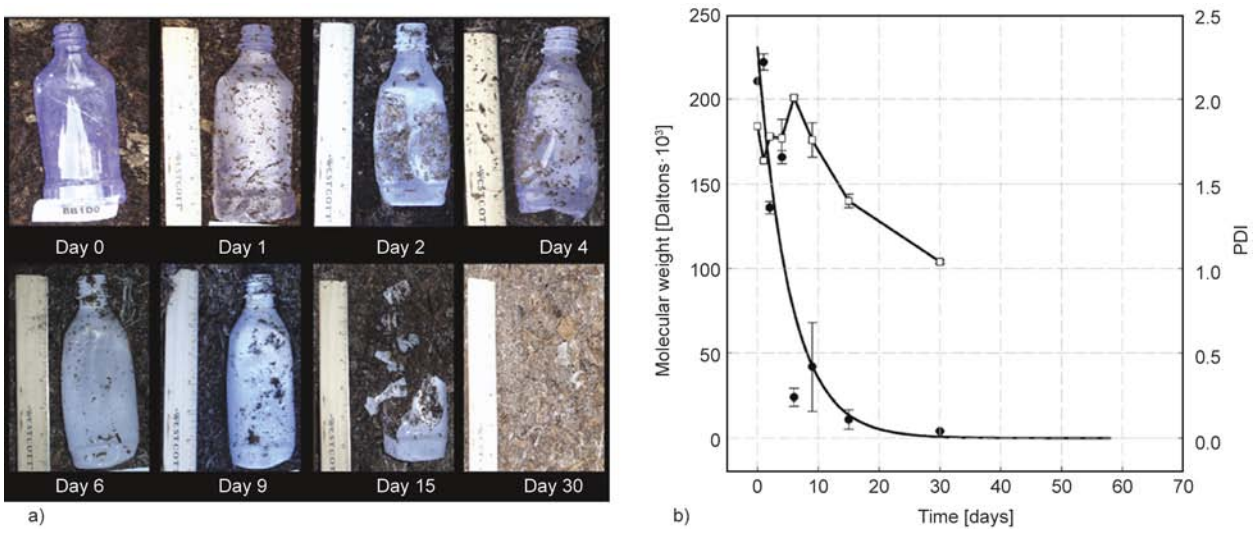

Figure 13. (a) Biodegradation of PLA bottles [64] (b) variation in the molecular weight and PDI as a function of the biodegradation time under real composting conditions [65]

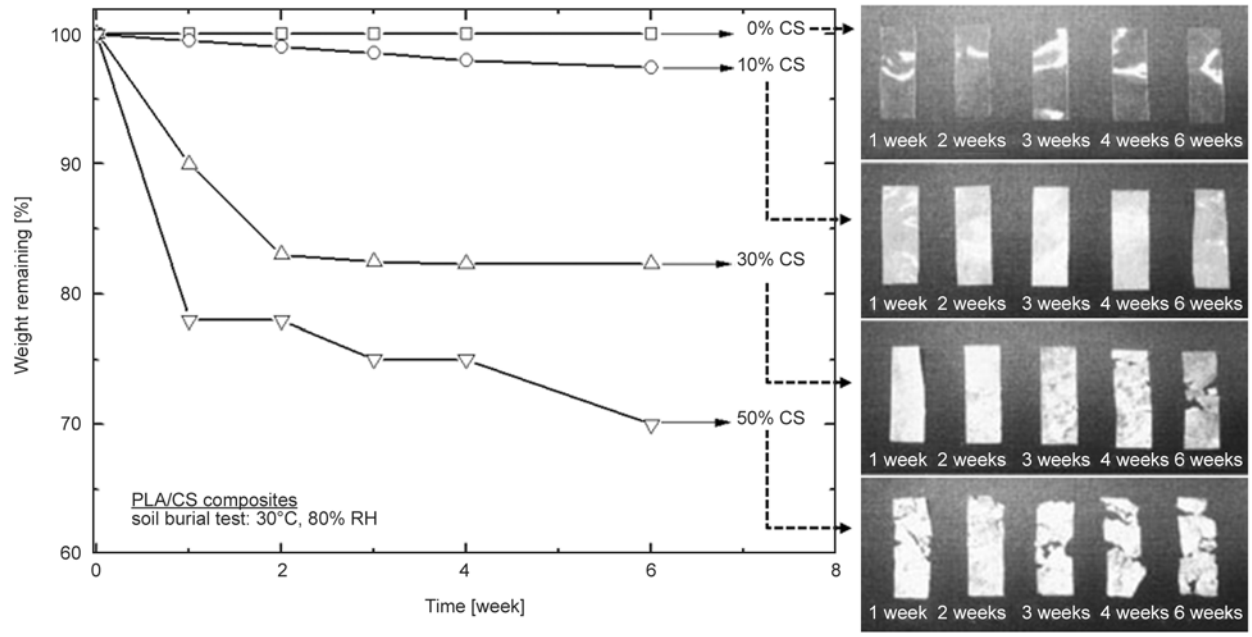

Figure 14. Weight remaining and appearance for samples fabricated from PLA and PLA/corn starch (CS) composites as a function of degradation time in burial tests at 30°C with 30% *RH*

4. Medical applications

4.1. Tissue engineering

Tissue engineering (TE), a term first coined in 1987 [67], has been a multidisciplinary field in an effort to find a solution for critical medical problems, such as tissue loss and organ failure using the development and application of knowledge in chemistry, physics, engineering, and life sciences [68]. PLA and their copolymers were a family of linear aliphatic polyesters that were used most frequently in tissue engineering. The medical applications of PLA arose from its biocompatibility as well as its dissolvability in the body by the simple hydrolysis of the ester backbone to produce non-harmful and non-toxic degradation compounds. For medical applications of PLA polymer, hydrolysis would be the most important degradation mode which differed from the biodegradation mode explained in the preceding section.

PLA has been investigated for tissue engineering applications, such as bone scaffolds, because of the good biocompatibility of this polymer [69], but it had poor mechanical properties for applications to tissue engineering. The mechanical properties of PLA

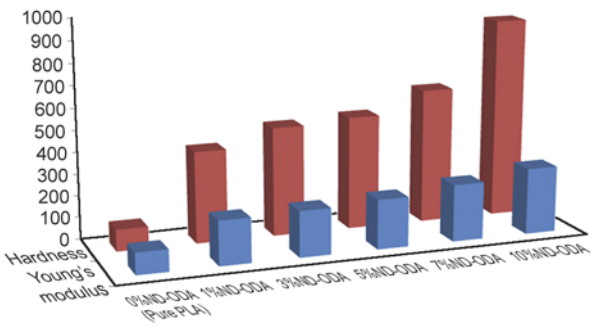

Figure 15. Hardness and Young's modulus of PLA/ND-ODA polymer composites as compared to pure PLA [70]

were improved using a range of methods, such as blending, composites forming, and co-polymerization.

Zhang *et al*. [70] prepared PLA/octadecylamine-functionalized nano-diamond (ND-ODA) composites for use in tissue engineering. The composites were prepared using a solution method where PLA was dissolved in chloroform whereas ND-ODA was dispersed in chloroform and sonicated. The PLA solution and ND-ODA dispersion were then mixed, and the chloroform was vaporized to obtain thin films of the composites. Various loads of ND-ODA in the composite preparations (up to 10 wt%) were incorporated. The results showed that the mechanical properties of PLA (Young's modulus and hardness) were improved after mixing with ND-ODA (Figure 15) because of the good affinity between the polymer and the filler in the composites indicating the applicability of this composite for tissue engineering. In addition, the toxicity and biocompatibility experiments showed that the ND-ODA and composites were nontoxic to murine osteoblasts.

In addition, PLA and its copolymers, such as PLA-polyethylene glycol block copolymer (PLA-PEG) and PLA-p-dioxanone-polyethylene glycol block copolymer (PLA-p-DPEG), were used as carriers for bone morphogenetic proteins (BMPs). BMPs were biologically active molecules capable of inducing new bone formation, and they were expected to be used clinically in combination with biomaterials, such as bone-graft substitutes to promote bone repair. Saito and Takaoka [71] examined the usefulness of PLA as a carrier of BMP and the effect of PLA on the osteoinduction of demineralized bone, and they found that PLA was a good candidate as a carrier for BMP. Low molecular weight PLA was mixed with BMP to form a composite that was then implanted in the host bone, and new bone cells were formed during the degradation of a PLA matrix in the composite as shown in Figure 16 [72]. On the other hand, the newly-formed bone was too small in quantity. Therefore, PLA copolymers were used to solve these problems with low molecular weight PLA. Chang *et al*. [73] prepared a novel porous PLA composite scaffold and evaluated the capacity of the scaffold as a carrier for the recombinant bone morphogenetic protein 2 (rhBMP2). The results showed that the PLA scaffolds exhibited a sufficient capability of carrying rhBMP2 to induce bone formation in two weeks.

4.2. Wound management

PLA and its copolymers were used in a range of applications related to wound management, such as

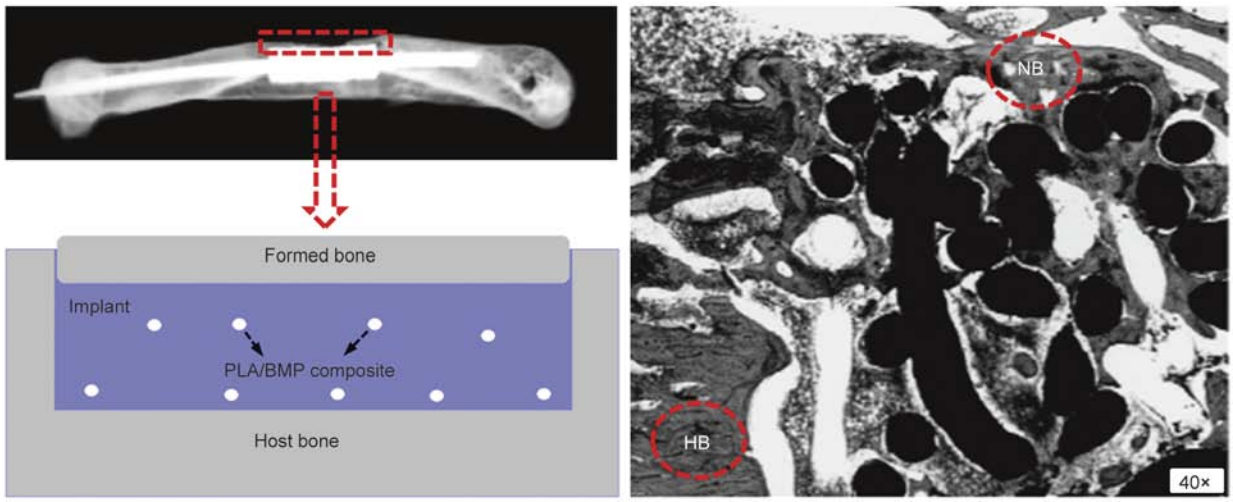

Figure 16. Bone-defect treatment using implants containing a composite of PLA and BMP. The composite exuded from pores of the implants and formed a layer of new bone (NB) covering the surface of the biomaterials. The NB encased the implant and thus enhanced biological fixation of the biomaterials to the host bone (HB) [71, 72]

surgical sutures, healing dental extraction wounds, and preventing postoperative adhesions. Li *et al*. [74] evaluated the efficacy and feasibility of PLA ureteral stents for the treatment of ureteral war injuries. The stents made of PLA were reliable in the treatment of ureteral war injuries where PLA stents were degraded so that they were removed from the body. Therefore, PLA stents represented a promising future for the treatment of ureteral war injuries. Qin *et al*. [75] used PLA based on polymer blends to prevent postoperative adhesions. In that study, PLA was blended with polytrimethylene carbonate (PTMC) using the solution method where the two polymers were mixed and dissolved in acetoacetate. After the polymeric solution was poured into a Teflon plate, the solvent was evaporated to obtain a thin film. The films prepared from the blend at different ratios were prepared and compared with those of pure PLA. Traditional characterizations of the films (thermal and mechanical characterizations) as well as the medical study on the films were performed. The results showed that the blends were more flexible than pure PLA, whereas the tensile strength, Young's modulus, and glass transition temperature of pure PLA were higher than those of the blends (Figure 17). The decreasing T_g with increasing PTMC content in the blend indicated the compatibility between the two components (PLA, PTMC) [76, 77]. The greater flexibility of the blends compared to pure PLA made them more suitable for covering the wound where the stiff film of pure PLA could not be covered freely over the wound when it was implanted in the body. The cytotoxicity of the blend films was examined by measuring the amount of succinate dehydrogenase (SDH) released by the cells incubated with the blend films. The results suggested that PLA and PLA/PTMC blend films were not cytotoxic. Brekke *et al*. [78] used PLA to improve the ability of dental extraction wound healing, and they reported that a PLA surgical dressing material reduced the incidence of mandibular third molar extraction wound failure substantially in all phases of the study.

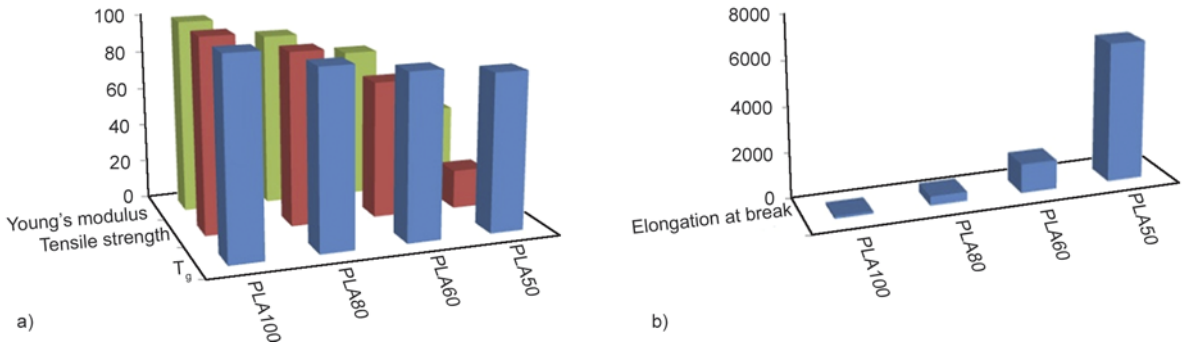

Figure 17. Mechanical and thermal properties of PLA/PTMC blends as a function of PLA content in the blends [75] (a) T_g, tensile strength and Young's modulus, (b) elongation at break

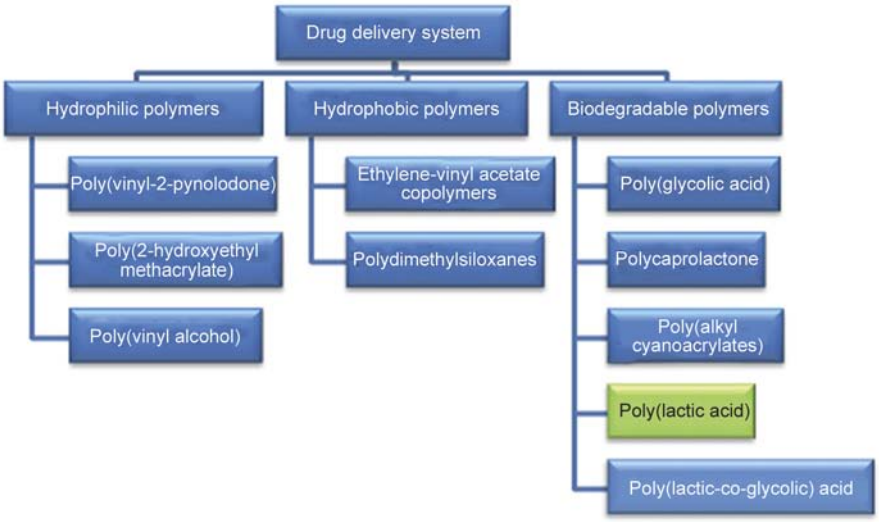

Figure 18. Different types of polymer used in the drug delivery system applications

4.3. Drug delivery system

In drug delivery systems (DDS), the drug could be released continuously for different periods of time up to one year. Different types of polymers including biodegradable polymers were used in this application (Figure 18).

Biodegradable polymers (PLA, PCL, Gelatin, etc.) were used as drug delivery systems owing to their biocompatibility, biodegradability, better encapsulation, and lower toxicity. Polymeric drug release occurred in one of three ways: erosion, diffusion and swelling. In the case of biodegradable polyesters consisting of monomers which were connected to each other by ester bonds, the degradation begun after the penetration of water into the device. The breakage of ester bonds occurred randomly through hydrolytic ester cleavage, leading to subsequent erosion of the device. For degradable polymers, two different erosion mechanisms were proposed: homogeneous or bulk erosion and heterogeneous or surface erosion [79] (Figure 19).

PLA and their copolymers in the form of nano-particles were used in the encapsulation process of many drugs, such as psychotic [80], restenosis [81], hormones [82], oridonin [83], dermatotherapy [84], and protein (BSA) [85]. Different methods were used to obtain these nano-particles, such as solvent evaporation, solvent displacement [86], salting out [80], and emulsion solvent diffusion [87].

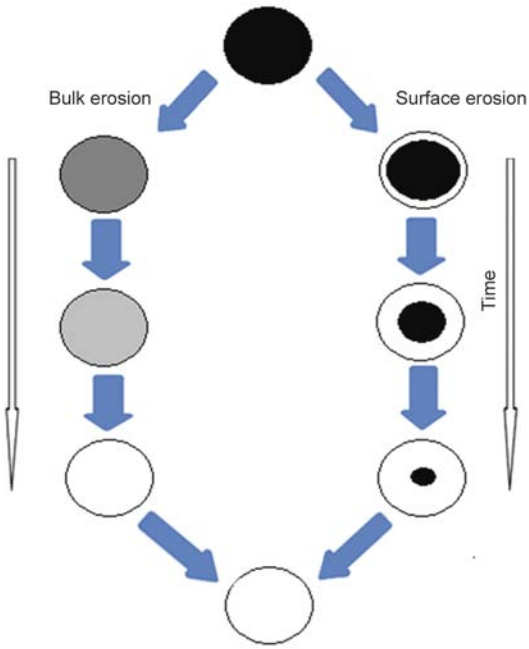

Figure 19. Different erosion mechanisms

Ling and Huang [88] used the poly(lactic-co-glycolic) acid nano-particles for loading the drug, paclitaxel. The nano-particles were prepared using the emulsion solvent evaporation method in the presence of tocopheryl polyethylene glycol succinate as an emulsion agent. The drug loading efficiency, encapsulation efficiency and ability of in vitro drug release of the nano-particles were investigated.

Rancan *et al*. [84] examined the use of PLA nanoparticles (PLA-NPs) loaded with fluorescent dyes as carriers for transepidermal drug delivery. PLA NPs were prepared using solvent evaporation technology. In this process, PLA was dissolved in acetone, the solution was added to an aqueous solution with moderate stirring and the solvent was then evaporated under reduced pressure at room temperature to obtain the PLA-NPs. The same method was used to obtain the fluorescent particles, where the fluorescent dye and PLA were dissolved in acetone. PLA NPs were tested in human skin. The results showed that PLA NPs could represent ideal candidates for the design of drug delivery systems, which could target active compounds into hair follicles.

4.4. Orthopedic device

Biodegradable polymers were used in orthopedic applications to achieve many goals. One of the most important goals was to avoid a second surgical procedure to remove unnecessary hardware (Figure 20). Traditionally, titanium was used in this application, but, in this case, a second surgical procedure was needed to remove the titanium device. Historically, the PLA polymer was used to produce biodegradable screws and fixation pins, plates, and suture anchors. These types of absorbable screws and pins have been gaining the widespread clinical use, particularly in cases where high mechanical stiffness or strength was not required. Pertinent orthopedic areas might include the knee [89–91], shoulder, foot and ankle [92–94], hand, wrist [95], elbow [96], pelvis, and zygomatic fractures. In some cases, high performance PLA was needed, so that techniques would be used to improve the mechanical properties of PLA, particularly impact strength, tensile strength, and flexural strength in fracture fixation, where both metal and biodegradable plate, pins, and rods had limits in their use in fracture fixation.

Haers *et al*. [97] reported an improvement of the mechanical properties of PLA through the control

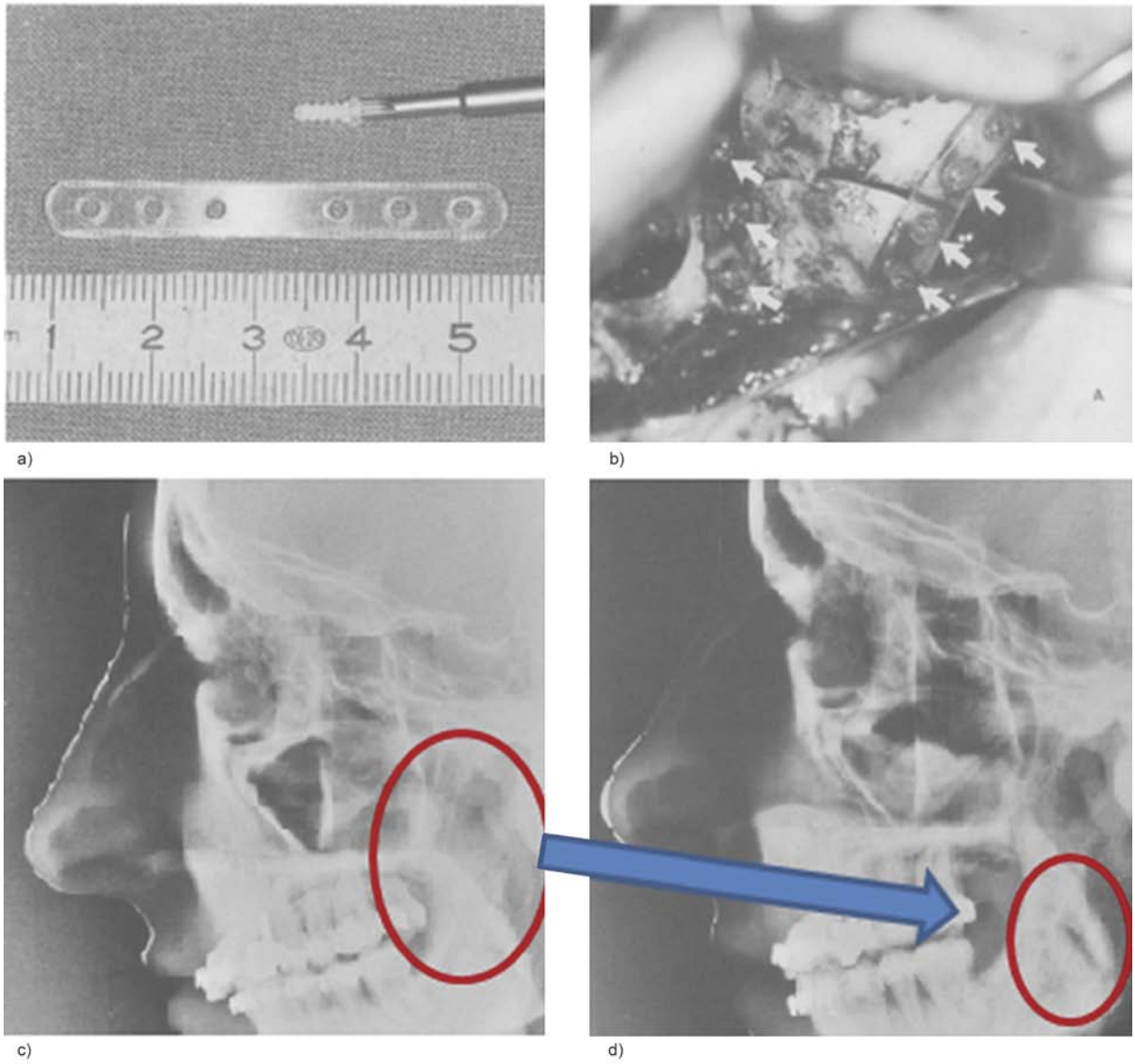

Figure 20. (a) Screws and plate made of PLA (b) upper jaw with the plates and screws in situ (c) and (d) lateral cephalogram, with the screws and plate, taken immediately postoperatively and 6 weeks postoperatively, respectively [97]

of the *L*/*D* ratio in the polymer, where the ratio of *L*/*D* 85/15 was polymerized, and the prepared PLA was used for the manufacture of screws and fixation plates used in fracture fixation. The results showed that it was possible to use the plates without the need for additional support for the fixation of fractures (Figure 20). van Sliedregt *et al*. [98] examined the biocompatibility of PLA for orthopedically applications using cell cultures of three types of rat epithelial cells in addition to human fibroblasts and osteosarcoma cells. They found that PLA showed good biocompatibility. Majola *et al*. [99] reported that PLA rods had good biocompatibility in the cancellous bone of rats. Böstman *et al*. [92] also reported the biocompatibility of PLA copolymers in the human body. They found that 6 out of 120 patients treated with pins fabricated from a PLA-PGA copolymer developed an aseptic sinus at the implantation site.

5. Conclusions

According to the brief review reported in this review paper, the polylactic acid would be one of the promising candidates for various industrial applications. The excellent biocompatibility, low cost, and good materials properties of PLA would open many applications in the medical fields, such as drug delivery systems and orthopedic devices. In addition, the shear thinning behavior of PLA would be suitable for processes using traditional polymer processing technologies, which have also broadened the applications.

More academic attention would be paid to the development of new methods to prepare polylactic acid,

which would be less expensive and more complex than those of the other polymerization methods. In addition, the development of new applications using PLA in the medical fields would be strongly required for next-generation.

Acknowledgements

This work was supported by funding from the Yeungnam University Research Project (#214A367008).

References

[1] Hamad K., Kaseem M., Ko Y. G., Deri F.: Biodegradable polymer blends and composites: An overview. Polymer Science Series A, **56**, 812–829 (2014). DOI: 10.1134/S0965545X14060054

[2] Kaseem M., Hamad K., Deri F.: Thermoplastic starch blends: A review of recent works. Polymer Science Series A, **54**, 165–176 (2012). DOI: 10.1134/S0965545X1202006X

[3] Lim L-T., Auras R., Rubino M.: Processing technologies for poly(lactic acid). Progress in Polymer Science, **33**, 820–852 (2008). DOI: 10.1016/j.progpolymsci.2008.05.004

[4] Holten H.: Lactic acid properties and chemistry of lactic acid and derivatives. Verlag Chemie, Weinheim, (1971).

[5] Lunt J.: Large-scale production, properties and commercial applications of polylactic acid polymers. Polymer Degradation and Stability, **59**, 145–152 (1998). DOI: 10.1016/S0141-3910(97)00148-1

[6] Lowe E.: Preparation of high molecular weight polyhydroxyacetic ester. U.S. Patent 2668162 A, USA (1954).

[7] Datta R., Henry M.: Lactic acid: Recent advances in products, processes and technologies – A review. Journal of Chemical Technology and Biotechnology, **81**, 1119–1129 (2006). DOI: 10.1002/jctb.1486

[8] Lasprilla A. J. R., Martinez G. A. R., Lunelli B. H., Jardini A. L., Filho R. M.: Poly-lactic acid synthesis for application in biomedical devices – A review. Biotechnology Advances, **30**, 321–382 (2012). DOI: 10.1016/j.biotechadv.2011.06.019

[9] Zhang J., Krishnamachari P., Lou J., Shahbazi A.: Synthesis of poly(L(+) lactic acid) by polycondensation method in solution. in 'Proceedings of the 2007 National Conference on Environmental Science and Technology' (eds.: Nzewi E., Reddy G., Luster-Teasley S., Kabadi V., Chang S-Y., Schimmel K., Uzochukwu G.) Springer, New York 3–8 (2009). DOI: 10.1007/978-0-387-88483-7

[10] Lei Z., Bai Y., Wang S.: Synthesis of high molecular weight polylactic acid from aqueous lactic acid *co*-catalyzed by tin(II)chloride dihydrate and succinic anhydride. Chinese Science Bulletin, **50**, 2390–2392 (2005). DOI: 10.1360/982005-1208

[11] Achmad F., Yamane K., Quan S., Kokugan T.: Synthesis of polylactic acid by direct polycondensation under vacuum without catalysts, solvents and initiators. Chemical Engineering Journal, **151**, 342–350 (2009). DOI: 10.1016/j.cej.2009.04.014

[12] Cheng Y., Deng S., Chen P., Ruan R.: Polylactic acid (PLA) synthesis and modifications: A review. Frontiers of Chemistry in China, **4**, 259–264 (2009). DOI: 10.1007/s11458-009-0092-x

[13] Auras R., Lim T., Selke M., Tsuji H.: Poly(lactic acid): Synthesis, structures, properties, processing, and applications. Wiley, New Jersey (2010).

[14] Kim E., Shin W., Yoo K., Chung S.: Characteristics of heterogeneous titanium alkoxide catalysts for ring-opening polymerization of lactide to produce polylactide. Journal of Molecular Catalysis A: Chemical, **298**, 36–39 (2009). DOI: 10.1016/j.molcata.2008.09.029

[15] Gupta B., Revagade N., Hilborn J.: Poly(lactic acid) fiber: An overview. Progress in Polymer Science, 34, 455–482 (2007). DOI: 10.1016/j.progpolymsci.2007.01.005

[16] Fang Q., Hanna M.: Rheological properties of amorphous and semicrystalline polylactic acid polymers. Industrial Crops and Products, **10**, 47–53 (1999). DOI: 10.1016/S0926-6690(99)00009-6

[17] Hamad K., Kaseem M., Deri F.: Rheological and mechanical characterization of poly(lactic acid)/polypropylene polymer blends. Journal of Polymer Research, **18**, 1799–1806 (2011). DOI: 10.1007/s10965-011-9586-6

[18] Hamad K., Kaseem M., Deri F.: Rheological and mechanical properties of poly(lactic acid)/polystyrene polymer blend. Polymer Bulletin, **65**, 509–519 (2010). DOI: 10.1007/s00289-010-0354-2

[19] Hamad K., Kaseem M., Deri F.: Poly(lactic acid)/low density polyethylene polymer blends: Preparation and characterization. Asia-Pacific Journal of Chemical Engineering, **7**, 310–316 (2012). DOI: 10.1002/apj.1649

[20] Huneault M., Li H.: Morphology and properties of compatibilized polylactide/thermoplastic starch blends. Polymer, **48**, 270–280 (2007). DOI: 10.1016/j.polymer.2006.11.023

[21] Shin B., Han D., Narayan R.: Rheological and thermal properties of the PLA modified by electron beam irradiation in the presence of functional monomer. Journal of Polymers and the Environment, **18**, 558–566 (2010). DOI: 10.1007/s10924-010-0198-8

[22] Wang Y., Yang L., Niu Y., Wang Z., Zhang J., Yu F., Zhang H.: Rheological and topological characterizations of electron beam irradiation prepared long-chain branched polylactic acid. Journal of Applied Polymer Science, **122**, 1857–1865 (2011). DOI: 10.1002/app.34276

[23] Hamad K., Ko Y. G., Kaseem M., Deri F.: Effect of acrylonitrile–butadiene–styrene on flow behavior and mechanical properties of polylactic acid/low density polyethylene blend. Asia-Pacific Journal of Chemical Engineering, **9**, 349–353 (2014).
DOI: 10.1002/apj.1802

[24] Saeidlou S., Huneault M. A., Li H., Park C. B.: Poly (lactic acid) crystallization. Progress in Polymer Science, **37**, 1657–1677 (2012).
DOI: 10.1016/j.progpolymsci.2012.07.005

[25] Dorgan J. R., Lehermeier H., Mang M.: Thermal and rheological properties of commercial-grade poly(lactic acid)s. Journal of Polymers and the Environment, **8**, 1–9 (2000).
DOI: 10.1023/A:1010185910301

[26] Lehermeier H., Dorgan J. R.: Melt rheology of poly (lactic acid): Consequences of blending chain architectures. Polymer Engineering and Science, **41**, 2172–2184 (2001).
DOI: 10.1002/pen.10912

[27] Palade R., Lehermeier H., Dorgan J. R.: Melt rheology of high L-content poly(lactic acid). Macromolecules, **34**, 1384–1390 (2001).
DOI: 10.1021/ma001173b

[28] Liu H., Zhang J.: Research progress in toughening modification of poly(lactic acid). Journal of Polymer Science Part B: Polymer Physics, **49**, 1051–1083 (2011).
DOI: 10.1002/polb.22283

[29] Rasal R., Janorkar A., Hirt D.: Poly(lactic acid) modifications. Progress in Polymer Science, **35**, 338–356 (2010).
DOI: 10.1016/j.progpolymsci.2009.12.003

[30] Liu G-C., He Y-S., Zeng J-B., Xu Y., Wang Y-Z.: *In situ* formed crosslinked polyurethane toughened polylactide. Polymer Chemistry, **5**, 2530–2539 (2014).
DOI: 10.1039/C3PY01649H

[31] Oyama H.: Super-tough poly(lactic acid) materials: Reactive blending with ethylene copolymer. Polymer, **50**, 747–751 (2009).
DOI: 10.1016/j.polymer.2008.12.025

[32] Sun S., Zhang M., Zhang H., Zhang X.: Polylactide toughening with epoxy-functionalized grafted acrylonitrile–butadiene–styrene particles. Journal of Applied Polymer Science, **122**, 2992–2999 (2011).
DOI: 10.1002/app.34111

[33] Li Y., Shimizu H.: Improvement in toughness of poly (L-lactide) (PLLA) through reactive blending with acrylonitrile–butadiene–styrene copolymer (ABS): Morphology and properties. European Polymer Journal, **45**, 738–746 (2009).
DOI: 10.1016/j.eurpolymj.2008.12.010

[34] Hashima K., Nishitsuji S., Inoue T.: Structure-properties of super-tough PLA alloy with excellent heat resistance. Polymer, **51**, 3934–3939 (2010).
DOI: 10.1016/j.polymer.2010.06.045

[35] Jo M. Y., Ryu Y. J., Ko J., Yoon J. H., Yoon J-S.: Effects of compatibilizers on the mechanical properties of ABS/PLA composites. Journal of Applied Polymer Science, **125**, E231–E238 (2012).
DOI: 10.1002/app.36732

[36] Wang Y., Chiao S., Hung T-F., Yang S-Y.: Improvement in toughness and heat resistance of poly(lactic acid)/polycarbonate blend through twin-screw blending: Influence of compatibilizer type. Journal of Applied Polymer Science, **125**, E402–E412 (2012).
DOI: 10.1002/app.36920

[37] Kanzawa T., Tokumitsu K.: Mechanical properties and morphological changes of poly(lactic acid)/polycarbonate/poly(butylene adipate-*co*-terephthalate) blend through reactive processing. Journal of Applied Polymer Science, **121**, 2908–2918 (2011).
DOI: 10.1002/app.33916

[38] Liu G-C., He Y-S., Zeng J-B., Li Q-T., Wang Y-Z.: Fully biobased and supertough polylactide-based thermoplastic vulcanizates fabricated by peroxide-induced dynamic vulcanization and interfacial compatibilization. Biomacromolecules, **15**, 4260–4271 (2014).
DOI: 10.1021/bm5012739

[39] Dorgan J. R., Jansen J., Clayton M. P., Hait S. B., Knauss D. M.: Melt rheology of variable L-content poly(lactic acid). Journal of Rheology, **49**, 607–619 (2005).
DOI: 10.1122/1.1896957

[40] Liang J-Z., Zhou L., Tang C-Y., Tsui C-P.: Crystalline properties of poly(L-lactic acid) composites filled with nanometer calcium carbonate. Composites Part B: Engineering, **45**, 1646–1650 (2013).
DOI: 10.1016/j.compositesb.2012.09.086

[41] Hughes J., Thomas R., Byun Y., Whiteside S.: Improved flexibility of thermally stable poly-lactic acid (PLA). Carbohydrate Polymers, **88**, 165–172 (2012).
DOI: 10.1016/j.carbpol.2011.11.078

[42] Day M., Nawaby V., Liao X.: A DSC study of the crystallization behaviour of polylactic acid and its nanocomposites. Journal of Thermal Analysis and Calorimetry, **86**, 623–629 (2006).
DOI: 10.1007/s10973-006-7717-9

[43] Yuryev Y., Wood-Adams P. M.: Crystallization of poly(L-/D-lactide) in the presence of electric fields. Macromolecular Chemistry and Physics, **213**, 635–642 (2012).
DOI: 10.1002/macp.201100448

[44] Pyda M., Bopp R. C., Wunderlich B.: Heat capacity of poly(lactic acid). The Journal of Chemical Thermodynamics, **36**, 731–742 (2004).
DOI: 10.1016/j.jct.2004.05.003

[45] Lee J. K., Lee K. H., Jin B. S.: Structure development and biodegradability of uniaxially stretched poly(L-lactide). European Polymer Journal, **37**, 907–914 (2001).
DOI: 10.1016/S0014-3057(00)00213-5

[46] Pillin I., Montrelay N., Bourmaud A., Grohens Y.: Effect of thermo-mechanical cycles on the physico-chemical properties of poly(lactic acid). Polymer Degradation and Stability, **93**, 321–328 (2008).
DOI: 10.1016/j.polymdegradstab.2007.12.005

[47] Żenkiewicz M., Richert J., Rytlewski P., Moraczewski K., Stepczyńska M., Karasiewicz T.: Characterisation of multi-extruded poly(lactic acid). Polymer Testing, **128**, 412–418 (2009).
DOI: 10.1016/j.polymertesting.2009.01.012

[48] Al-Itry R., Lamnawar K., Maazouz A.: Improvement of thermal stability, rheological and mechanical properties of PLA, PBAT and their blends by reactive extrusion with functionalized epoxy. Polymer Degradation and Stability, **97**, 1898–1914 (2012).
DOI: 10.1016/j.polymdegradstab.2012.06.028

[49] Hamad K., Kaseem M., Deri F.: Effect of recycling on rheological and mechanical properties of poly(lactic acid)/polystyrene polymer blend. Journal of Materials Science, **46**, 3013–3019 (2011).
DOI: 10.1007/s10853-010-5179-8

[50] Auras R., Harte B., Selke S.: Effect of water on the oxygen barrier properties of poly(ethylene terephthalate) and polylactide films. Journal of Applied Polymer Science, **92**, 1790–1803 (2004).
DOI: 10.1002/app.20148

[51] Auras R. A., Singh S. P., Singh J. J.: Evaluation of oriented poly(lactide) polymers vs. existing PET and oriented PS for fresh food service containers. Packaging Technology and Science, **18**, 207–216 (2005).
DOI: 10.1002/pts.692

[52] Thellen C., Orroth C., Froio D., Ziegler D., Lucciarini J., Farrell R., D'Souza N. A., Ratto J. A.: Influence of montmorillonite layered silicate on plasticized poly(L-lactide) blown films. Polymer, **46**, 11716–11727 (2005).
DOI: 10.1016/j.polymer.2005.09.057

[53] Chaiwong C., Rachtanapun P., Wongchaiya P., Auras R., Boonyawan D.: Effect of plasma treatment on hydrophobicity and barrier property of polylactic acid. Surface and Coatings Technology, **204**, 2933–2939 (2010).
DOI: 10.1016/j.surfcoat.2010.02.048

[54] Jamshidian M., Tehrany E., Cleymand F., Leconte S., Falher T., Desobry S.: Effects of synthetic phenolic antioxidants on physical, structural, mechanical and barrier properties of poly lactic acid film. Carbohydrate Polymers, **87**, 1763–1773 (2012).
DOI: 10.1016/j.carbpol.2011.09.089

[55] Bao L., Dorgan J. R., Knauss D., Hait S., Oliveira N. S., Maruccho I. M.: Gas permeation properties of poly (lactic acid) revisited. Journal of Membrane Science, **285**, 166–172 (2006).
DOI: 10.1016/j.memsci.2006.08.021

[56] Al-Mulla E. A. J., Yunus W. M. Z. W., Ibrahim N. A. B., Rahman M. Z. A.: Properties of epoxidized palm oil plasticized polytlactic acid. Journal of Materials Science, **45**, 1942–1946 (2010).
DOI: 10.1007/s10853-009-4185-1

[57] Martino V. P., Jiménez A., Ruseckaite R. A.: Processing and characterization of poly(lactic acid) films plasticized with commercial adipates. Journal of Applied Polymer Science, **112**, 2010–2018 (2009).
DOI: 10.1002/app.29784

[58] NatureWorks LLC: Sheet extrusion processing guide. Minnetonka (2005).

[59] Carrasco F., Cailloux J., Sánchez-Jiménez P. E., Maspoch M. L. I.: Improvement of the thermal stability of branched poly(lactic acid) obtained by reactive extrusion. Polymer Degradation and Stability, **104**, 40–49 (2014).
DOI: 10.1016/j.polymdegradstab.2014.03.026

[60] Sato Y., Inohara K., Takishima S., Masuoka H., Imaizumi M., Yamamoto H., Takasugi M.: Pressure-volume-temperature behavior of polylactide, poly(butylene succinate), and poly(butylene succinate-*co*-adipate). Polymer Engineering and Science, **40**, 2602–2609 (2000).
DOI: 10.1002/pen.11390

[61] Kale G., Auras R., Singh P.: Comparison of the degradability of poly(lactide) packages in composting and ambient exposure conditions. Packaging Technology and Science, **20**, 49–70 (2007).
DOI: 10.1002/pts.742

[62] Kale G., Auras R., Singh S. P.: Degradation of commercial biodegradable packages under real composting and ambient exposure conditions. Journal of Polymers and the Environment, **14**, 317–334 (2006).
DOI: 10.1007/s10924-006-0015-6

[63] Weng Y-X., Jin Y-J., Meng Q-Y., Wang L., Zhang M., Wang Y-Z.: Biodegradation behavior of poly(butylene adipate-*co*-terephthalate) (PBAT), poly(lactic acid) (PLA), and their blend under soil conditions. Polymer Testing, **32**, 918–926 (2013).
DOI: 10.1016/j.polymertesting.2013.05.001

[64] Kale G., Auras R., Singh S. P., Narayan R.: Biodegradability of polylactide bottles in real and simulated composting conditions. Polymer Testing, **26**, 1049–1061 (2007).
DOI: 10.1016/j.polymertesting.2007.07.006

[65] Kale G., Kijchavengkul T., Auras R., Rubino M., Selke S. E., Singh S. P.: Compostability of bioplastic packaging materials: An overview. Macromolecular Bioscience, **7**, 255–277 (2007).
DOI: 10.1002/mabi.200600168

[66] Ohkita T., Lee S-H.: Thermal degradation and biodegradability of poly (lactic acid)/corn starch biocomposites. Journal of Applied Polymer Science, **100**, 3009–3017 (2006).
DOI: 10.1002/app.23425

[67] Bain J. R.: Peripheral nerve allografting: Review of the literature with relevance to composite tissue transplantation. Transplantation Proceedings, **30**, 2762–2767 (1998).
DOI: 10.1016/S0041-1345(98)00804-5

[68] Langer R., Vacanti P.: Tissue engineering. Science, **260**, 920–926 (1993).
DOI: 10.1126/science.8493529

[69] Mitragotri S., Lahann J.: Physical approaches to biomaterial design. Nature Materials, **8**, 15–23 (2009).
DOI: 10.1038/nmat2344

[70] Zhang Q., Mochalin V. N., Neitzel I., Knoke I. Y., Han J., Klug C. A., Zhou J. G., Lelkes P. I., Gogotsi Y.: Fluorescent PLLA-nanodiamond composites for bone tissue engineering. Biomaterials, **32**, 87–94 (2011).
DOI: 10.1016/j.biomaterials.2010.08.090

[71] Saito N., Takaoka K.: New synthetic biodegradable polymers as BMP carriers for bone tissue engineering. Biomaterials, **24**, 2287–2293 (2003).
DOI: 10.1016/S0142-9612(03)00040-1

[72] Murakami N., Saito N., Horiuchi H., Okada T., Nozaki K., Takaoka K.: Repair of segmental defects in rabbit humeri with titanium fiber mesh cylinders containing recombinant human bone morphogenetic protein-2 (rhBMP-2) and a synthetic polymer. Journal of Biomedical Materials Research Part A, **62**, 169–174 (2002).
DOI: 10.1002/jbm.10236

[73] Chang P-C., Liu B-Y., Liu C-M., Chou H-H., Ho M-H., Liu L-C., Wang D-M., Hou L-T.: Bone tissue engineering with novel rhBMP2-PLLA composite scaffolds. Journal of Biomedical Materials Research Part A, **81**, 771–780 (2007).
DOI: 10.1002/jbm.a.31031

[74] Li G., Wang Z-X., Fu W-J., Hong B-F., Wang X-X., Cao L., Xu F-Q., Song Q., Cui F-Z., Zhang X.: Introduction to biodegradable polylactic acid ureteral stent application for treatment of ureteral war injury. BJU International, **108**, 901–906 (2011).
DOI: 10.1111/j.1464-410X.2010.09992.x

[75] Qin Y., Yuan M., Li L., Guo S., Yuan M., Li W., Xue J.: Use of polylactic acid/polytrimethylene carbonate blends membrane to prevent postoperative adhesions. Journal of Biomedical Materials Research Part B: Applied Biomaterials, **79**, 312–319 (2006).
DOI: 10.1002/jbm.b.30544

[76] Bhatia A., Gupta R. K., Bhattacharya S. N., Choi H. J.: Compatibility of biodegradable poly (lactic acid) (PLA) and poly (butylene succinate) (PBS) blends for packaging application. Korea-Australia Rheology Journal, **19**, 125–131 (2007).

[77] Fraisse F., Verney V., Commereuc S., Obadal M.: Recycling of poly(ethylene terephthalate)/polycarbonate blends. Polymer Degradation and Stability, **90**, 250–255 (2005).
DOI: 10.1016/j.polymdegradstab.2005.02.019

[78] Brekke J. H., Olson R. A. J., Scully J. R., Osbon D. B.: Influence of polylactic acid mesh on the incidence of localized osteitis. Oral Surgery, Oral Medicine, Oral Pathology, **56**, 240–245 (1983).
DOI: 10.1016/0030-4220(83)90003-8

[79] Kumari A., Yadav S. K., Yadav S. C.: Biodegradable polymeric nanoparticles based drug delivery systems. Colloids and Surfaces B: Biointerfaces, **75**, 1–18 (2010).
DOI: 10.1016/j.colsurfb.2009.09.001

[80] Leroux J-C., Allémann E., De Jaeghere F., Doelker E., Gurny R.: Biodegradable nanoparticles – From sustained release formulations to improved site specific drug delivery. Journal of Controlled Release, **39**, 339–350 (1996).
DOI: 10.1016/0168-3659(95)00164-6

[81] Fishbein I., Chorny M., Rabinovich L., Banai S., Gati I., Golomb G.: Nanoparticulate delivery system of a tyrphostin for the treatment of restenosis. Journal of Controlled Release, **65**, 221–229 (2000).
DOI: 10.1016/S0168-3659(99)00244-8

[82] Matsumoto J., Nakada Y., Sakurai K., Nakamura T., Takahashi Y.: Preparation of nanoparticles consisted of poly(L-lactide)–poly(ethylene glycol)–poly(L-lactide) and their evaluation *in vitro*. International Journal of Pharmacy, **185**, 93–101 (1999).
DOI: 10.1016/S0378-5173(99)00153-2

[83] Xing J., Zhang D., Tan T.: Studies on the oridonin-loaded poly(D,L-lactic acid) nanoparticles *in vitro* and *in vivo*. International Journal of Biological Macromolecules, **40**, 153–158 (2007).
DOI: 10.1016/j.ijbiomac.2006.07.001

[84] Rancan F., Papakostas D., Hadam S., Hackbarth S., Delair T., Primard C., Verrier B., Sterry W., Blume-Peytavi U., Vogt A.: Investigation of polylactic acid (PLA) nanoparticles as drug delivery systems for local dermatotherapy. Pharmaceutical Research, **26**, 2027–2036 (2009).
DOI: 10.1007/s11095-009-9919-x

[85] Gao H., Wang Y. N., Fan Y. G., Ma J. B.: Synthesis of a biodegradable tadpole-shaped polymer via the coupling reaction of polylactide onto mono(6-(2-aminoethyl)amino-6-deoxy)-β-cyclodextrin and its properties as the new carrier of protein delivery system. Journal of Controlled Release, **107**, 158–173 (2005).
DOI: 10.1016/j.jconrel.2005.06.010

[86] Fessi H., Puisieux F., Devissaguet J. P., Ammoury N., Benita S.: Nanocapsule formation by interfacial polymer deposition following solvent displacement. International Journal of Pharmaceutics, **55**, R1–R4 (1989).
DOI: 10.1016/0378-5173(89)90281-0

[87] Esmaeili F., Ghahremani M. H., Ostad S. N., Atyabi F., Seyedabadi M., Malekshahi M. R., Amini M., Dinarvand R.: Folate-receptor-targeted delivery of docetaxel nanoparticles prepared by PLGA–PEG–folate conjugate. Journal of Drug Targeting, **16**, 415–423 (2008).
DOI: 10.1080/10611860802088630

[88] Ling Y., Huang Y.: Preparation and release efficiency of poly (lactic-*co*-glycolic) acid nanoparticles for drug loaded paclitaxel. IFMBE Proceedings, **19**, 514–517 (2008).
DOI: 10.1007/978-3-540-79039-6_129

[89] Barber F. A., Elrod B. F., McGuire D. A., Paulos L. E.: Preliminary results of an absorbable interference screw. Arthroscopy: The Journal of Arthroscopic and Related Surgery, **11**, 537–548 (1995).
DOI: 10.1016/0749-8063(95)90129-9

[90] Matsusue Y., Nakamura T., Suzki S., Iwasaki R.: Biodegradable pin fixation of osteochondral fragments of the knee. Clinical Orthopaedics and Related Research, **322**, 166–173 (1996).

[91] Stähelin A. C., Weiler A., Rüfenacht H., Hoffmann R., Geissmann A., Feinstein R.: Clinical degradation and biocompatibility of different bioabsorbable interference screws: A report of six cases. Arthroscopy: The Journal of Arthroscopic and Related Surgery, **13**, 238–244 (1997).
DOI: 10.1016/S0749-8063(97)90162-6

[92] Böstman O., Hirvensalo E., Vainionpää S., Mäkelä A., Vihtonen K., Törmälä P., Rokkanen P.: Ankle fractures treated using biodegradable internal fixation. Clinical Orthopaedics and related research, **238**, 195–203 (1989).

[93] Lavery A., Higgins K. R., Ashry H. R., Athanasiou K. A.: Mechanical characteristics of poly-L-lactic acid absorbable screws and stainless steel screws in basilar osteotomies of the first metatarsal. Journal of Foot Ankle Surgery, **33**, 249–254 (1994).

[94] Bucholz R. W., Henry S., Henley M. B.: Fixation with bioabsorbable screws for the treatment of fractures of the ankle. Journal of Bone and Joint Surgery, **76**, 319–324 (1994).

[95] Casteleyn P. P., Handelberg F., Haentjens P.: Biodegradable rods versus Kirschner wire fixation of wrist fractures. A randomised trial. Journal Bone and Joint Surgery, **74**, 858–861 (1992).

[96] Hope P. G., Williamson D. M., Coates C. J., Cole W. G.: Biodegradable pin fixation of elbow fractures in children: A randomized trial. Journal Bone and Joint Surgery, **73**, 965–968 (1991).

[97] Haers P. E., Suuronen R., Lindqvist C., Sailer H.: Biodegradable polylactide plates and screws in orthognathic surgery: Technical note. Journal of Cranio-Maxillofacial Surgery, **26**, 87–91 (1998).
DOI: 10.1016/S1010-5182(98)80045-0

[98] van Sliedregt A., Radder A. M., de Groot K., van Blitterswijk C. A.: *In vitro* biocompatibility testing of polylactides Part I Proliferation of different cell types. Journal of Materials Science: Materials in Medicine, **3**, 365–370 (1992).
DOI: 10.1007/BF00705369

[99] Majola A., Vainionpää S., Vihtonen K., Mero M., Vasenius J., Törmälä P., Rokkanen P.: Absorption, biocompatibility, and fixation properties of polylactic acid in bone tissue: An experimental study in rats. Clinical Orthopaedics and Related Research, **268**, 260–269 (1991).

eXPRESS Polymer Letters Vol.9, No.5 (2015) 456–468
Available online at www.expresspolymlett.com
DOI: 10.3144/expresspolymlett.2015.43

The influence of polysilane chemical structure on optical properties, rubbed film morphology and LC alignment

M. Soroceanu, A. I. Barzic, I. Stoica, L. Sacarescu, V. Harabagiu*

'Petru Poni' Institute of Macromolecular Chemistry, Aleea Grigore Ghica Voda 41A, 700487 Iasi, Romania

Received 26 September 2014; accepted in revised form 6 December 2014

Abstract. Polysilane films were prepared by the drop casting method and their optical and morphological properties have been analyzed in order to investigate their suitability as alignment layers for nematic molecules. The samples do not absorb the radiations in the visible domain, particularly those containing methylhydrosilyl units, and present a transmittance of about 90% starting from 390 to 1100 nm. The optical band-gap is higher than 3.26 eV for all polysilanes indicating a low probability of optical absorption processes in the visible range. The morphology of the pristine samples shows isotropically distributed granular formations. The polymer surface was oriented by rubbing with two types of velvet: one with short fibers and the other with long fibers. The latter generates higher surface anisotropy, as shown by the reduction of the surface texture direction index values. The presence of methylhydrosilyl units allows a denser packing of the polymer structure and thus finer surface periodicities, leading to better orientation of the nematic molecules on the polysilane surface.

Keywords: *material testing, polysilane, rubbing, morphology, LC alignment*

1. Introduction

In the last years, devices based on liquid crystal display (LCD) have evolved rapidly as a result of strong competition among the other display technologies including cathode ray tube (CRTs) and plasma display panel (PDPs) [1]. Given their advantages, such as lightweight, low power consumption, and low-voltage operation, LCDs occupy the largest proportion of the entire display market [2]. Therefore, such devices are commonly encountered in every aspects of everyday life, including manufacturing of watches, cellular phones, notebook computers and wide screen televisions.

The basic element of the LCD is represented by the liquid crystal (LC) cell, consisting of a layer of nematic molecules, sandwiched between two glass substrates [3]. They are covered with an organic or inorganic compound, like SiO_2 or other oxides, which provides a monodomain within the LC. The performance of such devices relies in the homogeneous, defect-free alignment of the LC interacting with the organic (e.g. polymer) layer. Improved orientation of the mesogens can be achieved by a proper surface treatment of the substrates between which the LC layer is interposed, also called alignment layers. There are several different methods of LC alignment layer preparation, such as photoalignment, and Langmuir-Blodgett (LB) layer deposition, but one of the most used is mechanical rubbing of polymer films with a velvet cloth [4]. This technique is successfully used in the production process of large displays currently manufactured.

The continuous evolution of LCDs lies in the development of both current technologies and available materials. Literature surveys [5–8] on this subject show that many efforts have been made to control and/or improve the viewing angle, the contrast, the response time and the transparency of the alignment

*Corresponding author, e-mail: irina_cosutchi@yahoo.com

layer in the visible domain. The surface morphology of the rubbed alignment layer, the pretilt angle and surface energy of the alignment film are influenced by the conformation of the polymer molecular backbone [9].

Many studies are focused on preparing alignment layers by rubbing polyimides [10–13], poly(vinylidene fluoride) [14] or polyamides [15]. Since the absorption characteristics of alignment layer determines unwanted light-transmission modulation of the liquid crystal leading to ghost images on the LCD panel [16, 17], the investigations are focused on transparent polymers with good surface alignment ability.

Another class of transparent polymers is represented by polysilanes. They consist of chains exclusively made up of silicon atoms with significant delocalization of the sigma electrons along the backbone. This aspect leads to interesting electrical and optical properties, such as high quantum efficiency of charge generation, high charge-carrier mobility, efficient luminescence, and optical non-linearity [18]. Their photophysical properties are strongly influenced by the chemical structure of the polymer side groups and/or dimensionality of the skeletal framework [19, 20]. To our knowledge there are no investigations on polysilane-based alignment layers patterned by rubbing.

Previous papers [21–23] showed that polysilanes exhibit good ability of aligning molecules. The morphological features of these polymers are affected by UV exposure due to the scission of the main chain and oxidation processes [21]. Since UV-irradiated polysilane generated different orientation of nematic molecules from that induced non-irradiated polymer, patterning of surface orientation should be possible by partial UV-irradiation. It was shown that the friction-transferred polysilane film patterned by UV exposure with a shadow mask determines the patterned orientation of 5CB. Therefore it was reported that this type of polymer films could be used in practical applications as patternable LC alignment layers [21].

Having all these in view, the present work is concerned with the research of different polysilane structures as suitable layer for LC alignment through conventional rubbing technology. For this purpose, four polysilanes having methyl, phenyl and hydrogen side groups in various combinations have been synthesized. Then, thin films have been casted onto quartz glasses and their optical properties like energy gap or other energies describing the absorption edge, were analyzed in connection with the polymer chemical structure. This type of optical analysis on polysilanes using the method proposed by Tauc [24] and Mott and Davis [25] is not reported yet in the literature.

The surface morphology was studied first and subsequently adapted by rubbing with two types of velvet. The surface features are discussed in relation with both chemical structures of the polysilane and patterning conditions. The alignment capacity of polysilane films was further tested using a nematic LC.

2. Experimental

2.1. Starting materials

4′-pentyl-4-biphenylcarbonitrile (5CB, Sigma Aldrich, Saint Louis, USA) nematic crystalline compound was used as received.

2.2. Polysilane synthesis

Polysilanes with structures represented in Figure 1 have been synthesized using the heterogeneous Wurtz coupling technique of appropriate monomers. Details concerning the synthesis method, properties of the comonomers in relation with the reaction conditions and methods to protect the methylhydrosilyl structural integrity have been described in previous works [26–28]. The physico-chemical characteristics of the studied polysilanes are presented in Table 1.

Polysilanes film samples have been prepared on quartz slides by drop casting of a 1% polymer solution in toluene and overnight drying at room temperature. For this purpose the quartz slides were cleaned in a HNO_3 bath for 2 h then ultrasonicated for 5 minutes in acetone, washed with toluene and dried in air. The average thickness of polysilane films vary between 10 and 20 μm (Table 1). For each sample 5 plates were prepared and the standard deviation for average thickness was determined and listed in Table 1.

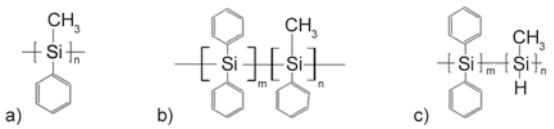

Figure 1. Chemical structures of the studied polysilanes: (a) polymethylphenylsilane (PMePhS), (b) poly(diphenyl-co-methylphenyl)silane (P(DPh-MePhS)), (c) poly(diphenyl-co-methyl(H))silane (P(DPh-MeHS)) for m/n = 1 and P(DPh-MeHS) 7/1 for m/n = 7/1

Table 1. Physico-chemical properties of polysilanes and thickness of polysilane films

Sample code	$M_w \cdot 10^3$ [g/mol]	M_w/M_n [GPC]	DPh/MePh [molar ratio]	DPh/MeH [molar ratio]	Average film thickness [μm]
PMePhS	3.8	1.20	–	–	15±0.35
P(DPh-MePhS)	4.6	1.21	7/1	–	10±0.31
P(DPh-MeHS)	3.2	1.50	–	1/1	20±0.21
P(DPh-MeHS) 7/1	4.1	1.18	–	7/1	10±0.28

2.3. Characterization

The absorption spectra of the films were recorded using a SPECORD 200 Analytik Jena UV/VIS spectrometer (Jena, Germany).

Surface rubbing was performed with a laboratory made device consisting in a cylinder covered with velvet having a diameter of 12 mm and a rotation speed of 200 rpm (rotatio/minute). The polymer films were processed for 30 seconds, using two types of velvet: one with short and rigid cotton fibers (Vsf) and the other made of long and flexible acrylic fibers (Vlf). The pile impression was 0.8 mm and the plate of our instrument was fixed (its speed was zero).

The texture of the rubbing fabrics was investigated on an Environmental Scanning Electron Microscope (ESEM) type Quanta 200 (FEI, Eindhoven, The Netherlands).

Polarized light microscopy (PLM) images were recorded on an Olympus BH-2 polarized light microscope (Olympus Corporation, Tokyo, Japan), at 400× magnification.

The surface morphology was investigated by the Solver PRO-M, (NTMDT, Zelenograd, Russia) Scanning Probe Microscope (AFM) equipped with a commercially available NSG10 cantilever. The theoretical spring constant of the cantilever was 11.8 N/m, the resonant frequency was 228 kHz and the manufacturer's value for the probe tip radius was 10 nm. All AFM images were collected in tapping mode, in air, at room temperature. Different scanning areas starting from 20×20 μm^2 down to 3×3 μm^2 have been analyzed. For illustration purpose, scanning lengths of 5 and 10 μm for pristine and rubbed samples respectively have been chosen because the morphological features were easier to observe. However, all the texture parameters were calculated from the AFM data obtained over the 10×10 μm^2 scanning area.

3. Results and discussion

3.1. Optical properties

Polymethylphenylsilane, PMePhS, is a homopolymeric structure composed of methylphenylsilane units. It was widely studied in previous reports [19] and is used in this study for comparison reasons. Poly (diphenyl-co-methylphenyl)silane, P(DPh-MePhS), was designed as a statistical copolymeric architecture structure, where the molar ratio of the comonomeric structural units is M_r = 7/1. The most interesting are the poly(diphenyl-co-methyl(H))silane copolymers known also as polyhydrosilanes. This work is focused on two polyhydrosilanes having different content of methylhydrosilyl units: P(DPh-MeHS) with M_r = 1 and P(DPh-MeHS) 7/1 having M_r = 7/1.

The transparency of the polysilane films was studied within the 200–1100 nm spectral range. The UV-VIS spectra presented in Figure 2 reveal that samples do not absorb visible light, having a transmittance of about 90% in the domain starting from 450 nm to near infrared domain. One may observe that the transparency band can be extended to the UV region depending on polysilane substituent nature. The introduction of specific side groups could influence the position of the cut-off wavelength (the wavelength at which the transmittance becomes less than 1% in the spectrum). Therefore, polysilanes containing rigid methylphenyl segments present higher cut-off wavelengths (Figure 2 inset).

The transmission characteristics of the investigated films in the visible domain are optimal for LC alignment. Moreover, the sharp fall in the UV region can offer information on the band gap. This parameter and the energies describing the absorption edges are

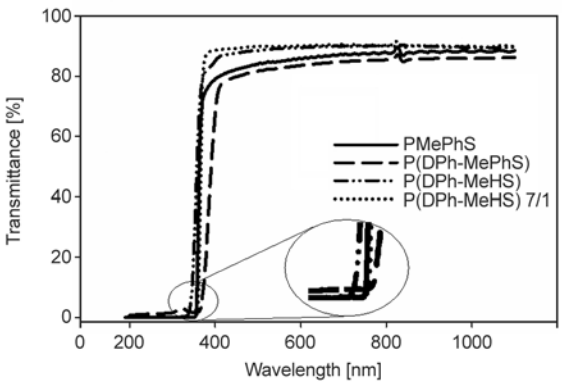

Figure 2. The UV-VIS spectra of the studied polysilane films

determined using the approach of Tauc [24] and Mott and Davis [25]. The method starts from the evaluation of the optical absorption dependence on photon energy, reflecting the type of optical transitions. The absorption coefficient, α, is calculated using Equation (1):

$$\alpha = \frac{1}{d} \cdot \ln\left(\frac{1}{T}\right) \quad (1)$$

where d is the polymer film thickness and T is the transmittance.

The dependence of the absorption coefficient versus photon energy for most amorphous materials presents three domains: (1) absorption due to the interband transition near the optical band-gap, (2) absorption below the optical gap defines Urbach edge caused by the electric fields produced by charged impurities and other possible sources of internal electric fields and (3) optical absorption at low energies produced by structural defects, referring to the weak absorption Urbach tail.

Figure 3 shows the absorption coefficient as a function of incident photon energy, E, for the studied polysilanes. It can be noticed that the shape of the obtained curves is similar to that proposed by Tauc for a typical amorphous compounds [24]. Each of the absorption edges from Figure 3 exhibits two different domains, characterized by different slopes. Both exponential parts follow the Urbach rule [29] given by Equation (2):

$$\alpha \propto \exp\left(\frac{h\nu}{B}\right) \quad (2)$$

where B becomes either Urbach energy, E_u, in the high-energy exponential region or Tauc energy, E_t, describing the low-energy exponential part of the absorption coefficient.

The values of E_u and E_t of the polysilane films are obtained from the reverse of the slope of the dependence of absorption coefficient on photon energy in the two domains depicted in Figure 3. It can be noticed that the results displayed in Table 2 are influenced by the substituent type and the copolymer composition. The different absorption capacities of the samples in the low-energy absorption domain can be explained by considering the fact that in this energy region take place transitions involving defect states in the tails of the states density. Thus, the presence of structural defects, like the break or torsion of polymer chains, determines the occurrence of the optical absorption processes. The combination of the flexible methyl or bulky phenyl side groups into polysilane backbone could favor structural disorder and hence the increase of the E_t and E_u values. In the sample P(DPh-MePhS), where the diphenylsilyl segments are connected through bulky methylphenyl units, significant distortions can be produced leading to defects and higher values for E_u and E_t energies. When the coupling of the diphenylsilyl is made through an elastic segment, such as methyl(H)silyl (in P(DPh-MeHS) and P(DPh-MeHS) 7/1), all tensions are dissipated by local modification of the polymer conformation, resulting in lower values for the width of the tails of localized states.

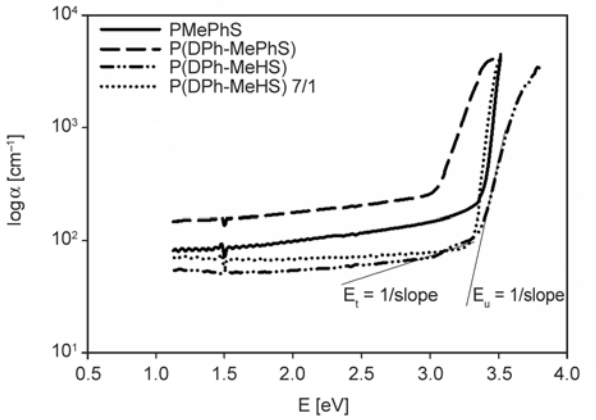

Figure 3. Absorption coefficient dependence on photon energy for the investigated polysilanes

Table 2. The values of Tauc energy, E_t, Urbach energy, E_u, and optical band-gap, E_g, of the studied polysilanes

Sample	E_t [meV]	E_u [meV]	E_g [eV]
PMePhS	3367.1	127.6	3.37
P(DPh-MePhS)	4310.3	319.4	3.21
P(DPh-MeHS)	2173.9	277.3	3.29
P(DPh-MeHS) 7/1	1785.7	121.2	3.35

The interband transitions in the high absorption region are expressed through another optical parameter, namely the optical band-gap, E_g. This energy is evaluated from the analysis of the spectral dependence of absorption at the highest energies of incident photons. The theory developed by Tauc [24] and Mott and Davis [25] for amorphous materials allows the determination of the optical band-gap from the intercept with x-axis of the dependence expressed by relation (3):

$$\alpha = C(E - E_g)^2 \quad (3)$$

where C is a constant.

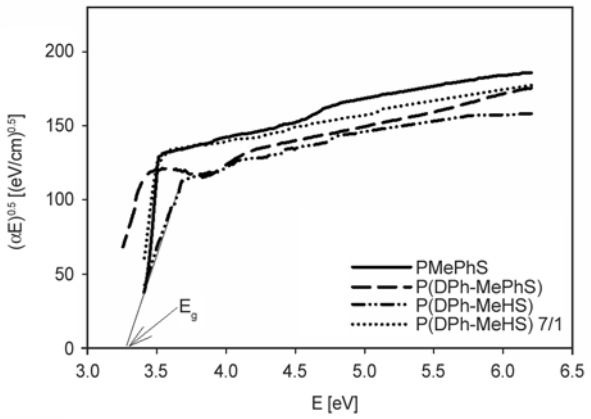

Figure 4. The Tauc dependence for the investigated polysilanes

This approach has been also applied earlier for amorphous polymer foils [30–32]. The Tauc plots for the investigated polysilanes, displayed in Figure 4, present a saturation domain at high energies followed by an exponential one in the low energies range, from which were extracted the values of the optical band-gap energy (Table 2). It can be noted that the obtained values increase with decreasing the polarizability of the polymer. Therefore, the different types of chain conjugation affect the E_g values. In P(DPh-MePhS) containing diphenylsilyl segments linked through methylphenilsilyl there is a synergetic effect on E_g caused by both σ–σ and σ–π conjugations, leading to a reduction of the optical band-gap. In P(DPh-MeHS) 7/1 only σ–σ conjugation has continuity since the σ–π one is interrupted by the short chain of methylhydrosilyl. This results in slightly higher values of Eg. The same tendency is noticed for P(DPh-MeHS), which contains methyl (H)silyl units, where the lower probability of electrons delocalization eliminates the possibility of optical absorption processes. Nevertheless, all samples exhibit optical band-gap energy higher than 3.26 eV, which is a good indicator of transparent polymer films [28].

Considering the good optical properties of the prepared polymer films, it can be concluded that they meet the transparency requirements encountered for liquid crystal alignment layers.

3.2. Surface morphology

The investigations continued with morphological analysis of polysilane films in order to check their surface organization ability (after rubbing) and implicitly their LC alignment properties [33].

For a better understanding of the effects created by the rubbing velvet fibers a comparative analysis between the pristine films and the patterned ones was performed. The changes occurring in the polysilane surface features were closely examined by AFM investigations. Figure 5 reveals that the topography of the unrubbed polymers is determined by the structural peculiarities. Thus, the morphological aspects can be associated with the different packing abilities of the studied polysilanes, due to the side groups, which induce a different flexibility for each macromolecule. The presence of bulky and rigid methylphenyl units in the polymer structure (PMePhS or P(DPh-MePhS)) favor the conformational disorder, thus the chain packing is diminished and the surface roughness increases resulting in granular formations of nanometric dimensions. In P(DPh-MeHS) or P(DPh-MeHS) 7/1 samples, the introduction of non-bulky and flexible methyl(H)silyl segments enhance the chain mobility and conformational order. This leads to a closer chain packing, with lower free volume as reflected by smaller root mean square roughness (S_q) and implicitly flatter structural formations (Table 3). The variation of S_q does not influence the LC alignment as much as the surface uniformity and anisotropy.

For an easy evaluation of the spatial properties of the surface, two texture parameters were used, namely texture direction index, S_{tdi} (which shows the degree of surface orientation) and texture aspect ratio, S_{tr} (which identifies the uniformity of the surface texture, isotropy *vs*. anisotropy). These parameters

Table 3. The values of texture direction index, S_{tdi}, and texture aspect ratio, S_{tr}, and root mean square roughness, S_q, for the studied polysilanes before and after rubbing with velvet having short (Vsf) and long fibers (Vlf), respectively

Sample	Texture direction index, S_{tdi}	Texture aspect ratio, S_{tr}	S_q [nm]
PMePhS	0.638	0.141	19
PMePhS - Vsf	0.420	0.080	12
PMePhS - Vlf	0.442	0.040	11
P(DPh-MePhS)	0.744	0.125	52
P(DPh-MePhS) - Vsf	0.443	0.074	19
P(DPh-MePhS) - Vlf	0.493	0.052	30
P(DPh-MeHS)	0.749	0.460	0.9
P(DPh-MeHS) - Vsf	0.403	0.095	32
P(DPh-MeHS) - Vlf	0.589	0.090	21
P(DPh-MeHS) 7/1	0.699	0.528	0.6
P(DPh-MeHS) 7/1 - Vsf	0.460	0.078	31
P(DPh-MeHS) 7/1 - Vlf	0.322	0.075	11

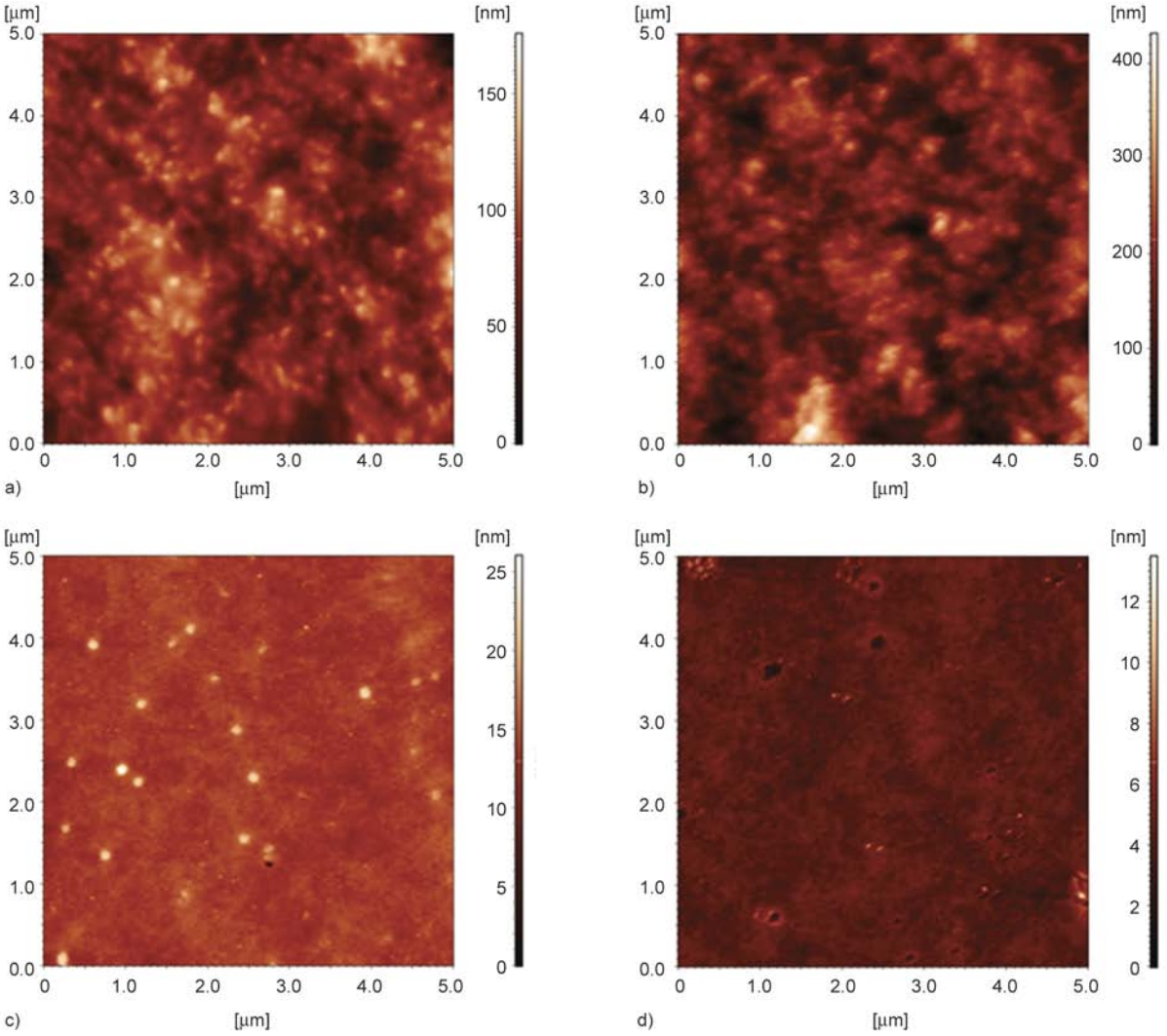

Figure 5. The 2D-AFM images of the pristine polysilane films: (a) PMePhS, (b) P(DPh-MePhS), (c) P(DPh-MeH)S and (d) P(DPh-MeH)S 7/1

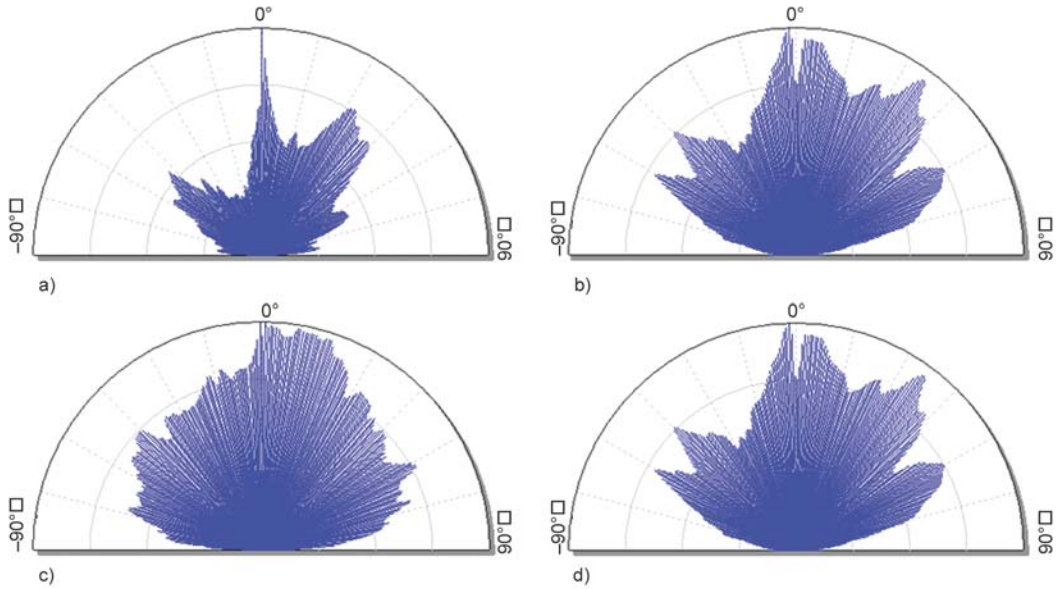

Figure 6. Fourier angular spectra derived from the 2D-AFM images of the pristine polysilane films: (a) PMePhS, (b) P(DPh-MePhS), (c) P(DPh-MeH)S and (d) P(DPh-MeH)S 7/1

were calculated based on the Fourier angular spectrum and provided information about the directional preference of the structures in the surface. The topographical AFM images (Figure 5) and the aspect of the corresponding Fourier angular spectra (Figure 6) obtained for all four pristine films suggest surfaces without apparent orientation. These findings are supported by the higher values of S_{tdi} and S_{tr} parameters shown in Table 3, indicating that the surfaces are isotropic, having the same characteristics in every direction.

In order to produce a proper orientation of the nematic 5CB, the polysilane films surfaces were adapted by rubbing with two velvet fabrics having different characteristics of the constituent fibers. It is well known that each fiber tip comprises subfibrous filaments that have a broad range of diameters, from a few submicrometers to a few micrometers. The contact of the filaments with the polysilane film during rubbing could generate microroughness and also the reorganization of the chains at the surface because of the temperature rise. In our experiments we used velvet having short and rigid fibers (Vsf) and velvet made from long and flexible fibers (Vlf). The aspect, shape, and size of these two types of textile fibers are analyzed by ESEM, as presented in Figure 7. According to this investigation, the material Vsf presents fibers with 950 μm length and 15 μm thickness, whereas Vlf fibers with 4000 μm length and 23 μm thickness.

The AFM data show that for all polysilane films the structural formations (randomly distributed on the surface) become less prevalent and fine microgrooves lines appear parallel to the rubbing direction. According to Berreman model [33], this type of surface organization is essential for inducing a good alignment of LC molecules. The detailed modifications induced in sample's surface topography during rubbing with the two types of velvet are reflected in bidimensional AFM images and their corresponding Fourier angular spectra (Figures 9–11).

The changes resulted in the morphology of the investigated samples might be explained by considering the chemical structure of the polymer, which determines through its organization a specific deformation response of the film surface during processing. In other words, when the chain conformation determines denser packing it can be assumed that the hardness increases producing only weakly developed structure at the surface, while a more ductile polymer is deformed more easily, producing relatively well-developed structure. The rigid linking methylphenyl units lead to a reduced chain packing resulting in a less organized structure, which allows deeper penetration of the velvet fibers (as seen in Figures 8 and 9 for samples PMePhS and P(DPh-MePhS)). Conversely, the presence of the flexible methylhydrosilyl coupling segments (methyl groups) results in a more compact polymer structure and this generates a smaller depth of the formed microgrooves (as seen in Figures 10 and 11 for samples P(DPh-MeHS) and P(DPh-MeHS) 7/1).

Another essential factor which strongly influences the resulting morphological features is the type of the fabric fibers. The material constituted from short and tough fibers (velvet Vsf) penetrates better with

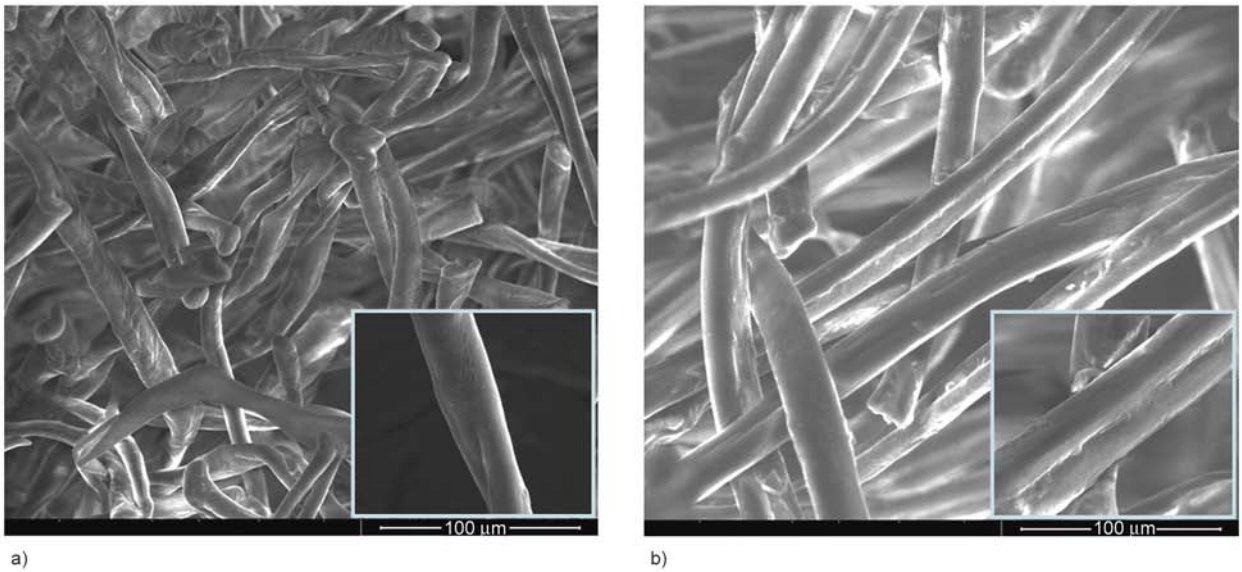

Figure 7. ESEM images obtained for (a) velvet with short fibers (Vsf) and (b) velvet with long fibers (Vlf)

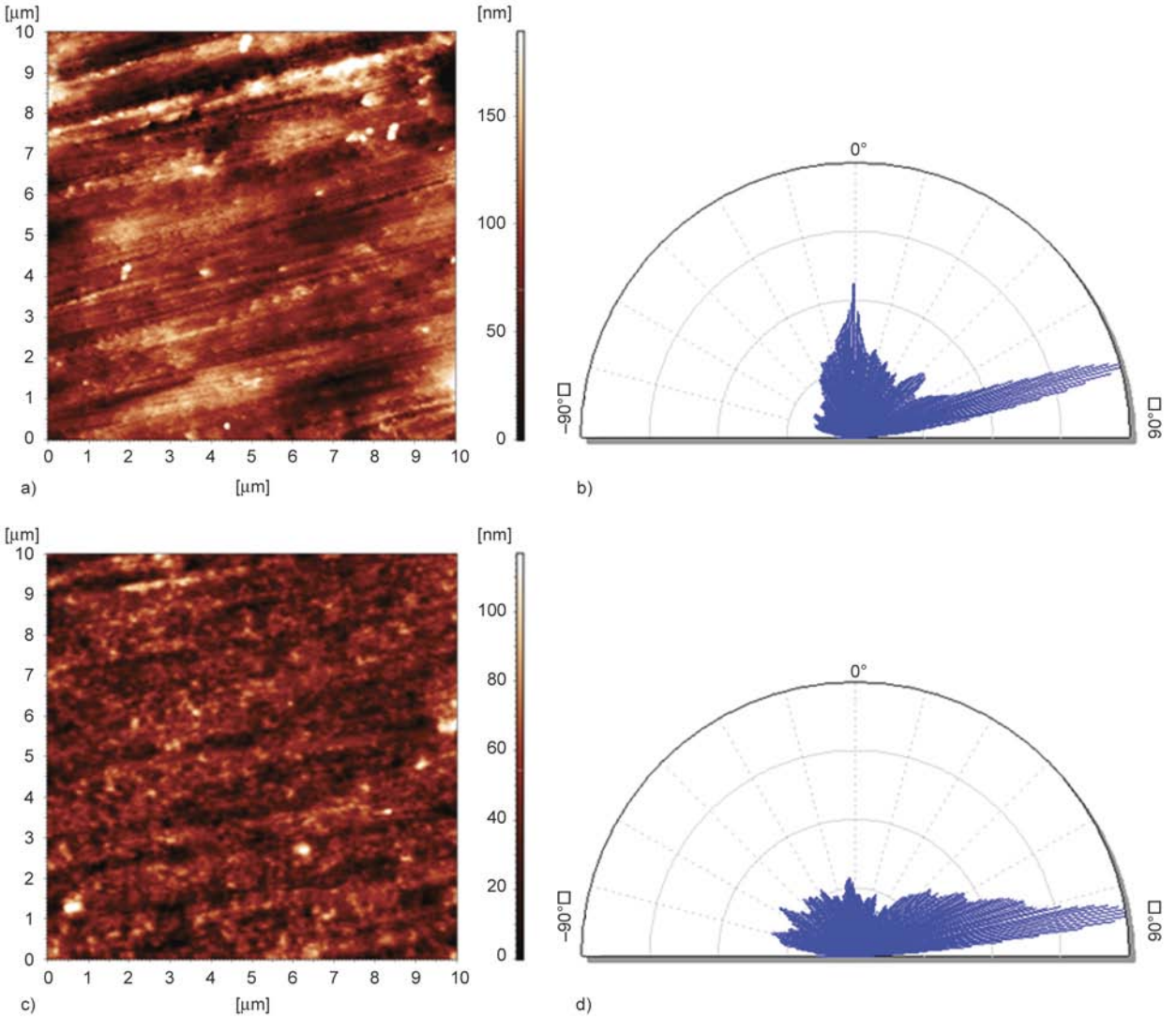

Figure 8. 2D-AFM image (a, c) and the corresponding Fourier angular spectra (b, d) for PMePhS film rubbed with velvet with short fibers (Vsf) and velvet with long fibers (Vlf), respectively

the tip the sample surface, resulting in more intense racks. The textile having long and flexible fibers (velvet Vlf), tends to bend more during rubbing, diminishing the depth of the surface grooves created on polysilane films. Thus, during patterning, the polymer surface predominantly interacts with sides of the fiber than with its tip. For all the studied polysilanes, except P(DPh-MePhS), a better regularity of surface topography is achieved when they are rubbed with Vlf. For P(DPh-MePhS) film, whatever the rubbing fiber, the depth of the microgrooves is almost the same, possibly due to its prevalently aromatic structure. Previous investigations showed that polymers containing aliphatic units develop more uniform pattern during rubbing with natural fibers like Vsf, while aromatic structures adopt the mentioned surface features when are processed with synthetic fibers (in our case Vlf) [10]. In addition, alignment layer orientation mechanism is not only determined by the mechanical contact, but also by the temperature rise of the layer that causes the polymer chain reorientation.

The values of S_{tdi} and S_{tr} parameters (Table 3) calculated from the Fourier angular spectra (Figures 9–11) were significantly lower for all the rubbed polymer films, comparatively with those observed at the unrubbed ones. This indicates that the surface was oriented and periodic structures were induced by the rubbing process. Additionally, the smaller values of the S_{tr} ratio ($S_{tr} < 0.1$) indicate stronger anisotropy, much more evident in the case of samples rubbed with synthetic velvet fibers.

3.3. Testing of LC alignment ability

The mechanism of LC molecules orientation on rubbed polymer films is determined by various fac-

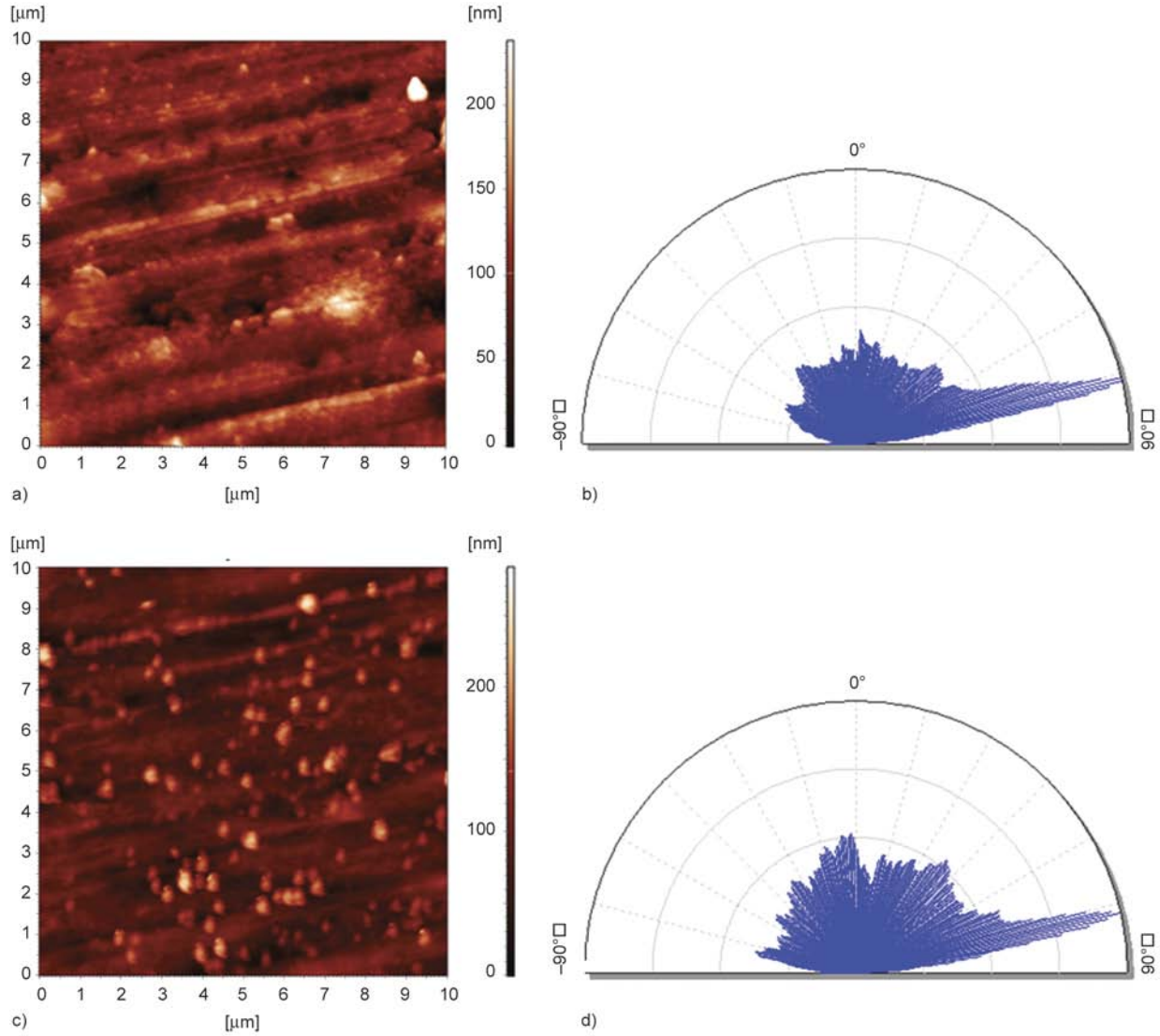

Figure 9. 2D-AFM image (a, c) and the corresponding Fourier angular spectra (b, d) for P(DPh-MePhS) film rubbed with velvet with short fibers (Vsf) and velvet with long fibers (Vlf), respectively

tors including surface topography and intermolecular interactions. However, which of these two aspects play the major role is not fully understood. The alignment mechanism of the nematic molecules is the result of two effects: liquid crystal orientational elasticity in connection with an induced surface pattern [33] and short-range interactions on the molecular scale [34, 35]. Taking into consideration the surface features of the polysilanes and the characteristics derived from their structure, the alignment mechanisms are discussed by considering the surface periodicity and uniformity as the main factor which induces the LC orientation.

The alignment behavior of 5CB on polysilanes, rubbed with the two types of velvet, is tested by PLM. The employed approach provides preliminary indications about the quality of nematic orientation. The method is based on recording the changes in light intensity when rotating the sample (placed under crossed polarizers). For all films, dark regions are recorded at 0 and 90° rotation of the LC director with respect to the crossed polarizers, revealing that it is aligned parallel to the polarizers' transmission direction. Further rotation of the polymer film from this position at 45 and 135° relative to the crossed polarizers, bright states are observed since the electric field components passing through the easy direction of 5CB have the highest resultant on the analyzer transmission direction. This behavior is characteristic for a homogeneous alignment of a nematic LC. Given the regularity of the induced grooves it can be noticed that the higher uniformity of the surfaces rubbed with Vlf leads to a higher contrast between the dark and bright states (as seen in Figure 12). This is indica-

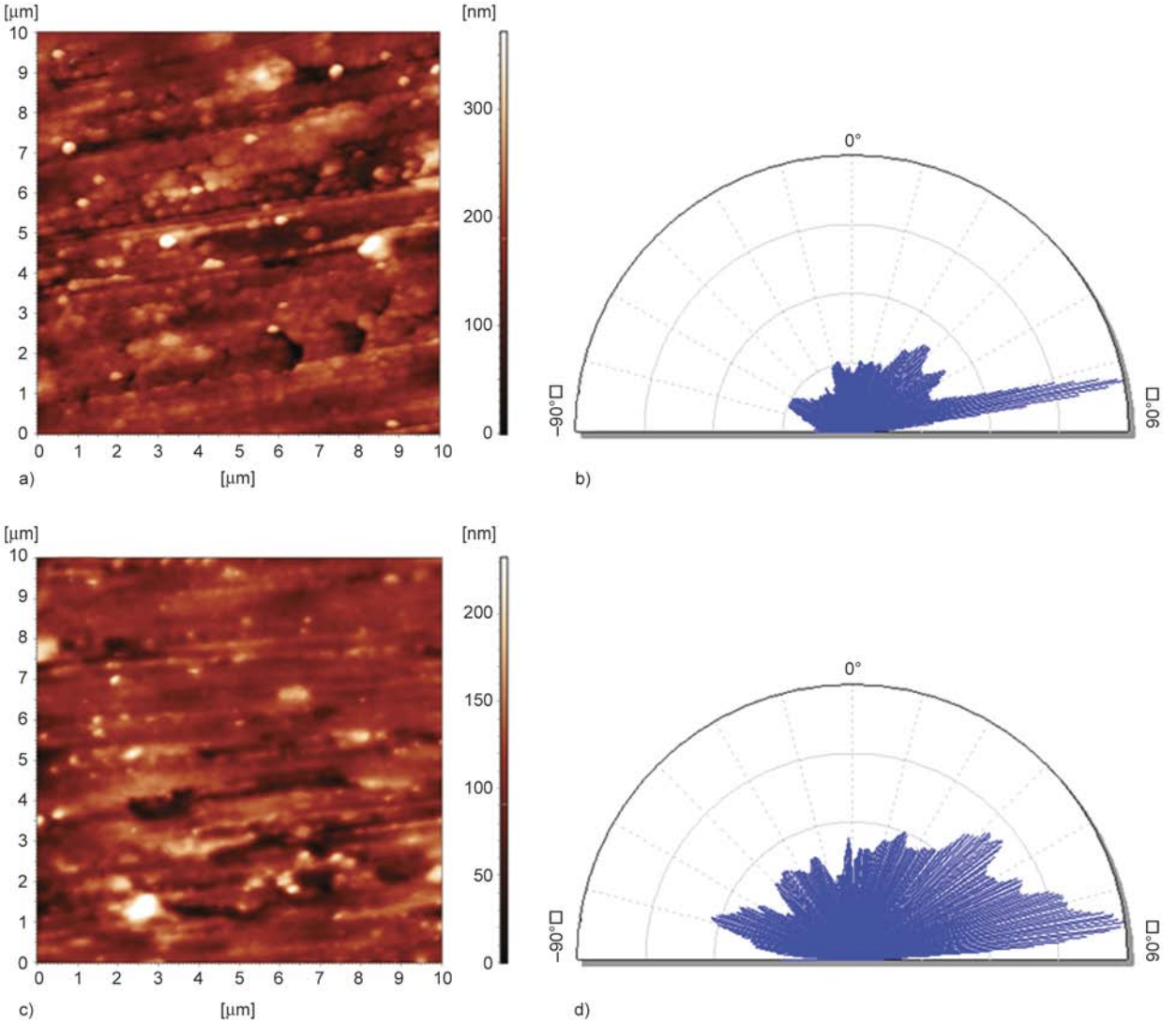

Figure 10. 2D-AFM image (a, c) and the corresponding Fourier angular spectra (b, d) for P(DPh-MeH)S film rubbed with velvet with short fibers (Vsf) and velvet with long fibers (Vlf), respectively

tive that the 5CB orientation is more uniform in the case of Vlf. The alignment of 5CB is relatively poor for samples PMePhS and P(DPh-MePhS) samples, regardless the rubbing fabric, can be explained by considering their less flexible structure that leads to less deep surface grooves. Thus, the performance of alignment abilities is higher for the samples containing methylhydrosilyl units, namely P(DPh-MeHS) and P(DPh-MeHS) 7/1. Considering the transparency and surface morphology, it can be concluded that this type of polysilane films meets the requirements for alignment layers.

4. Conclusions

A series of polysilanes films was prepared in order to investigate their optical and morphological properties for LC alignment purposes. The influence of the specific chemical structure over the optical properties of the polylsilane was investigated resulting that introduction of less polarizable methylhydrosilyl units into the polymer backbone improves the transparency. All samples present a transmittance of about 90% in the range of 450–1100 nm. The Urbach energy tends to increase for the samples with rigid methylphenyl segments (PMePhS or P(DPh-MePhS)), which facilitate less chain packing and implicitly a more disordered structure. Optical band-gap is higher than 3.26 revealing a low probability of optical absorption processes, thus sustaining the suitability of the samples as alignment layers from the point of view of lack of absorption in the visible domain. The morphology of the pristine polysilanes is constituted from isotropically distributed granular formations. In order to obtain a proper alignment of a nematic LC the surface of the samples was adapted by rubbing with two different velvets: one

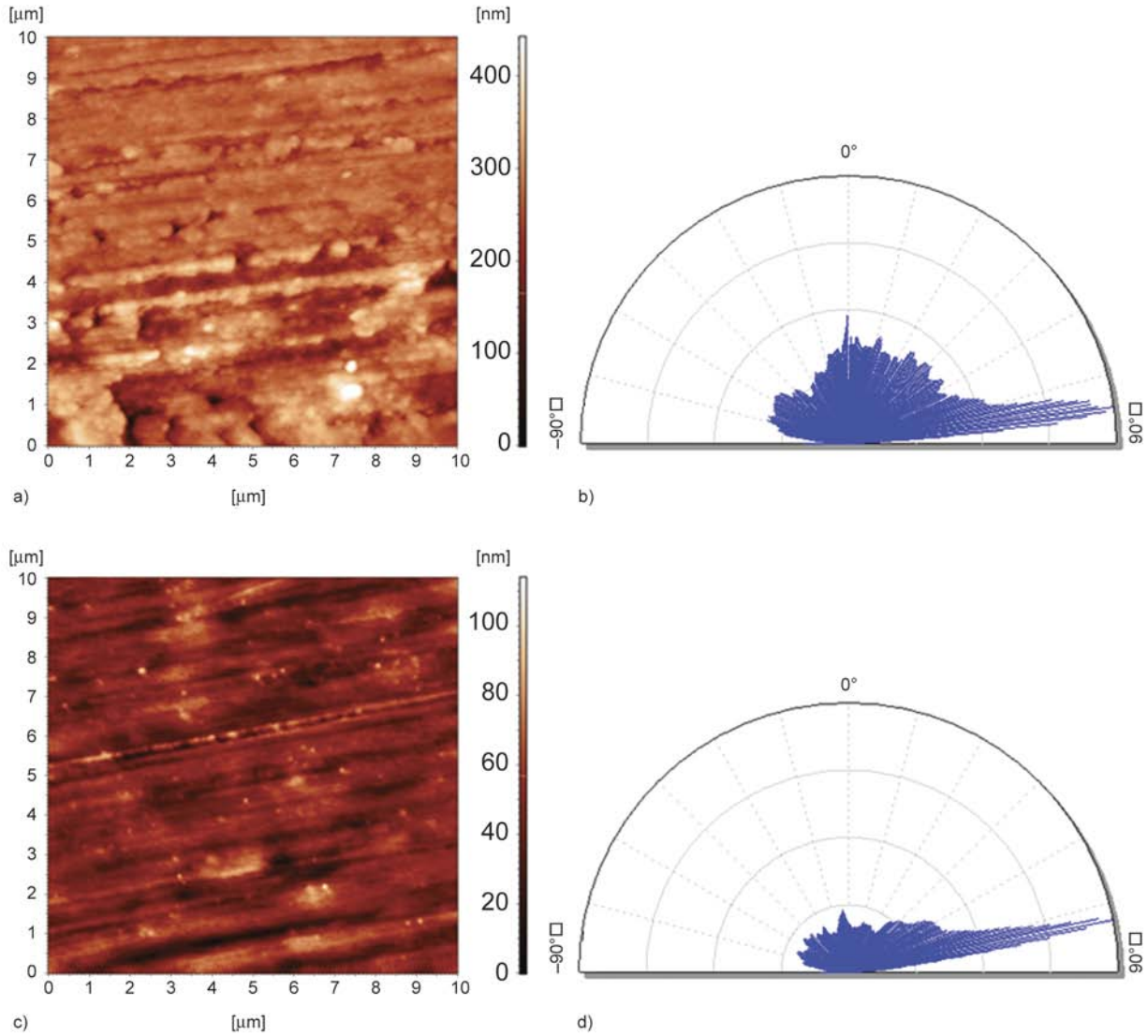

Figure 11. 2D-AFM image (a, c) and the corresponding Fourier angular spectra (b, d) for P(DPh-MeH)S 7/1 film rubbed with velvet with short fibers (Vsf) and velvet with long fibers (Vlf), respectively

with short fibers and other with longer fibers. The polymers containing methylhydrosilyl units present a more compact structure. Hence, finer grooves are formed at the polymer surface, leading to a better orientation of the 5CB nematic. Also, the velvet with longer fibers generates surfaces with higher uniformity facilitating a positive contribution to the LC alignment. This is supported by the higher contrast between the bright and dark states recorded by PLM. Considering the transparency and surface morphology of the samples containing more methyl substituents, it can be concluded that this type of polyhydrosilane are good candidates as alignment layers for LCDs.

References

[1] Kim K-H., Song J-K.: Technical evolution of liquid crystal displays. NPG Asia Materials, **1**, 29–36 (2009). DOI: 10.1038/asiamat.2009.3

[2] Kim S. S.: Invited paper: Super PVA sets new state-of-the-art for LCD-TV. SID Symposium Digest of Technical Papers, **35**, 760–763 (2004). DOI: 10.1889/1.1825793

[3] Chrzanowski M. M., Zieliński J., Olifierczuk M., Kędzierski J., Nowinowski-Kruszelnicki E.: Photoalignment – An alternative aligning technique for liquid crystal displays. Journal of Achievements in Materials and Manufacturing Engineering, **48**, 7–13 (2011).

[4] Stöhr J., Samant M. G.: Liquid crystal alignment by rubbed polymer surfaces: A microscopic bond orientation model. Journal of Electron Spectroscopy and Related Phenomena, **98–99**, 189–207 (1999). DOI: 10.1016/S0368-2048(98)00286-2

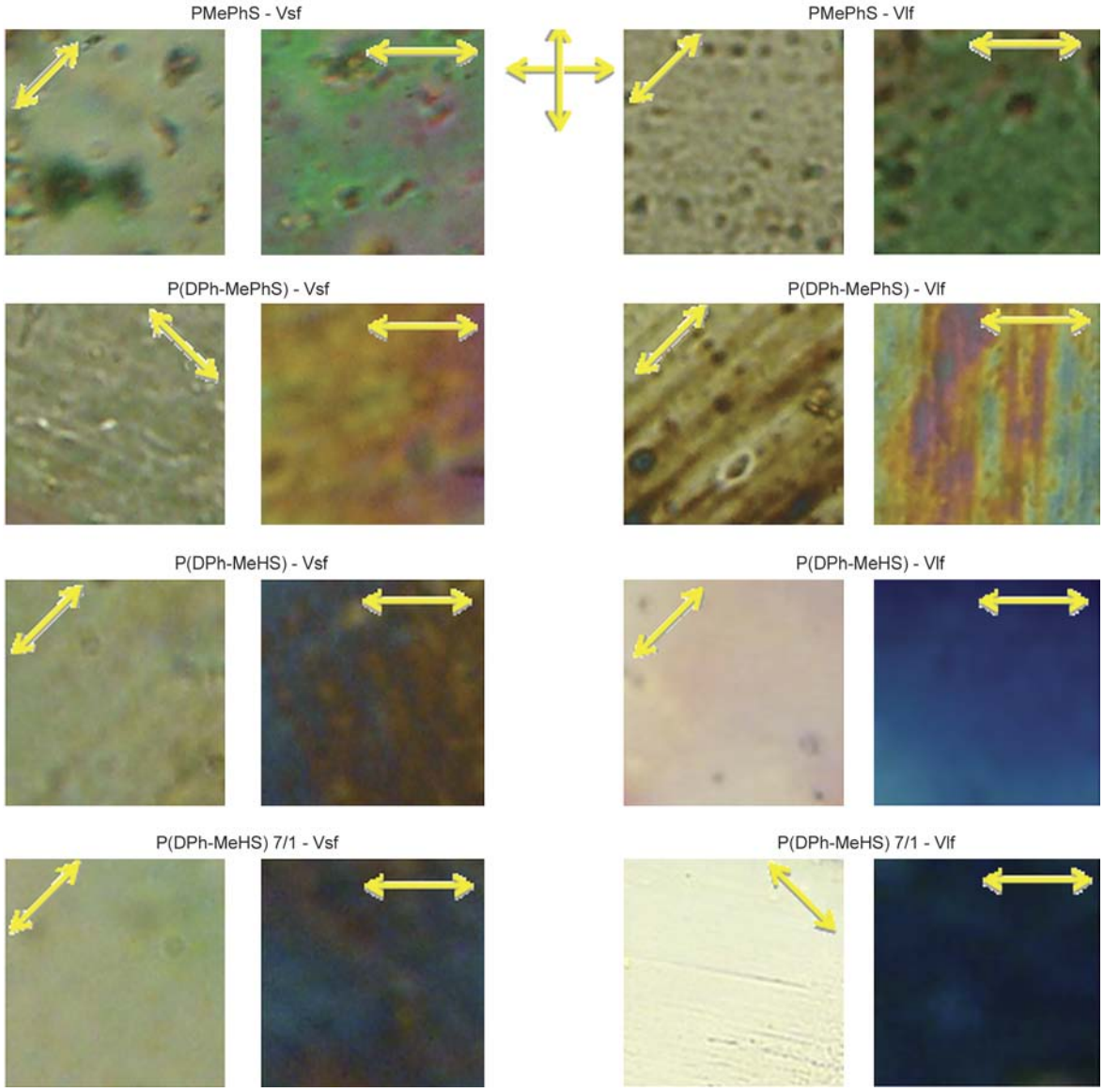

Figure 12. Polarized light images revealing dark and bright states as result of 5CB orientation on rubbed polysilane films with velvet having short (Vsf) and long fibers (Vlf), respectively

[5] Hahm S. G., Lee T. J., Chang T., Jung J. C., Zin W-C., Ree M.: Unusual alignment of liquid crystals on rubbed films of polyimides with fluorenyl side groups. Macromolecules, **39**, 5385–5392 (2006). DOI: 10.1021/ma060956f

[6] Takatoh K., Hasegawa M., Koden M., Itoh N., Hasegawa R., Sakamoto M.: Alignment technologies and applications of liquid crystal devices. Taylor and Francis, London (2005).

[7] Hirosawa I., Koganezawa T., Ishii H., Sakai T.: Effects of annealing on rubbed polyimide surface studied by grazingincidence X-ray diffraction. IEICE Transactions on Electronics, **E92C**, 1376–1381 (2009). DOI: 10.1587/transele.E92.C.1376

[8] Hirosawa I., Sasaki N., Kimura H.: Characterization of molecular orientation of rubbed polyimide film by grazing incidence X-ray scattering. Japanese Journal of Applied Physics, **38**, L583–L585 (1999). DOI: 10.1143/JJAP.38.L583

[9] Chang C-J., Chou R-L., Lin Y-C., Liang B-J., Chen J-J.: Effects of backbone conformation and surface texture of polyimide alignment film on the pretilt angle of liquid crystals. Thin Solid Films, **519**, 5013–5016 (2011). DOI: 10.1016/j.tsf.2011.01.155

[10] Barzic A. I., Rusu R. D., Stoica I., Damaceanu M. D.: Chain flexibility versus molecular entanglement response to rubbing deformation in designing poly(oxadiazole-naphthylimide)s as liquid crystal orientation layers. Journal of Materials Science, **49**, 3080–3098 (2014). DOI: 10.1007/s10853-013-8010-5

[11] Barzic A. I., Stoica I., Hulubei C.: Semi-alicyclic polyimides: Insights into optical properties and morphology patterning approaches for advanced technologies. in 'High performance polymers – Polyimides based – From chemistry to applications' (ed.: Abadie M. J. M.) InTech, Novi Sad, 167–214 (2012). DOI: 10.5772/2834

[12] Barzic A. I., Stoica I., Popovici D., Vlad S., Cozan V., Hulubei C.: An insight on the effect of rubbing textile fiber on morphology of some semi-alicyclic polyimides for liquid crystal orientation. Polymer Bulletin, **70**, 1553–1574 (2013).
DOI: 10.1007/s00289-012-0858-z

[13] Stoica I., Barzic A. I., Hulubei C.: The impact of rubbing fabric type on surface roughness and tribological properties of some semi-alicyclic polyimides evaluated from atomic force measurements. Applied Surface Science, **268**, 442–449 (2013).
DOI: 10.1016/j.apsusc.2012.12.123

[14] Geivandov A. R., Palto S. P.: The influence of ferroelectric polymer alignment layer on electrooptical properties of nematic LC cell. Molecular Crystals and Liquid Crystals, **433**, 155–164 (2005).
DOI: 10.1080/15421400590957143

[15] Negi Y. S., Suzuki Y., Hagiwara T., Kawamura I., Yamamoto N., Mori K., Yamada Y., Kakimoto M., Imai Y.: Surface alignment of ferroelectric liquid crystals using polyimide, polyamide-imide and polyamide layers and their effect on pre-tilt angle. Liquid Crystals, **13**, 153–161 (1993).
DOI: 10.1080/02678299308029061

[16] Kim T. Y., Kim W. J., Lee T. H., Kim J. E., Suh K. S.: Electrical conduction of polyimide films prepared from polyamic acid (PAA) and pre-imidized polyimide (PI) solution. Express Polymer Letters, **1**, 427–432 (2007).
DOI: 10.3144/expresspolymlett.2007.60

[17] Hoogboom J., Rasing T., Rowan A. E., Nolte R. J. M.: LCD alignment layers. Controlling nematic domain properties. Journal of Materials Chemistry, **16**, 1305–1314 (2006).
DOI: 10.1039/B510579J

[18] Da Z. L., Zhang Q. Q., Wu D. M., Yang D. Y., Qiu F. X.: Synthesis, characterization and thermal properties of inorganic-organic hybrid. Express Polymer Letters, **1**, 698–703 (2007).
DOI: 10.3144/expresspolymlett.2007.95

[19] Nešpůrek S., Wang G., Yoshino K.: Polysilanes – Advanced materials for optoelectronics. Journal of Optoelectronics and Advanced Materials, **7**, 223–230 (2005).

[20] Okoshi K., Fujiki M., Watanabe J.: Asymmetrically tilted alignment of rigid-rod helical polysilanes on a rubbed polyimide surface. Langmuir, **28**, 4811–4814 (2012).
DOI: 10.1021/la204789g

[21] Tanigaki N., Mochizuki N., Mizokuro T., Yoshida Y., Yase K.: Orientation patterning of liquid crystals by UV-irradiated polysilane oriented films. Molecular Crystals and Liquid Crystals, **445**, 119–124 (2006).
DOI: 10.1080/15421400500369492

[22] Tanigaki N., Yase N., Kaito A., Ueno K.: Highly oriented films of poly(dimethylsilylene) by friction deposition. Polymer, **36**, 2477–2480 (1995).
DOI: 10.1016/0032-3861(95)97351-F

[23] Tanigaki N., Kyotani H., Wada M., Kaito A., Yoshida Y., Han E-M., Abe K., Yase K.: Oriented thin films of conjugated polymers: Polysilanes and polyphenylenes. Thin Solid Films, **331**, 229–238 (1998).
DOI: 10.1016/S0040-6090(98)00924-9

[24] Tauc J.: Optical properties of solids. Plenum, New York (1969).

[25] Mott N. F., Davis E. A.: Electronic processes in non-crystalline materials. Clarendon, Oxford (1979).

[26] Săcărescu G., Voiculescu N., Marcu M., Săcărescu L., Ardeleanu R., Simionescu M.: Polyhydrosilanes I. Synthesis. Journal of Macromolecular Science Part A: Pure and Applied Chemistry, **34**, 509–516 (1997).
DOI: 10.1080/10601329708014977

[27] Sacarescu L., Siokou A., Sacarescu G., Simionescu M., Mangalagiu I.: Methylhydrosilyl chemostructural effects in polyhydrosilanes. Macromolecules, **41**, 1019–1024 (2008).
DOI: 10.1021/ma071853f

[28] Hamciuc V., Pricop L., Marcu M., Ionescu C., Sacarescu L., Pricop D. S.: Reaction conditions study in linear H-functional polysiloxane synthesis. Journal of Macromolecular Science Part A: Pure and Applied Chemistry, **35**, 1957–1970 (1998).
DOI: 10.1080/10601329808000990

[29] Urbach F.: The long-wavelength edge of photographic sensitivity and of the electronic absorption of solids. Physical Review, **92**, 1324–1326 (1953).
DOI: 10.1103/PhysRev.92.1324

[30] Barzic A. I., Stoica I., Fifere N., Dobromir M., Hulubei C., Dorohoi D. O., Harabagiu V.: Transparency and absorption edges of disiloxane modified copolyimides. Journal of Molecular Structure, **1044**, 206–214 (2013).
DOI: 10.1016/j.molstruc.2012.12.044

[31] Barzic A. I., Stoica I., Fifere N., Vlad C. D., Hulubei C.: Morphological effects on transparency and absorption edges of some semi-alicyclic polyimides. Journal of Polymer Research, **20**, 130–138 (2013).
DOI: 10.1007/s10965-013-0130-8

[32] Jarząbek B., Schab-Balcerzak E., Chamenko T., Sęk D., Cisowski J., Volozhin A.: Optical properties of new aliphatic–aromatic co-polyimides. Journal of Non-Crystalline Solids, **299**, 1057–1061 (2002).
DOI: 10.1016/S0022-3093(01)01130-9

[33] Berreman D. W.: Alignment of liquid crystals by grooved surfaces. Molecular Crystals and Liquid Crystals, **23**, 215–231 (1973).
DOI: 10.1080/15421407308083374

[34] Johannsmann D., Zhou H., Sonderkaer P., Wierenga H., Myrvold B. O., Shen Y. R.: Correlation between surface and bulk orientations of liquid crystals on rubbed polymer surfaces: Odd-even effects of polymer spacer units. Physical Review E, **48**, 1889–1896 (1993).
DOI: 10.1103/PhysRevE.48.1889

[35] Kikuchi H., Logan J. A., Yoon D. Y.: Study of local stress, morphology, and liquid-crystal alignment on buffed polyimide surfaces. Journal of Applied Physics, **79**, 6811–6817 (1996).
DOI: 10.1063/1.361502

eXPRESS Polymer Letters Vol.9, No.5 (2015) 469–479
Available online at www.expresspolymlett.com
DOI: 10.3144/expresspolymlett.2015.44

Synthesis of novel silica-polyimide nanocomposite films using aromatic-amino modified silica nanoparticles: Mechanical, thermal and morphological investigations

R. V. Ghorpade[*], *C. R. Rajan, N. N. Chavan, S. Ponrathnam*

Polymer Science and Engineering Division, CSIR-National Chemical Laboratory, Dr. Homi Bhabha Road, Pune- 411008 India

Received 13 October 2014; accepted in revised form 9 December 2014

Abstract. Silica nanoparticles were modified with aromatic amino groups and modified-silica/polyimide composite films were prepared using them. 3,3′,4,4′-Benzophenone tetracarboxylic dianhydride (BTDA) and 4,4′-oxydianiline (ODA) were used as precursors for polyimide matrix. The structures of the modified nanoparticles and hybrid nanocomposites were identified using Fourier Transform Infrared (FTIR) spectrometry. The hybrid composite films were evaluated for mechanical, thermal and morphological characteristics. Morphological results describe a uniform dispersion of silica particles in the polymer matrix. The thermal stability and mechanical properties of polyimide composite were improved, and the decomposition temperature was increased when the amount of silica nanoparticles was increased.

Keywords: *nanocomposites, nanoparticle modification, hybrid polyimide composites, thermal properties, mechanical properties*

1. Introduction

Polymer–inorganic hybrid nanocomposites are an emerging class of materials that hold significant promise due to their outstanding properties, which usually arise from a combined effect of the properties of their polymeric and inorganic components [1]. Nanoparticles and nanocomposites are used in a wide range of applications comprising of diverse fields, such as medicine, textiles, cosmetics, agriculture, optics, food packaging, optoelectronic devices, semiconductor devices, aerospace, construction and catalysis [2–4]. Polymeric nanocomposites consisting of inorganic nanoparticles and organic polymers represent a new class of materials that exhibit improved performance compared to their microparticle counterparts [4].

Silica nanoparticles are gaining considerable interest for a wide variety of applications in various fields of material science like electronic, chemical, optical and mechanical industries due to their unique and promising physical and chemical properties [5–7]. The surface modification of nanoparticles in order to change their physical and chemical properties has become an area of significant research in industry. However, the applications of silica nanoparticles are largely limited because of their high energetic surface, which causes the silica nanoparticles to be easily agglomerated. However, this problem could be resolved by using surface modification methods [8]. Surface modification of silica nanoparticles has attracted attention because it produces excellent integration and an improved interface between nanoparticles and polymer matrices [9]. Polymer matrices reinforced with modified silica nanoparticles combine the functionalities of polymer matrices, which include low weight and easy formability,

[*]Corresponding author, e-mail: rv.ghorpade@ncl.res.in

with the unique features of the inorganic nanoparticles. However, the nanoparticles have a strong tendency to undergo agglomeration in the polymer matrix, degrading the mechanical properties of the nanocomposites [4, 10, 11]. To improve the dispersion stability of nanoparticles in polymer, it is essential that the particle surface be modified by reactive surface functionalities to generate a strong interaction between monomer precursors and particle surface and repulsion between particles. In order to precisely design desirable surface functionalities, one can select an appropriate surface modification method according to the needs in terms of polymer functional groups and composition.

Also the mechanical properties of these hybrid polymer/nanocomposite materials strongly depend on the dispersion of the reactive sites and on the chemical nature of their environment [12]. This environment mainly consists of the uncovered surface. Therefore, the mode of anchorage of the organic moieties is of prime importance for the characteristics of the final functionalized nanoparticles [13]. Despite the numerous functionalization methods described in literature, only a few allow a precise and easy control of the chemical composition and structure of the surface functionalities of shell. Not all the modification processes offer compatible surface functional groups that can be directly incorporated during polymerization. So, today there is a great challenge to develop alternative methods that provide convenient access to surface functionalized nanoparticles, with the characteristics of the hybrid nanoparticles targeted by the specific property to be achieved.

Aromatic polyimides are important class of thermally stable organic polymers, ranked among the thermally stable polymers. They are widely used in various applications such as high temperature plastics, adhesives, dielectrics, photoresists, nonlinear optical materials and membranes. Additionally, polyimides are used in the fields of aerospace, defense, and optoelectronics; they are also used in liquid crystal alignments, composites, polymer electrolyte fuel cells, fiber optics, etc [14]. The most common technique used to process polyimides is from soluble polyamic acid as a precursor. Films are cast, and then they are thermally dehydrated to produce the final imide form [14, 15].

Even though polyimides are thermally very stable polymers, they can still degrade if exposed to a high temperature for a long period. This exposure can lead to changes in the physical and chemical structure of the materials and affect their thermo-oxidative stability [16]. A technology that has been gaining attention in recent years is the incorporation of appropriate nanoscale components into polyimides as a means of improving their thermal and mechanical properties [17–19]. Polyimide-silica materials offer key properties of both components are, therefore, in great demand for high performance applications [20]. There are many factors affecting the properties of hybrid composites, such as the particle size, size distribution, and filler content. In addition, the particle shape and surface functionalities play an important role in the formation of hybrid composite materials [21]. Especially, the bond strength between inorganic particles and polymer matrix should be improved, which always is influenced by the type of dispersion aid and surface functional groups of nanoparticles [22–24]. Thermodynamic immiscibility between inorganic and organic materials, however, may lead to phase separation of the components [25].

Preparation of polymer–inorganic nanocomposites was reported by *in situ* and *ex situ* generation of nanoparticles [27, 28]. Sol-gel process [29] is known to generate nanoparticles *in situ* in the polymerization process, but it is difficult to ensure full control of the shape, crystallinity, size, size distribution, and surface properties of the nanoparticles during the reaction. Also unreacted reactants and byproducts are the major drawback of this process [27]. While, in *ex situ* process, pre-made and modified nanoparticles are blended with polymer precursors [30], hence, the properties of the nanoparticles can be easily controlled. Therefore *ex situ* synthetic process of modification and blending of nanoparticles is the simplest and most convenient way to prepare polymer nanocomposites. Polyimide nanocomposites with aliphatic amino functionalized SiO_2 nanoparticles were recently reported [28], but the thermal properties like decomposition temperature and T_g deceased with increasing silica content. Therefore the use of suitably surface modified silica nanoparticles is a reasonably good approach for producing fine silica particles uniformly dispersed in the polyimide matrix through polymerization of monomeric precursors with modified silica.

In the present work, simple route was used to modify surface of silica nanoparticle with aromatic amino groups. Polyimide–silica nanocomposites were pre-

pared using 3,3′,4,4′-benzophenone tetracarboxylic dianhydride (BTDA), 4,4′-oxydianiline(ODA) and aromatic amino modified silica nanoparticles by ultrasonic blending followed by thermal imidization. This approach contributes to the novelty in the making of such composite materials. After the surface modification process, the modified silica nanoparticles had better compatibility with polymer matrix and could be well dispersed into the PI matrix in various amounts and the aromatic amino groups on the nanoparticle surface forms covalent bond with the polyimide matrix. Mechanical, thermal and morphological analyses of the composite films were carried out and compared with the film prepared by unmodified silica nanoparticles.

2. Experimental

2.1. Materials

Chemicals of high purity were obtained from various commercial sources, which consisted of 3,3′,4,4′-benzophenone tetracarboxylic dianhydride (BTDA; Aldrich), 4,4′-oxydianiline(ODA; Aldrich), N-methyl-2-pyrrolidone (NMP; Merck), phenyl triethoxysilane (PTEOS; Aldrich). 100 nm silica nanoparticles were obtained from Fiber Optic Center Inc. USA and dried under vacuum at 120°C before use. NMP was purified by distillation under reduced pressure over calcium hydride and stored over 4 Å molecular sieves. Other organic solvents were purified by vacuum distillation. BTDA was dehydrated by drying under a vacuum at 160°C for 24 h. The other reagents were used as received.

2.2. Methods

The FTIR spectra of silica nanoparticles and silica polymide composite were scanned using a Perkin Elmer 599B spectrophotometer (Waltham, MA) between 400 and 4000 cm^{-1} using KBr pellets as medium. XPS measurement was carried out on the APPES system with Mg K radiation (hr = 1253.6 eV). Differential scanning calorimetry was performed on a TA Q100 DSC instrument to determine the glass transition temperatures (T_g) of the copolymers. All samples were run against an aluminium reference in crimped aluminium pans. A temperature range of 40 to 400°C was used to determine the T_g. Two scans were performed on each sample at a heating rate of 10°C/min. The second heating results were used for evaluation of T_g. Thickness of the film specimens was measured by Mitutoyo Micrometer. For each individual specimen, measurements were done at five different points and the average value was taken. The thickness data of the film specimens were used for tensile testing. The tensile test was conducted using a Linkam Tensile Stress Testing System-TST 350. Thermogravimetric analysis (TGA) was performed on STA 6000 TGA model from Perkin Elmer instruments. The samples were heated at a rate of 10°C/min under nitrogen atmosphere in the range of 40 to 900°C. Modified nanosilica and polyimide hybrid composite films were investigated using X-ray diffractometer (Rigaku, Micro Max-007 HF).

2.3. Modification of silica nanoparticles with PTEOS

100 nm silica nanoparticles were dried under reduced pressure at 120°C for 12 h in vacuum oven. Dried silica nanoparticles (10.0 g) were suspended in 200 mL of toluene for 30 min under sonication. Nanosilica-toluene mixture kept under mechanical stirring in three necked reactor under nitrogen atmosphere. 3.0 g of triethylamine was added into the mixture. An excess 3.0 g of phenyl triethoxysilane (PTEOS) was added to a suspension of silica – toluene and stirred for 30 min at room temperature. The mixture was heated at reflux for 24 h at high speed stirring. Finally, the particles were washed free of adsorbed initiator using 5 cycles of centrifugation and re-suspension in toluene, and then volatiles were removed under vacuum.

2.4. Nitration of PTEOS modified nanosilica

Sodium nitrite (2.0 g) was added to 100 mL RB flask containing a mixture of PTOES modified silica nanoparticles (2.0 g), chloroform (20 mL), and acetic acid (3 mL), and the mixture was stirred for 2 hour at room temperature. Acetic acid (2 mL) was then added and the mixture was stirred for a further 18 hours. Nanoparticles were separated by centrifugation and washed with water for several times to remove any unreacted $NaNO_2$ and acetic acid. Finally silica nanoparticles were washed by centrifugation with ethanol and dried under vacuum.

2.5. Reduction of nitro group on modified nanosilica

4.0 g of aromatic-nitro modified silica nanoparticles were dispersed in 50 mL of ethanol and sonicated for 30 min. 4.0 g of $SnCl_2 \cdot 2H_2O$ dissolved in

25 mL of ethanol and added to silica suspension with mechanical stirring at 30°C. The reaction mixture was kept under stirring for 4 h at 30°C. The pH was made slightly basic (pH 8) by addition of 5% aqueous sodium bicarbonate and the resulting basic mixture kept one hour under stirring. Nanoparticles were washed with water for several times to remove unreacted components followed by washing with ethanol and dried under reduced pressure. These modified nanoparticles were characterized by IR, TGA and XPS.

2.6. Determination of surface amino groups

A typical non-aqueous titration method was employed to detect the coverage density of amino group on the surface of silica nanoparticles by using HCl ethanol standard solution. [31] Thymol-blue was used as indicator in the titration, where the referred HCl was used to quantify the amount of amino groups on the surface of modified nanosilica dispersed in the ethanol. The concentration of surface $–NH_2$ groups were determined which is an average of more than 4 times by this titration process.

2.7. Polyimide/ modified silica composite

Polyimide films with various amounts of modified silica nanoparticles were prepared. First, the desired amount of modified silica and NMP were mixed and sonicated for 15 min (Solution A). Second, the diamine (ODA) was dissolved in NMP and stirred for 15 min (Solution B). Then, the solutions A and B were mixed while stirring was continued for 1 h. Third, the dianhydride (BTDA) was dissolved in Solution (A+B) with constant stirring. The mixture was stirred for 24 h at 30°C. The nanocomposite films were prepared by casting from the viscous poly(amic acid)/modified silica solution on a glass plate using a doctor's knife. The resultant films were dried in an oven and subsequently imidized at a high temperature in air. An imidization program, such as heating from room temperature to 80°C in 30 min, heating at 80°C for 2 h, heating from 80 to 200°C in 5 h, heating from 200 to 300°C in 2 h, heating at 300°C for 45 min, and then cooling to room temperature, was employed. Table 1 presents the amount of dianhydride, diamine, solvent NMP, modified silica nanoparticles with film thickness of each sample. Polyimide film with 4 wt% of unmodified silica nanoparticles was prepared as per procedure mentioned.

3. Results and discussion

PTEOS was used to modify surface of nanosilica. Aromatic amino functionalized silica nanoparticles were prepared by nitration followed by reduction of PTEOS modified silica nanoparticles as depicted in Figure 1. A typical titration method was employed to detect the surface amino group on the on the modified nanosilica. The density of $–NH_2$ group on the nanoparticle surface is about 180.7 $\mu mol \cdot g^{-1}$. Also FTIR spectral analysis of nanoparticles confirms modification of silica nanoparticles with aromatic amino groups. Figure 2 shows the FT-IR spectrum of the samples, SiO_2 (curve a), PTEOS modified SiO_2 nanoparticles (curve b), SiO_2@Ar-NO_2 (curve c) and SiO_2@Ar-NH_2 (curve d). In Figure 2 curve a the spectra displayed the characteristic band at 1103 cm^{-1} of the Si–O–Si unit and symmetric

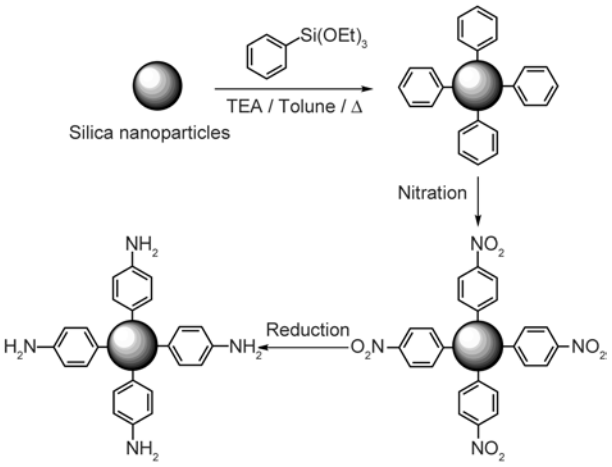

Figure 1. Synthetic scheme for modification of silica nanoparticles

Table 1. Modified silica/ polyimide hybrid film compositions and thickness

Polymer code	BTDA [g]	ODA [g]	NMP (70 wt% wrt. of solids) [g]	Modified silica nanoparticles [wt% / g]	Film thickness ±0.2 mm [mm]
PI	2.0	1.24	7.56	0 / 0	0.162
PIMS-2	2.0	1.24	7.71	2.0 / 0.065	0.168
PIMS-4	2.0	1.24	7.86	4.0 / 0.130	0.170
PIMS-6	2.0	1.24	8.01	6.0 / 0.194	0.165
PIMS-8	2.0	1.24	8.16	8.0 / 0.259	0.169

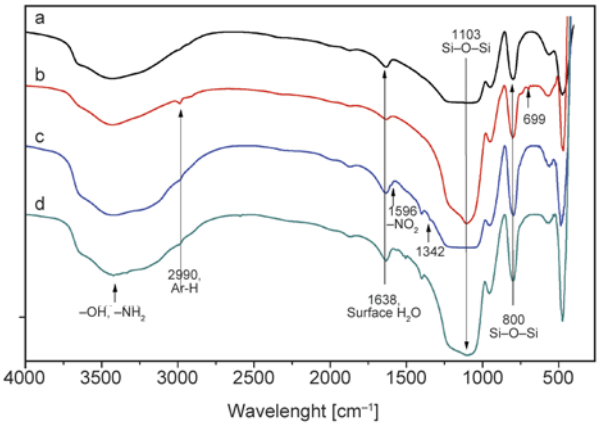

Figure 2. FT-IR spectrum of SiO_2 (a), SiO_2@Ar (b), SiO_2@Ar-NO_2 (c) and SiO_2@Ar-NH_2 (d)

stretching at 800 cm^{-1}.The broad absorption from 3200 to 3300 cm^{-1} was assigned to the Si–OH linkage. The band at 1638 cm^{-1} was the bending vibrations of water molecules adsorbed on the surface of the SiO_2. Figure 2 curve b displayed the characteristic features of PTEOS modified SiO_2 nanoparticles. Compared with Figure 2 curve a, the weak C–H stretching vibration for Ar-H of PTEOS was observed at 2990 cm^{-1}, and the peaks at 699 and 738 cm^{-1} were due to Si-Ph vibrations. In Figure 2 curve c bands at 1596 and 1342 cm^{-1} are due to vibrations of nitro groups, indicate nitration of surface aromatic rings. While in Figure 2 curve d disappearance bands at 1596 and 1342 cm^{-1} and presence of wider band consisted of the asymmetric stretching vibration for N–H bonds and the Si–OH of SiO_2 depicted the reduction of SiO_2@Ar-NO_2 to SiO_2@Ar-NH_2.

Modification of silica nanoparticles was also followed by evaluating chemical states of nitrogen using XPS analysis. Figure 3 curve a and curve b shows, the N 1 s spectra for SiO_2@Ar-NO_2 and SiO_2@Ar-NH_2 nanoparticles respectively. In Figure 3 curve a peak at 407.1 eV and in Figure 3 curve b peak at 399.6 eV attributing to binding energy of –NO_2 and –NH_2 groups, respectively. Shifting of chemical states of nitrogen confirms that surface –NO_2 groups from silica nanoparticles converted into –NH_2 groups.

The contact angle measurement was performed to obtain the hydrophilicity/hydrophobicity behavior of nanoparticle surface. The sessile-drop method in air was used to quantify wetting ability, an indicator of hydrophilicity. The contact angle reading taken is the angle between the bordering surfaces, in this case formed between silica monolayer and the water surface. Figure 4 indicates that the water contact angle of aromatic modified silica nanoparticles is higher due to surface hydrophobicity, while the water contact angle decreases on nitration and further decreased on reduction of surface nitro groups to amino groups.

In this study, ODA and BTDA were used to prepare PI matrix. Thin films were obtained from neat polyamic acid as well as its composites with various proportions of modified silica (Figure 5). To prevent aggregation and get uniform dispersion of the nanoparticles, ultrasonic blending was performed on the reaction mixture. The details of the process of silica/PI composite films are shown in Figure 6. The FT-IR spectra of neat PI and hybrid composite films are shown in Figure 7. The typical characteristic bands of PI polymer matrix were found. In these spectra, the bands at 1771 and 1710 cm^{-1} were associated with the imide carbonyl band. In the IR spectra of PIMS-8 additional band at 1104 cm^{-1} were found due to characteristic vibrations of Si–O linkage.

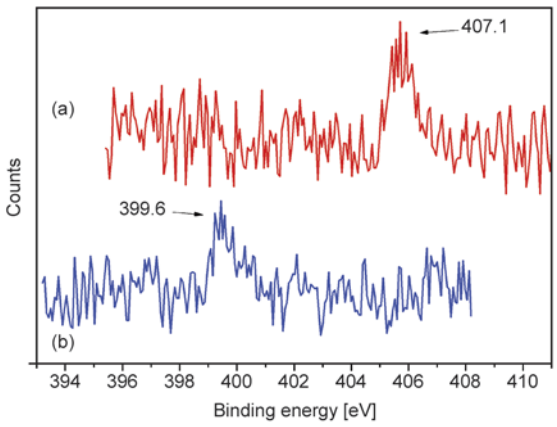

Figure 3. N 1 s XPS spectra of SiO_2@Ar-NO_2 (a) and SiO_2@Ar-NH_2 (b)

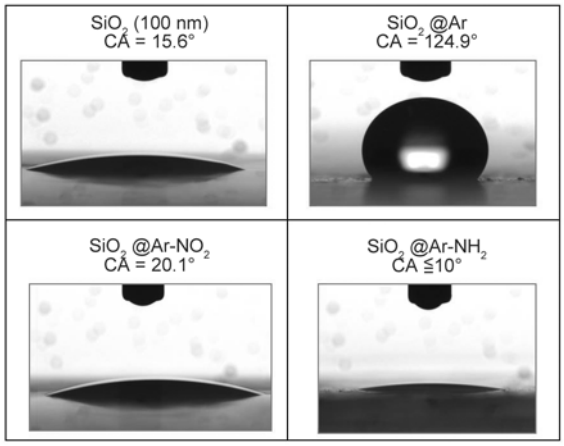

Figure 4. Variation in contact angle during modification of silica nanoparticles

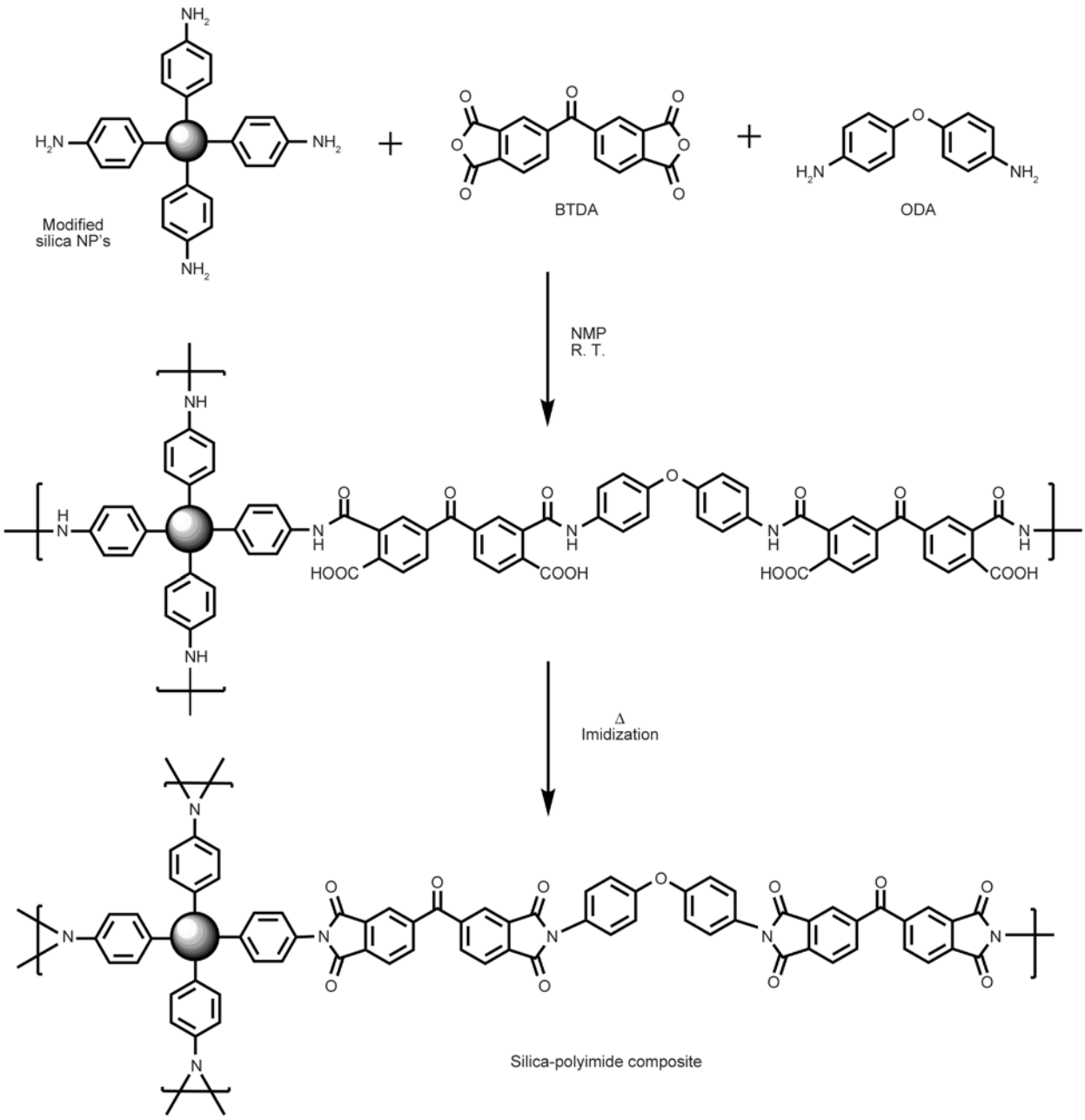

Figure 5. Synthetic scheme of modified silica/polyimide composites

The morphology of the modified silica nanoparticles and hybrid films has been studied using scanning electron microscopy (SEM). After modification with aromatic amino group silica particles remains dispersed and spherical in nature (Figure 8b). The micrographs of the composites containing 4 wt% modified and unmodified silica in the matrix are shown in Figure 8c and Figure 8d respectively. Composite films have a very homogeneous distribution with no agglomeration of silica in any region across the films. The amino groups present on the surface of nanosilica reacts with polyimide matrix forming covalent bonds and do not allow the agglomeration of silica particles. Such homogeneous distribution of nanoparticles demonstrates better compatibility between modified silica nanoparticles and the polyimide in the composite films. This has resulted in improved strength of the composite films for present system.

To reveal the distribution of silica nanoparticles in the polyimide matrix, transmission electron microscopy (TEM) was performed. The samples for the TEM study were taken from a microtomed section of the polyimide/modified silica nanocomposites. Figure 9 shows TEM micrographs for the polyimide nanocomposites incorporated with 4 wt% modified silica nanoparticles (Figure 9a) and 4 wt% unmodified silica nanoparticles (Figure 9b). The light

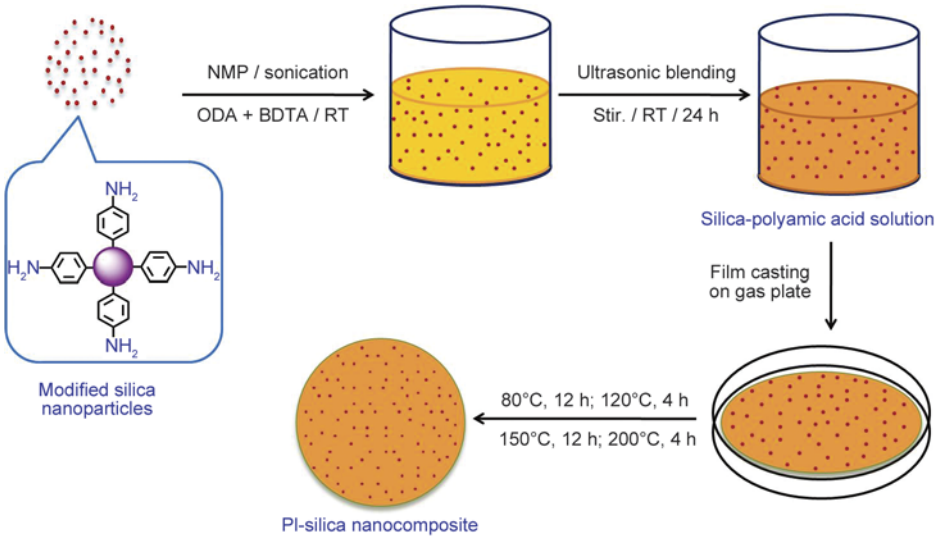

Figure 6. Details of the synthetic process for silica/PI composite

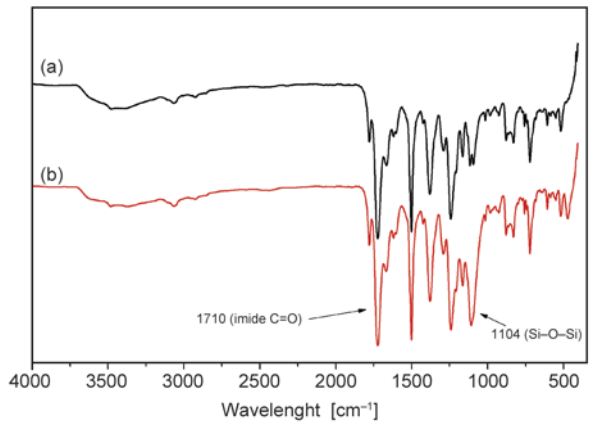

Figure 7. The FT-IR spectra of neat PI (a) and hybrid PI (b) composite films

regions represent the Polyimide matrix, and the gray, dark spots correspond to the SiO_2 nanoparticles. The distribution of silica nanoparticles in Figure 9a is more uniform than that in Figure 9b. It can be conclude that aromatic amino modified silica nanoparticles distribute more uniformly in the polyimide matrix than the unmodified silica nanoparticles. It is thought that the modification plays an important role in the uniformity of the silica distribution.

Stress–strain curves of neat polyimide, nanosilica/ polyimide films and modified nanosilica/polyimide films were recorded for evaluation of strain-to-break properties. Dog bone shaped specimens of the neat polyimide and polyimide/modified SiO_2 nanocomposites with thickness of around 0.2 micrometer and width of 2.7 mm at the gauge section were used for the tensile test. The specimen was loaded at a strain rate of 0.1 mm/min until the failure happened. The influence of the silica content on the tensile strength is shown in Figure 10. The tensile strength at yield point for neat polyimide films was 82 MPa. These values of yield stress for the composite films increased (122 MPa) with an increase in the modified silica content up to 8 wt%. The variation of tensile strength at yield point and at break point as a function of modified silica content is illustrated in Table 2. The elongation at break decreased slightly with increasing silica content. Ultimate strength and % elongation of modified silica/polyimide composite film (PIMS-4) improved compared with unmodified silica/ polyimide composite film (PIAS-4). This may be caused by the fact that the modified nanosilica is much easier to be dispersed homogeneously in the solution and covalently bonded to the polyimide matrix.

Table 2. Mechanical properties of modified nanosilica/ polyimide composite films

Polymer code	Ultimate tensile stress [MPa]	Strain to yield point [%]
PI	82.08	8.93
PIMS-2	98.72	8.80
PIMS-4	110.63	8.47
PIMS-6	122.33	7.47
PIMS-8	130.42	7.00
PIAS-4	104.06	7.00

The DSC curves presented in Figure 11 shows the evaluation of the glass transition temperatures of nanosilica/polyimide composites. The glass transition temperature of the nanocomposites gradually increased with increase in modified silica content in the polyimide matrix. Because of the surface modification of nanoparticles, the interface between the polymer and the nanoparticle can change and affect

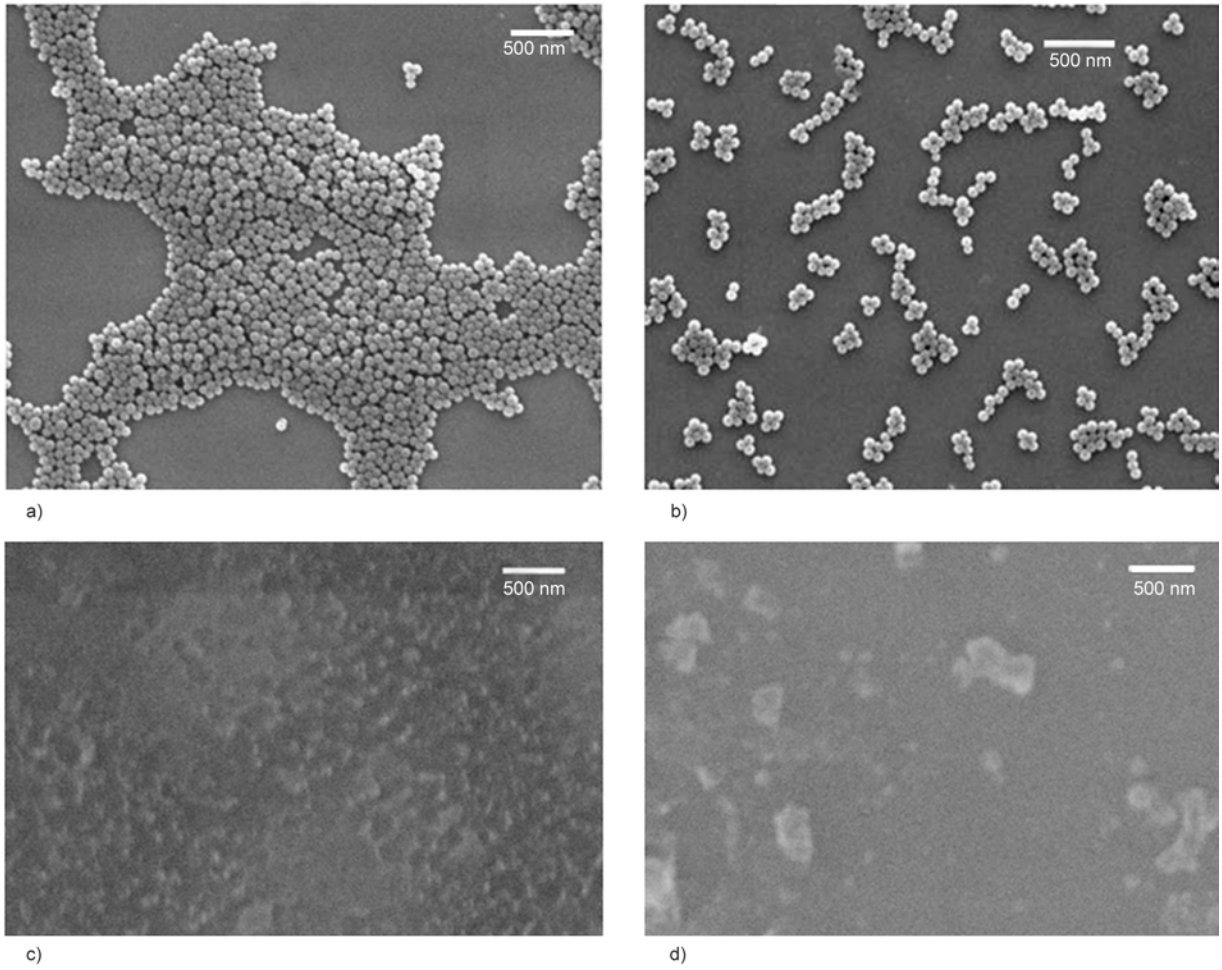

Figure 8. SEM images of silica (a), modified silic (b) modified silica/polyimide (c) and unmodified silica/polyimide (d) composite films

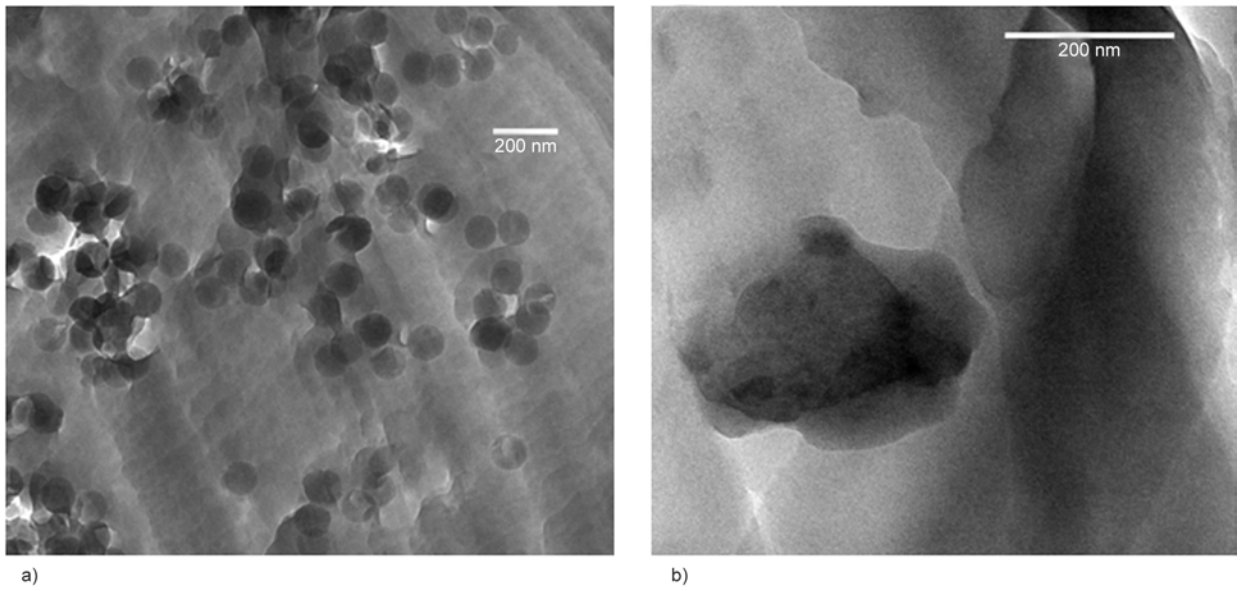

Figure 9. TEM of modified (a) and unmodified (b) silica/polyimide composite films

the thermal properties of the nanocomposites. In this case aromatic amino groups on the nanoparticle surfaces form covalent bonds with polyimide matix and increase the rigidity in the polymer. As a result T_g increased from 282 to 288°C with the SiO_2 content increase. Such improvement in T_g is not observed in case of unmodified silica/PI composite.

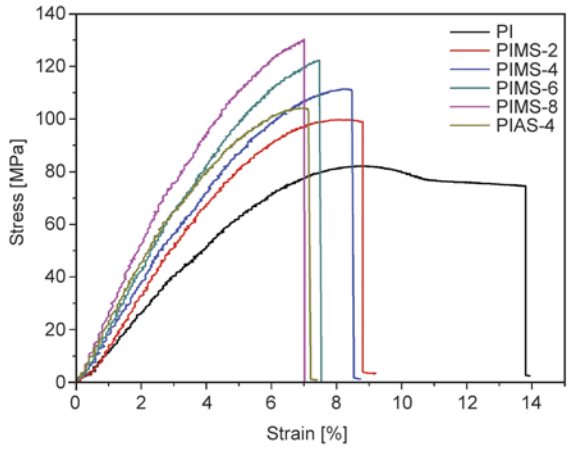

Figure 10. Mechanical tensile testing: stress/strain curves for hybrid polyimide composite films

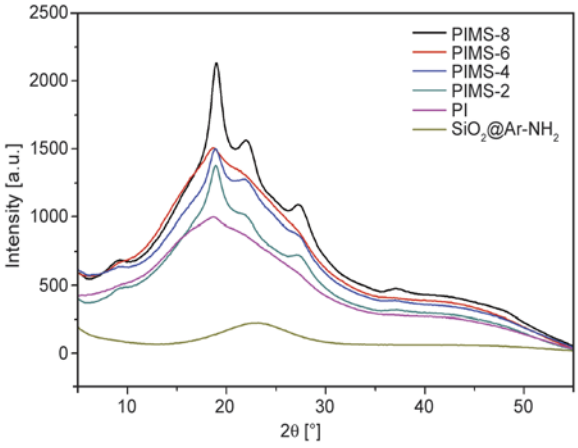

Figure 13. XRD patterns of the modified SiO_2 particles and polyimide/SiO_2 composite films

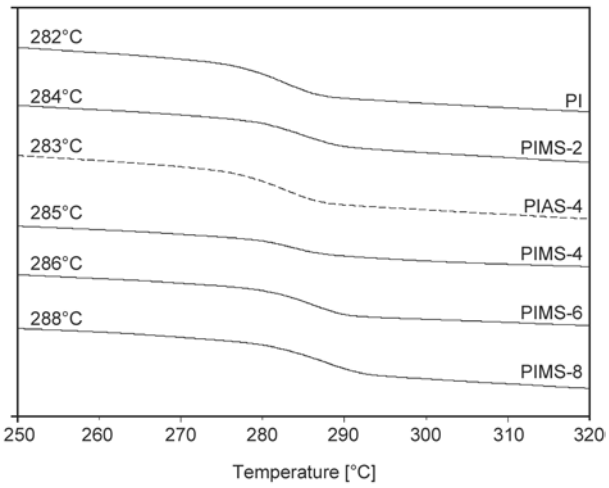

Figure 11. DSC thermograms for silica/ polyimide composite films

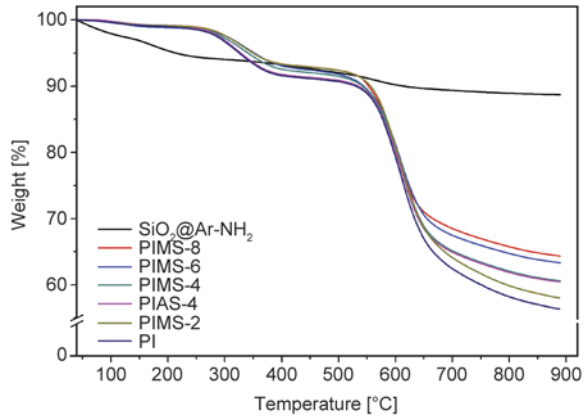

Figure 12. Thermogravimetric analysis of modified silica and hybrid polyimide composite films

The thermal stability of the modified nanosilica/ polyimide composite films was studied by thermogravimetric analysis (TGA). TGA plots of PAI modified nanosilica/polyimide composites with the different amounts of modified silica nanoparticles are shown in Figure 12. The amount of modified silica nanoparticles to polyimide matrix was changed from 0 to 8 wt%. A weight loss is observed above 150°C on all the TGA plots, which corresponds to the loss of water. Weight loss observed at about 250~350°C is due to the trapped solvent as well contribution from imidization arising from surface groups. When the temperature was raised to 500°C, the polyimide matrix began to decompose and the decomposition temperature became higher when the modified silica nanoparticles were added into the polyimide matrix. At the same temperature, all the curves of the composites indicated that the weight loss of the composites was less than that of the pure polyimide matrix. It is worth pointing out that the thermal stability of polyimide was enhanced with the increasing modified silica contents. Also comparison of thermograms of PIMS-4 and PIAS-4 depicted that, at the initial stage of decomposition, thermal stability of PIMS-4 is higher than PIAS-4, which is again proof for covalent bonding between surface functional amino groups on silica with PI matrix.

The prepared composite films were also characterized by XRD. Figure 13 shows the XRD patterns of the modified SiO_2 particles and polyimide/SiO_2 composite films with various contents of modified SiO_2. As can be clearly seen in the Figure, peak patterns in the diffractograms of the PI hybrid films reveal semi-crystalline structure polymers. The result indicated that modified nano-SiO_2 in polyimide could improve the crystallization behavior of the polymer matrix.

4. Conclusions

The aromatic amino modified silica/PI inorganic/organic nanocomposite films were prepared by the simple ultrasonic blending, after the silica nanoparticles were modified by aromatic amino groups on surface. In the micrographs of composite films, the modified silica nanoparticles were found to be well dispersed in the PI polymer matrix. The silica nanoparticles were still monodispersed without any agglomerations when the amount of silica nanoparticles to PI reached 8 wt%. The thermal stability of PI improved, and the decomposition temperature was increased with increasing amount of modified nanosilica in hybrid films. The optimum tensile strength was achieved when appropriate amounts of the modified nanosilica used. Tensile measurements indicate that modulus as well as stress at break point improved while elongation at break decreased for the hybrid materials. The shift in T_g values suggests the presence of interactions between the two phases. The morphological investigations reveal a uniform dispersion of silica particles in the polyimide matrix. In this system, the high thermal stability and mechanical strength showed that these modified silica/PI nanocomposite films can be widely used in the high performance polymer applications.

Acknowledgements

Funding from Department of Science and Technology, Govt. of India (Grant No. SR/S3/CE/0014/2010) is gratefully acknowledged.

References

[1] Beija M., Marty J-D., Destarac M.: RAFT/MADIX polymers for the preparation of polymer/inorganic nanohybrids. Progress in Polymer Science, **36**, 845–886 (2011).
DOI: 10.1016/j.progpolymsci.2011.01.002

[2] Trindade T., da Silva D. A.: Nanocomposite particles for bio-applications: Materials and bio-interfaces. Pan Sanford Publishing, Singapore (2011).

[3] Mahfuzn H., Dhanak V.: Nanoparticle reinforced composites for structural applications. Imperial College Press, London (2010).

[4] Kango S., Kalia S., Celli A., Njuguna J., Habibi Y., Kumar R.: Surface modification of inorganic nanoparticles for development of organic–inorganic nanocomposites – A review. Progress in Polymer Science, **38**, 1232–1261(2013).
DOI: 10.1016/j.progpolymsci.2013.02.003

[5] O'Farrell N., Houlton A., Horrocks B.: Silicon nanoparticles: Applications in cell biology and medicine. International Journal of Nanomedicine, **1**, 451–472 (2006).
DOI: 10.2147/nano.2006.1.4.451

[6] Tang L., Cheng J.: Nonporous silica nanoparticles for nanomedicine application. Nanotoday, **8**, 290–312 (2013).
DOI: 10.1016/j.nantod.2013.04.007

[7] Taylor R., Coulombe S., Otanicar T., Phelan P., Gunawan A., Lv W., Rosengarten G., Prasher R., Tyagi H.: Small particles, big impacts: A review of the diverse applications of nanofluids. Journal of Applied Physics, **113**, 011301/1–011301/19 (2013).
DOI: 10.1063/1.4754271

[8] Hu D., Xu Z-L., Chen C.: Polypiperazine-amide nanofiltration membrane containing silica nanoparticles prepared by interfacial polymerization. Desalination, **301**, 75–81 (2012).
DOI: 10.1016/j.desal.2012.06.015

[9] Li S., Lin M., Toprak M. S., Kim D. K., Muhammed M.: Nanocomposites of polymer and inorganic nanoparticles for optical and magnetic applications. Nano Reviews, **1**, 5214/1–5214/19 (2010).
DOI: 10.3402/nano.v1i0.5214

[10] Yang H., Zhang Q., Guo M., Wang C., Du N., Fu Q.: Study on the phase structures and toughening mechanism in PP/EPDM/SiO_2 ternary composites. Polymer, **47**, 2106–2115 (2006).
DOI: 10.1016/j.polymer.2006.01.076

[11] Kruenate J., Tongpool R., Panyathanmaporn T., Kongrat P.: Optical and mechanical properties of polypropylene modified by metal oxides. Surface and Interface Analysis, **36**, 1044–1047 (2004).
DOI: 10.1002/sia.1833

[12] Hanemann T., Szabó D. V.: Polymer-nanoparticle composites: From synthesis to modern applications. Materials, **3**, 3468–3517 (2010).
DOI: 10.3390/ma3063468

[13] Sutra P., Fajula F., Brunel D., Lentz P., Daelen G., Nagy J. B.: ^{29}Si and ^{13}C MAS-NMR characterization of surface modification of micelle-templated silicas during the grafting of organic moieties and end-capping. Colloids and Surfaces A: Physicochemical and Engineering Aspects, **158**, 21–27 (1999).
DOI: 10.1016/S0927-7757(99)00126-0

[14] Liaw D-J., Wang K-L., Huang Y-C., Lee K-R., Lai J-Y., Ha C-S.: Advanced polyimide materials: Syntheses, physical properties and applications. Progress in Polymer Science, **37**, 907–974 (2012).
DOI: 10.1016/j.progpolymsci.2012.02.005

[15] St. Clair A. K., St. Clair T. L.: Soluble aromatic polyimides for film and coating applications. in 'Polymers for high technology' (eds.: Bowden M. J., Turne S. R.) American Chemical Society, Washington, 437–444 (1987).
DOI: 10.1021/bk-1987-0346.ch037

[16] Cella J., Ghosh M., Mittal K.: Polyimides: Fundamentals and applications. Marcel Dekker, New York (1996).
[17] Kickelbick G.: Concepts for the incorporation of inorganic building blocks into organic polymers on a nanoscale. Progress in Polymer Science, **28**, 83–114 (2003). DOI: 10.1016/S0079-6700(02)00019-9
[18] Bershtein V. A., Egorova L. M., Yakushev P. N., Pissis P., Sysel P., Brozova L.: Molecular dynamics in nanostructured polyimide–silica hybrid materials and their thermal stability. Journal of Polymer Science Part B: Polymer Physics, **40**, 1056–1069 (2002). DOI: 10.1002/polb.10162
[19] Judeinstein P., Sanchez C.: Hybrid organic–inorganic materials: A land of multidisciplinarity. Journal of Materials Chemistry, **6**, 511–525 (1996). DOI: 10.1039/JM9960600511
[20] Khalil M., Saeed S., Ahmad Z.: Mechanical and thermal properties of polyimide/silica hybrids with imide-modified silica network structures. Journal of Applied Polymer Science, **107**, 1257–1268 (2008). DOI: 10.1002/app.27149
[21] Ma X., Lee N-H., Oh H-J., Hwang J-S., Kim S-J.: Preparation and characterization of silica/polyamide-imide nanocomposite thin films. Nanoscale Research Letters, **5**, 1846–1851 (2010). DOI: 10.1007/s11671-010-9726-7
[22] Hosseini S., Li Y., Chung T-S., Liu Y.: Enhanced gas separation performance of nanocomposite membranes using MgO nanoparticles. Journal of Membrane Science, **302**, 207–217 (2007). DOI: 10.1016/j.memsci.2007.06.062
[23] Castellano M., Conzattia L., Costa G., Falqui L., Turturro A., Valenti B., Negroni F.: Surface modification of silica: 1. Thermodynamic aspects and effect on elastomer reinforcement. Polymer, **46**, 695–703 (2005). DOI: 10.1016/j.polymer.2004.11.010
[24] Alexandre M., Dubois P.: Polymer-layered silicate nanocomposites: Preparation, properties and uses of a new class of materials. Materials Science and Engineering R: Reports, **28**, 1–63 (2000). DOI: 10.1016/S0927-796X(00)00012-7
[25] Khalil M.: Polyimide/silica hybrids using imide-modified silica network structures. PhD Thesis, Pakistan Institute of Engineering and Applied Sciences, Islamabad (2009).
[26] Lü C., Yang B.: High refractive index organic–inorganic nanocomposites: Design, synthesis and application. Journal of Materials Chemistry, **19**, 2884–2901 (2009). DOI: 10.1039/b816254a
[28] Kim Y-J., Kim J-H., Ha S-W., Kwon D., Lee J-K.: Polyimide nanocomposites with functionalized SiO_2 nanoparticles: Enhanced processability, thermal and mechanical properties. RSC Advances, **4**, 43371–43377 (2014). DOI: 10.1039/c4ra04952g
[29] Schottner G.: Hybrid sol–gel-derived polymers: Applications of multifunctional materials. Chemistry of Materials, **13**, 3422–3435 (2001). DOI: 10.1021/cm011060m
[30] Barbey R., Lavanant L., Paripovic D., Schüwer N., Sugnaux C., Tugulu S., Klok H-A.: Polymer brushes via surface-initiated controlled radical polymerization: Synthesis, characterization, properties, and applications. Chemical Reviews, **109**, 5437–5527 (2009). DOI: 10.1021/cr900045a
[31] Hu Y., Zhang Y., Tang Y.: One-step hydrothermal synthesis of surface organosilanized nanozeolite under microwave irradiation. Chemical Communications, **46**, 3875–3877 (2010). DOI: 10.1039/C002551H

eXPRESS Polymer Letters Vol.9, No.5 (2015) 480–488
Available online at www.expresspolymlett.com
DOI: 10.3144/expresspolymlett.2015.45

Specimen gripping effects in composites fatigue testing – Concerns from initial investigation

P. B. S. Bailey[1*], *A. D. Lafferty*[2]

[1]Instron Materials Testing, Coronation Road, HP12 3SY High Wycombe, United Kingdom
[2]Department of Materials Science and Engineering, University of Sheffield, Broad Lane, Sheffield, United Kingdom

Received 14 August 2014; accepted in revised form 10 December 2014

Abstract. This paper presents the findings of an initial investigation into effects of end tabs and gripping force on specimens for fatigue testing of structural composites. Live measurement of specimen compliance comparing extensometer measurements with grip displacement showed the impact of gripping on the dynamic behavior of the specimen. Use of thermal imaging enabled assessment of how load is introduced and carried along the specimen.
The effect of grip pressure and comparative merits of popular solutions are examined in the context of fatigue testing of composites. Although for static tests these potential issues have been investigated extensively throughout the history of composites research, interest has only recently fallen upon their effects on dynamic loading. Data collected show that the gripping pressure at the ends of the specimen can affect results more significantly than may be anticipated. These early results suggest that solutions which are well established for quasi-static testing may cause problems in cyclic tests.

Keywords: *polymer composites, fracture and fatigue, material testing, thermography, stress concentration*

1. Introduction

1.1. Background

Having regularly received enquiries regarding appropriate gripping forces for composite test coupons, and regarding specimen failures not only at the jaw face, but within the tabbed and gripped section, the authors sought to clarify the origins of these problems. The results of this initial investigation were considered of significant concern to the composites testing community, so are published within this paper while a wider investigation is ongoing.
Instron (Dynamic Systems) noticed that a rise in commercial demand for composites fatigue data started in the mid 2000's and this has continued to grow unabated since then. This was originally driven by the wind turbine industry, where structures experience significant cyclic strain over a long life cycle. By comparison, academic research interest in composites fatigue was particularly strong during the 1980s through into the mid-90s, along with all aspects of mechanical characterization of composites. Although numbers of publications remained consistent ever since, the topic seemed to become a less popular research and conference topic until around 2010, since when there has been a rapid increase in activity, primarily driven by the aerospace and automotive industries.
It has long been known and demonstrated that gripping methods can significantly affect both the value and the consistency of results in mechanical testing of composites [1, 2] and certain test practices have become commonly accepted for quasi-static tests. Nonetheless, it is interesting to note that ASTM D3039 for tensile testing of composites remarks that 'Design of mechanical test coupons, especially those using end tabs, remains to a large extent an art rather

*Corresponding author, e-mail: peter_bailey@instron.com

than a science, with no industry consensus on how to approach the engineering of the gripping interface' [3]. With growing drive to understand the dynamic behavior of composites [4, 5], an increasing number of experimentalists are finding it necessary to revisit their previous methodologies for specimen preparation.

1.2. Specimen and gripping designs

Straight sided tensile specimens with composite end tabs are now the accepted basic standard for tensile testing of composites [3, 4]. Unfortunately, in a majority of scenarios, where specimens comprise a large amount of on-axis reinforcement, these typically fail at, or only just beyond, the end of the tab [1, 4, 7]. Qualitatively, the analyst knows that this will be the region of highest constraint, and therefore the highest stress concentration, therefore physics dictates that the specimen must fail in that region, unless there is some other, more significant stress raiser or defect. This has been demonstrated quite elegantly, for a variety of configurations, using finite element analysis [8] with some straightforward mechanical tests provided to confirm the predictions. A number of workers examined tapered end-tabs [1, 9, 10] but it appears that results varied from no noticeable difference in failure, through to complete success in establishing failure away from the grips. Whatsoever the efficacy of this technique, tapered tabs are now suggested in international standards [3, 6], but anecdotally, many laboratory operators look on them unfavourably due to the even more laborious preparation required. Early recommendations [1, 11] proposed a variety of tabs including different configurations of fibre reinforced tab material, but also compliant abrasive pads, and aluminium sheet. Only glass fibre reinforced polymer matrix tabs have been carried forward to current international standards, although some researchers still use aluminium tabs and consider them easier and more reliable to prepare.

Several researchers experimented with a gently radiused gauge section, with the goal of forcing failure into a region of known and consistent stress state (away from the grips) as is well established for metals and plastics testing. Some work is published in open literature [12–14], but the authors have also been privileged to be shown similar results by industrial partners who have undertaken similar which remains unpublished. In certain respects, the published work shows a basic level of success, in terms of generating failure within the designated gauge section. However, this does not appear to significantly improve repeatability; it is unclear whether the dominant factor in variability is therefore related to the material or to the specimen preparation. More importantly, a non-critical failure is observed in many tests presented; prior to complete tensile rupture, the specimens develop a shear failure, parallel to the tensile axis, aligned with the edges of the narrowest point of the gauge section. This is particularly concerning for fatigue analyses, where considerable insight may be obtained by calculating the dynamic behavior of the specimen (for example stiffness, modulus, loss tangent, cyclic work done); clearly if the geometry of the load carrying section of the specimen changes, then any such calculations will show a change in output, but will no longer give a comparable measure of the material performance. This might be circumvented by use of strain gauges bonded directly to the specimen, but this raises the risk of not measuring a sufficiently large surface area to be representative, especially with commercial demand for use of large fibre tows and woven reinforcements.

By comparison, the use of open-hole specimens for fatigue does appear to reliably force failure into a defined location, and although this was demonstrated some time ago [15, 16], it was not developed into an international standard until 2011 [17] and is as yet only used by a small number of workers. Early work on fatigue damage in composites also examined the possibility of using on-axis uni-directionally reinforced material with an elongate, transverse, open hole. Growth of the longitudinal fractures propagating from the edges of the hole (as seen from the edges of the radii on dumbbell specimens discussed above) was evaluated, with some success, but the concept does not appear to have been advanced beyond the original work by Spearing and Beaumont [18].

1.3. Clamping pressure

Historically, mechanical testing practitioners have often used a 'rule of thumb' that the gripping force on the ends of a typical specimen should be approximately 10 to 15% larger than the maximum axial test load to be applied. Although at present the authors cannot identify the origins of this guideline, it seems highly probable that it originates in testing of metals coupons, where specimens have more compliant

surfaces making them easier to indent and grip. Furthermore a majority of tensile testing on metals and polymers utilizes wasted specimens where the gripped section is wider than the gauge length. It is the authors' opinion that this level of clamping pressure is usually inadequate for typical, parallel sided specimens, of structural composites.

2. Materials and experimental pocedure

2.1. Specimen preparation

Tests were conducted on E-glass fibre reinforced epoxy resin sheet, prepared by wet lay-up and vacuum consolidation.

Industrial grade, low temperature curing epoxy resin was used, with fibre in the form of E-glass 280 gsm non-crimp fabric. All specimens were produced in one batch, using the same batches of raw materials. The raw materials used in this initial work were generic industrial products, as supplied by East Coast Fibre Supplies, who do not offer further certification of composition or mechanical performance.

Material was produced by wet laying 6 plies of non-crimp fabric between polyamide peel-ply release film, on a polished steel caul plate, then vacuum consolidating at better than 0.95 bar until gelled. The consolidated material was moved to an oven (still on caul plate within bag and under vacuum) for final cure at 60°C for 4 hours.

Specimens were prepared in accordance with ISO 257 [6], cut by diamond wheel, with parallel gauge section of 25 by 150 mm. The 50 mm long gripped section was adjusted for comparison between: tabs of cross-plied, glass fibre reinforced epoxy, 2 mm thick [6, 11]; tabs of aluminium sheet, 2 mm thick [11]; no bonded tab [1].

Where used, the adhesive was the same composition and subject to the same cure as the matrix material. Bonded surfaces were thoroughly solvent washed with acetone, then abraded, then re-washed and allowed to dry, prior to bonding. Composite surfaces were abraded using bonded abrasive paper; aluminium tabs were grit blasted with clean silica sand.

2.2. Mechanical testing

Specimens were tested using an Instron 8801MT servohydraulic materials testing system, rated to 100 kN peak dynamic load, with a control system capable of 10 kHz data acquisition and loop closure rate. Direct strain measurements were taken using an Instron dynamic extensometer with a 25 mm gauge length (a strain gauged, clip-on extensometer, calibrated at 2% of a 12.5 mm gauge length, manufacturer's part No. 2620-602), at the mid-point of the free length of each specimen. Specimens were clamped using hydraulically tensioned, wedge acting grips (rated for up to 100 kN axial load), with a regulated acting hydraulic pressure.

For the purposes of this study, tests were carried out in tension-tension mode, at a single loading level. After tuning the control system, each specimen was subjected to a cyclic load at 5 Hz, at a loading ratio of 0.1, to a peak stress equating to 50% failure strength. After an initial bedding-in period of 1000 cycles, to overcome the initial phase of rapid damage accumulation, the hydraulic pressure was varied up to 200 bar (supply pressure is nominally 207 bar), in increments of 20 bar, to apply a range of clamping stresses on the gripped section of the specimen.

For reference, the peak tensile load in these tests was 15 kN, which according to the guidance for gripping of metals (discussed earlier) would correspond to a gripping stress of just 14.3 MPa; no data point was taken for this value since the required hydraulic pressure is so low that it is not always sufficient to overcome mass and static friction on opening or closing the grips.

Key parameters of the dynamic behavior of the specimen (including phase angle, stiffness and modulus, for in-phase, out-of-phase, and complex behavior) were calculated live, for each cycle, by the test control software, using simulated sine wave correlation algorithms.

2.3. Infrared thermography

It is fairly well known that composites under cyclic loading are subject to significant self-heating effects [14, 19–21], through a combination of viscous heating and energy release through micro-fractures. Obviously this presents other experimental concerns which have been discussed elsewhere, but it facilitates identification of where strain and damage are being introduced [22].

An Optris PI450 bolometer thermal imaging camera was used to examine the edge of the specimen as it passed into the gripped section, and at the end of each test an image was captured and line scan data extracted along the centerline. Data are presented as a temperature increase profile; after subtraction of a baseline profile of the gripped specimen, prior to any loading.

For the purposes of this initial investigation, it was not deemed necessary to apply a constant emissivity coating, since all surfaces of interest were of the same material, meaning that the absolute surface temperatures calculated are of uncertain accuracy, but over the small temperature range present in these tests, the relative changes of interest are highly reliable. Surface temperature calculations were based on an emissivity of 0.96, typical for polymer matrix composites.

Specimen heating effects are directly linked to applied strain amplitude and to progressive damage accumulation, so the locations of more severely loaded regions of the specimen may be inferred from the temperature distribution. This approach is distinct from thermo-elastic stress analysis [23, 24] and the two must not be confused. TSA is a differential technique for evaluating the relative magnitude of the change in stress distribution between two loading states of a test piece subject to purely elastic load; in cyclic tests (on composites) it can only reliably be applied between two loading points within a single cycle over a relatively small stress range. The approach used for this paper is effectively measuring the cumulative energy dissipation in the material over a large number of cycles, from which a semi-quantitative measure of strain amplitude is inferred.

3. Results and discussion

3.1. Raw data

Raw data for strain measurements for each specimen is presented in Figure 1. Since this is a fatigue

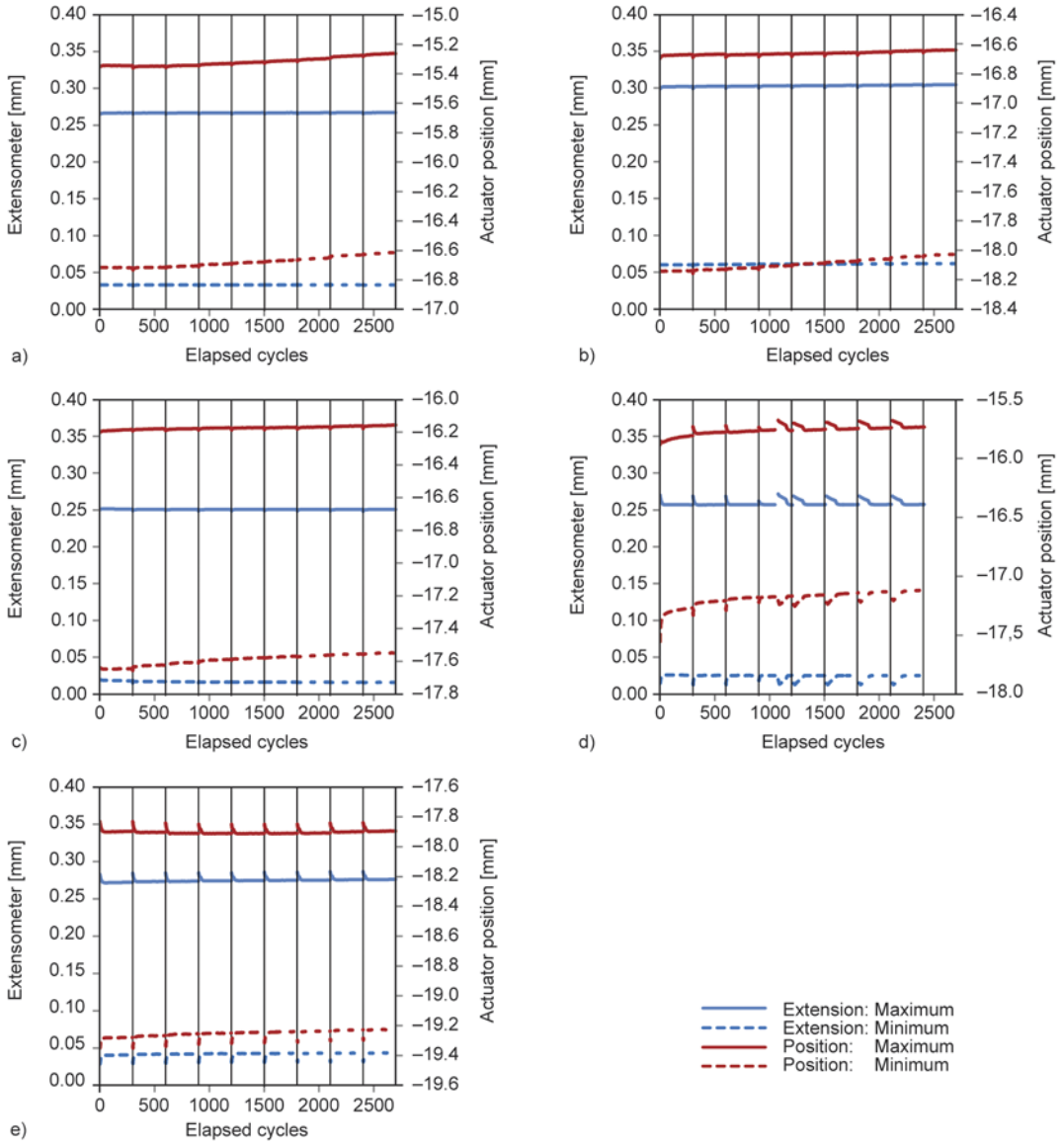

Figure 1. Peak strain from actuator displacement or extensometer reading vs elapsed cycles; vertical lines denote the timing of increments in gripping stress, a) GFRE tab, b) aluminium tab, c) no tab, d) abrasive cloth, e) SiC coated jaws

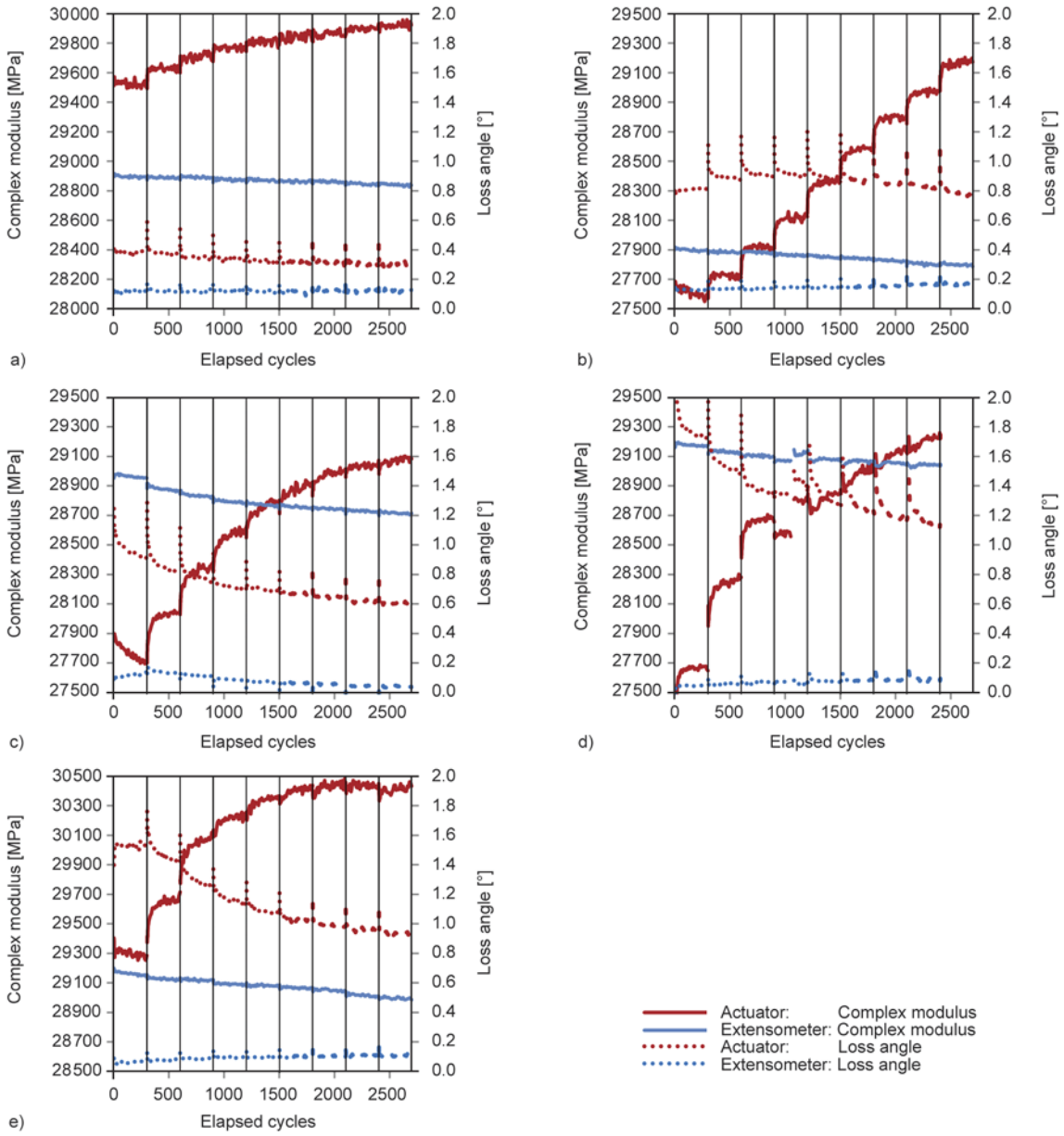

Figure 2. Calculated complex modulus from actuator displacement or extensometer reading vs elapsed cycles; vertical lines denote the timing of increments in gripping stress, a) GFRE tab, b) aluminium tab, c) no tab, d) abrasive cloth, e) SiC coated jaws

test, the specimen behavior does change with elapsed cycles, hence these charts are presented with cycles on the *x*-axis; vertical lines *are not* gridlines, but instead denote each point at which the hydraulic pressure to the grips was increased, by a step or 20 bar. The values of dynamic modulus and phase angle calculated live with each cycle are plotted in a similar manner in Figure 2.

3.2. Complex dynamic modulus

Under ideal conditions it is assumed that the specimen would be gripped such that there is no slipping of the specimen within the jaws, that load is introduced evenly without stress concentrations, and that the stiffness of the grip body and actuator are greatly above that of the specimen under test. Since our current standards for composite test coupons are straight and parallel sided, the result of this would be that any geometry-independent measurement of stiffness would ideally be identical when calculated from grip separation or extensometer respectively. Practically, this is clearly unrealistic, but many workers utilize grip separation to measure strain, for a variety of reasons. For this reason, the authors and many other sources frequently emphasize the importance of strain measurement on an appropriate gauge length.

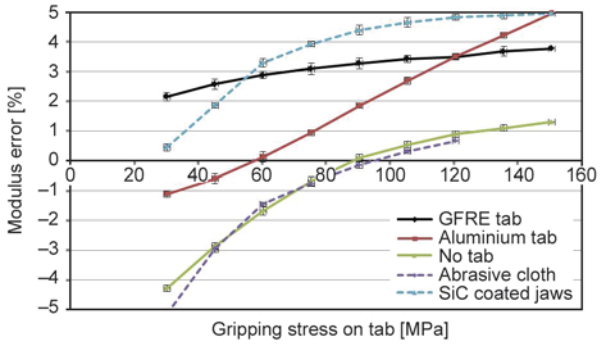

Figure 3. Error in measured complex modulus at grip vs gripping stress on tab (based on actuator displacement compared with extensometer measurement)

Figure 3 shows the error in complex modulus generated by imperfect gripping, and how it varies with the combination of clamping force and tab material. Each data point is the average of the percentage difference between 20 pairs of data points; 'error bars' on each data point indicate the maximum variation from mean.

The implication of a negative error is that there is significant shear or slippage within the gripped section; the effect of this is equivalent to a specimen with lower modulus or a larger gauge length. By contrast, positive errors suggest a degree of over-constraint on the specimen, causing the ends of the gauge length to exhibit greater on-axis stiffness. Logically it is also possible for a specimen to suffer from both effects at the same time; experiencing some slippage on the loading axis, while the ends of the gauge length are still subjected to a degree of over-constraint. For this reason, it is difficult to infer specific causality solely from the difference in extension or derived calculations, but it is the first step in identifying a problem.

On this basis it is postulated that the 'traditional' method of using cross-ply composite tabs results in noticeable over-constraint; potentially this is caused simply by the fact that the bonded tabs themselves apply considerable transverse constraint. Furthermore that this effect dominates compared with the small degree of slipping, which is known to happen at very low grip pressures through the evidence of abraded material which is found stuck in the serrations or the jaw face.

Conversely, the use of tab-less specimens (whether directly clamped in serrated, hardened steel jaws, or using the recommended layer of abrasive cloth) must give a significant degree of slipping or not clamp the full grip length. Using the same type of specimen with a silicon carbide bonded into the metal jaw surface still showed high sensitivity to clamping force, but surprisingly shifted the errors to a positive domain.

Finally, the use of aluminium tab material seems to be quite effective in achieving only a small error, without the need for high clamping forces which increase the risk of stress concentrations at the end of the gripped section.

3.3. Loss angle

Figure 4 shows the additional component of loss angle introduced at the grip, as compared with that at the extensometer measurement. Each data point is the average of the difference between 20 pairs of data points; 'error bars' on each data point indicate the maximum variation from mean. Loss angle (usually termed δ, or expressed as tan δ) can be used as a measure of the damping in a system. Since it is known that the specimen material is moderately consistent for its whole length, it must be assumed that a phase difference between the two displacement measurements is introduced by slipping or shear within the gripping assembly.

This appears to confirm the earlier suspicion that the composite tabs are held quite effectively, while the un-tabbed specimens experience more significant slippage.

It is interesting to note that the specimen with aluminium tabs introduced a similar degree of lag to the untabbed specimen, but probably for different reasons. With the untabbed specimen this seems very likely to be related to slippage, but the aluminium tabs appeared securely gripped throughout, so their contribution may come from shear within the metal. It was not possible to use digital image correlation during this study to determine the actual displacement

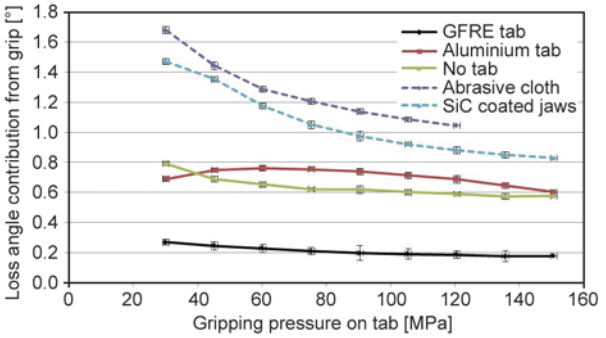

Figure 4. Additional phase lag introduced in grip vs gripping pressure (phase angle at extensometer for all tests was within 0.10±0.05°)

fields, but the authors intend to pursue this in further work to resolve these questions.

3.4. Temperature distribution

Figure 5 shows thermal images of the 5 different tab/grip configurations. A localized heating effect near the end of the grip is particularly obvious on the specimen with conventional composite tabs.

It is very clear that in the standard tabbed specimens, there is a very high degree of heating just within the end of the gripped section. The specimen gripped with un-bonded abrasive cloth behaved similarly. Using integral abrasive surfaces on the jaws, without tabs, seemed to reduce the sharp peak in heating, but caused more heat introduction further back into the grip, possibly due to sliding and abrasion. By contrast, specimens without tabs, or with aluminium tabs, show very gentle transitions from gripped to free length.

The specimens without any tabs and with aluminium tabs have remained much cooler that the others, probably due to much better conduction extracting more rapidly the heat which is generated. Since fatigue performance of composites is necessarily affected by temperature, due to the nature of the matrix materials, this would suggests that fatigue test specimens are doubly likely to fail at the grip, since the material near the end of the tab is both more highly stressed and at higher temperature.

Figure 6 plots the increase in surface temperature along the center-line of these specimens after cyclic loading

It is very clear that in the standard, composite-tabbed specimen, there is a very high degree of heating just within the end of the gripped section. Despite earlier

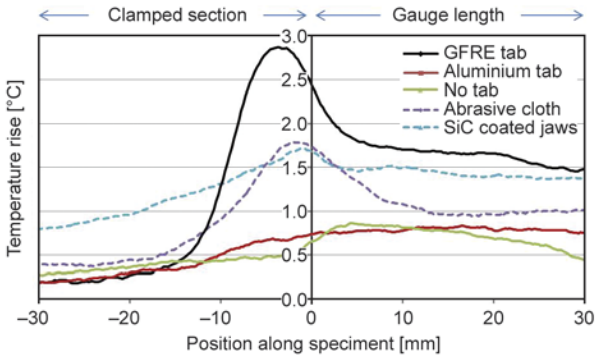

Figure 6. Temperature profiles along specimen edge as it enters the grip

indications (see section 3.4) that the tab-less specimen gripped with un-bonded abrasive cloth suffers significant slippage, the thermal activity in this configuration is very similar to the standard tabbed specimen. The implication of this is that the load introduction and damage localization is very similar between these two configurations. It may be argued that this is not an unexpected outcome, since these methods were established as moderately reliable and comparable early on in quasi-static test development for composites [1]; this would imply that the induced mechanical behavior of the specimen must be congruent in order to achieve similar results.

By contrast, specimens without tabs, or with aluminium tabs, show very gentle transitions from gripped to free length. It must be recognized that these specimens have a more direct connection to the metal jaws, through which heat might be conducted away into the thermal mass of the grips. Although this would surely suppress the magnitude of temperature rise, any significant local heating effects should still be apparent. It would appear that the severity of local

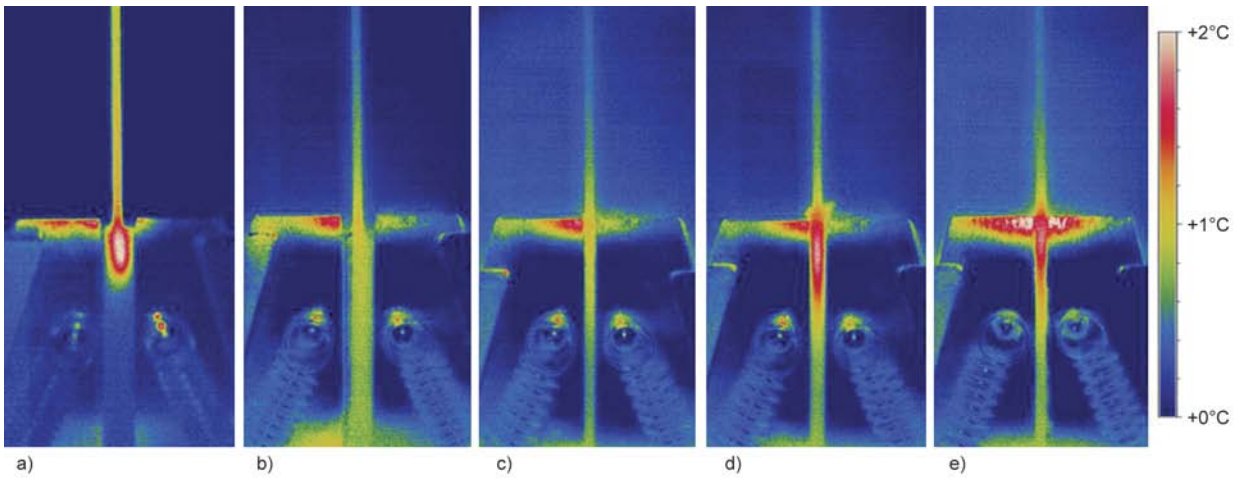

Figure 5. Thermal images of the specimen edge after cyclic loading. (a) GFRE tab; (b) Aluminium tab; (c) Tab-less; (d) Tab-less with abrasive cloth; (e) Tab-less in SiC fused jaws.

heating and grip-induced damage is reduced in these solutions, which do not conform to current international standards.

Using jaw faces with a rough silicon carbide surface, fused directly to the steel, with a tab-less specimen, seemed to reduce the sharp peak in heating, but caused more heat introduction further back within the grip. This may be due to sliding and abrasion of the surface, as previously discussed, which might reasonably overwhelm the better conductive path to extract heat into the jaws.

The authors have been unable to identify any other experimental analysis of stress or strain concentrations in the gripping region of composite test coupons for in-plane tensile or compressive property measurement. However, a survey of stress concentrations within the gripped section was conducted by De Baere *et al.* [8], using finite element modelling, for a fairly extensive range of tab and grip permutations. For GRFE tabbed specimens, the temperature rise illustrated by the line scans presented in Figure 6 seem to correspond well with the calculated stress concentrations along the specimen presented in that study. For aluminium tabbed specimens the computational method anticipated a small peak in stress concentration near the end of the tabs, which is not observed in the experimental data here, although this effect may be masked by the much better heat conduction along and out of the specimen, as already mentioned. De Baere *et al*. [8] did not examine untabbed specimens.

During the tests, it was also noted that the temperature distribution appears to change with the applied clamping stress. As shown in Figure 7, qualitatively speaking, higher clamping stress seems to push the localized heating into a tighter region, closer to the end of the gripped section, or just beyond it on some tab-less specimens. At the time of writing, insufficient data was available to draw any reliable conclusions without further testing.

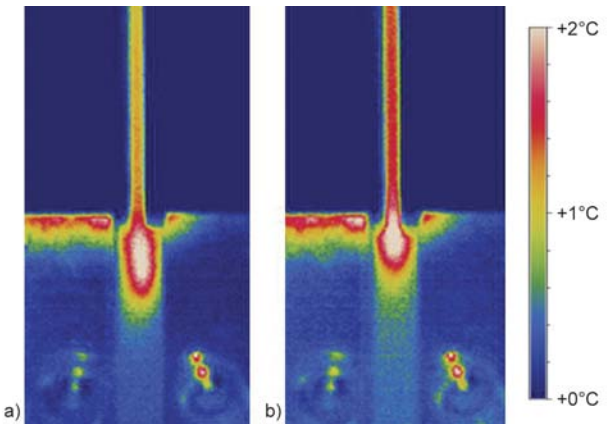

Figure 7. Temperature distribution on GFRE tab specimen (a) after 1600 cycles with 30 MPa clamping stress and (b) after a further 2100 cycles at 120 MPa clamping stress

4. Conclusions

The implication of these data is that, at least in cyclic testing of composites, the standard method of gripping composite coupons can easily cause damage and failure outside the gauge length, under un-representative loading conditions. This initial study gives some clues for how to locate and reduce the problem, and the findings are in agreement with computational models of stress concentration, as well as anecdotal evidence from a significant number of workers who regularly observe failure within the gripped section of composite fatigue test coupons.

The short case study presented here is based on a small sample size, but the indications are that there is a need to reconsider the best methods for gripping composite specimens for fatigue loading. The authors intend to verify this on a larger sample, and using several other representative materials.

References

[1] Hart-Smith L. J.: Generation of higher composite material allowables using improved test coupons. in 'Proceedings of the 36th International SAMPE Symposium, San Diego, USA' 1029–1045 (1991).

[2] Hojo M., Sawada Y., Miyairi H.: Influence of clamping method on tensile properties of unidirectional CFRP in 0° and 90° directions – Round Robin activity for international standardization in Japan. Composites, **25**, 786–796 (1994).
DOI: 10.1016/0010-4361(94)90139-2

[3] ASTM D3039/D3039M-14: Standard test method for tensile properties of polymer matrix composite materials (2014).

[4] Becerra N.: Flight mission. Testing, testing. Materials World, **22**, 26–27 (2014).

[5] Bailey P. B. S.: Growth in dynamic testing market for composites. Advanced Materials and Processes, **172**, 17–21 (2014).

[6] BS EN ISO 527-5: Plastics. Determination of tensile properties. Test conditions for unidirectional fibre-reinforced plastic composites (2009).

[7] Morrell, R., McCartney L. N.: Measurement of properties of brittle-matrix composites. British Ceramic Transactions, **92**, 1–7 (1993).

[8] De Baere I., Van Paepegema W., Degrieck J.: On the design of end tabs for quasi-static and fatigue testing of fibre-reinforced composites. Polymer Composites, **30**, 381–390 (2008).

[9] Kawai M., Morishita M., Satoh H., Tomura S.: Effects of end-tab shape on strain field of unidirectional carbon/epoxy composite specimens subjected to off-axis tension. Composites Part A: Applied Science and Manufacturing, **28**, 267–275 (1997).
DOI: 10.1016/S1359-835X(96)00122-4

[10] Sun C. T., Chung I.: An oblique end-tab design for testing off-axis composite specimens. Composites, **24**, 619–623 (1993).
DOI: 10.1016/0010-4361(93)90124-Q

[11] Curtis P.: CRAG test methods for the measurement of the engineering properties of fibre reinforced plastics. Technical Report 88012. Royal Aerospace Establishment, Farnborough (1988).

[12] De Baere I., Van Paepegem W., Quaresimin M., Degrieck J.: On the tension–tension fatigue behaviour of a carbon reinforced thermoplastic Part I: Limitations of the ASTM D3039/D3479 standard. Polymer Testing, **25**, 625–632 (2011).
DOI: 10.1016/j.polymertesting.2011.05.004

[13] De Baere I., Van Paepegem W., Hochard C., Degrieck J.: On the tension–tension fatigue behaviour of a carbon reinforced thermoplastic Part II: Evaluation of a dumbbell-shaped specimen. Polymer Testing, **30**, 663–672 (2011).
DOI: 10.1016/j.polymertesting.2011.05.005

[14] Curtis D. C., Moore D. R., Slater B., Zahlan N.: Fatigue testing of multi-angle laminates of CF/PEEK. Composites, **19**, 446–452 (1988).
DOI: 10.1016/0010-4361(88)90702-1

[15] Xiao J., Bathias C.: Fatigue behaviour of unnotched and notched woven glass/epoxy laminates. Composites Science and Technology, **50**, 141–148 (1994).
DOI: 10.1016/0266-3538(94)90135-X

[16] Patrick M., Norman T. L.: Effect of notch on failure of two-dimensional ±45° triaxial braided textile composite materials. ASTM Journal of Composites Technology and Research, **16**, 262–269 (1994).

[17] ASTM D7615/D7615M-11: Standard practice for open-hole fatigue response of polymer matrix composite laminates (2011).

[18] Spearing S. M., Beaumont P. R. W.: Fatigue damage mechanics of composite materials. I: Experimental measurement of damage and post-fatigue properties. Composites Science and Technology, **44**, 159–168 (1992).
DOI: 10.1016/0266-3538(92)90109-G

[19] Liu C., Cheng L., Luan X., Li B., Zhou J.: Damage evolution and real-time non-destructive evaluation of 2D carbon-fiber/SiC-matrix composites under fatigue loading. Materials Letters, **62**, 3922–3944 (2008).
DOI: 10.1016/j.matlet.2008.04.063

[20] Ogasawara T., Onta K., Ogihara S., Yokozeki T., Hara E.: Torsion fatigue behavior of unidirectional carbon/epoxy and glass/epoxy composites. Composite Structures, **90**, 482–489 (2009).
DOI: 10.1016/j.compstruct.2009.04.023

[21] Bailey P. B. S., Hoehl C., Jamshidi P., Cowan C., Squires S., Smith A. J.: Enhanced fatigue testing of composites. in 'Proceedings of the 19th International Conference on Composite Materials, Montreal, Canada' 5033–5038 (2013).

[22] Toubal L., Karama M., Lorrain B.: Damage evolution and infrared thermography in woven composite laminates under fatigue loading. International Journal of Fatigue, **28**, 1867–1872 (2006).
DOI: 10.1016/j.ijfatigue.2006.01.013

[23] Baker L. R., Webber J. M. B.: Thermoelastic stress analysis. Optica Acta: International Journal of Optics, **29**, 555–563 (1982).
DOI: 10.1080/713820858

[24] Fruehmann R. K., Dulieu-Barton J. M., Quinn S.: Assessment of fatigue damage evolution in woven composite materials using infra-red techniques. Composites Science and Technology, **70**, 937–946 (2010).
DOI: 10.1016/j.compscitech.2010.02.009